Phase Calibration of Multi-Baseline Pol-InSAR Data Stacks

Matteo Pardini
Vittorio Bianco
Konstantinos Papathanassiou

DLR

Institut für
Hochfrequenztechnik
und Radarsysteme

INTERNER BERICHT

DLR-HR-IB-551-1/2014

DLR

Phase Calibration Of Multi-Baseline Pol-InSAR Data Stacks

Bearbeiter:	Dr. Matteo Pardini	5.02.2014 Datum
Betreuer:	Dr. Konstantinos Papathanassiou	05.02.14. Datum
Abteilungsleiter:	Dr. Gerhard Krieger	06.02.14 Datum
Institutsdirektor:	Prof. Dr. Alberto Moreira	06.02.14 Datum

Der Bericht enthält: 98 Seiten, Bilder, Tabellen, Literaturzitate

Signatur Bibliothek FZ-OP	Barcode Bibliothek FZ-OP

Institut für Hochfrequenztechnik und Radarsysteme

INTERNER BERICHT

DLR-HR-IB-551-1/2014
Version: 1.0
Datum: 05.02.2014

Dokument Nummer: DLR-IB-551-1/2014

Titel: Phase Calibration of Multi-Baseline Pol-InSAR Data Stacks

Verfasser: Matteo Pardini

Projekt:

Fachgruppe: Information Retrieval

Abteilungsleiter: Dr. Gerhard Krieger

Kurzbeschreibung: New opportunities are arising in Earth observation with the use of multibaseline (MB) SAR being able to combine data stacks for an improved imaging and characterization of the observed scene. Prior to any MB coherent processing, it is necessary to correct the data stack for the phase contributions due to residual non-compensated platform motions (typical in airborne SAR applications) and/or atmospheric propagation delays (e.g. in spaceborne SAR), which in general are different from track to track. The classical calibration methods tackle the MB phase calibration problem by means of the detection of point-like scatterers. However, the effectiveness of these techniques is scenario-dependent, as both the number and spatial distribution of such scatterers varies. Especially in natural scenarios, the MB phase calibration is particularly challenging given the volumetric nature of the scattering. Moreover, a limited number of baselines can impair the detection performance, which in turn results into a degraded calibration quality. In this work we propose a new calibration method based on the minimization of the entropy applied on the vertical profile of the backscattered power to improve the performance. This allows to potentially exploit the MB SAR signal independently of the imaged scattering mechanism. With particular reference to SAR Tomography applications, the proposed method has been tested under controlled conditions by processing a simulated dataset of a forest stand. Performance results are shown in this presentation. The calibration accuracy has been also evaluated with an airborne L-Band dataset acquired by the DLR E-SAR platform over the forest site of Traunstein (Germany), and comparisons with the classical calibration techniques have been carried out.

Schlüsselworte: SAR, tomography, entropy minimization, phase calibration, baseline errors, atmospheric propagation

---

Deutsches Zentrum für Luft- und Raumfahrt e.V.
Institut für Hochfrequenztechnik und Radarsysteme
Institutsdirektor Prof. Dr. Alberto Moreira
Oberpfaffenhofen - 82234 Weßling

Verteiler:

1 Stück Bibliothek Forschungszentrum Oberpfaffenhofen
1 Stück Institutsleiter Prof. Dr. Alberto Moreira
1 Stück Prof. Dr. Helmut Süß
1 Stück Dr. Gerhard Krieger
1 Stück Dr. Manfred Zink
1 Stück Dr. Andreas Reigber
5 Stück Information Retrieval and PolInSAR Gruppen

Deutsches Zentrum für Luft- und Raumfahrt e.V.
Institut für Hochfrequenztechnik und Radarsysteme
Institutsdirektor Prof. Dr. Alberto Moreira
Oberpfaffenhofen - 82234 Weßling

Deutsches Zentrum
für Luft- und Raumfahrt e.V.
in der Helmholtz-Gemeinschaft

PHASE CALIBRATION OF MULTI-BASELINE POL-INSAR DATA STACKS

Technical Report

M. Pardini[1], V. Bianco[2], K. Papathanassiou[1]

[1] Deutsches Zentrum für Luft- und Raumfahrt (DLR)
Microwave and Radar Institute (HR) – Weßling (Germany)

[2] University of Naples "Federico II" – Naples (Italy)

November 2013

The experiments presented in this report were carried out during the stay of V. Bianco in DLR-HR for his M.Eng. thesis work, supervised by M. Pardini (DLR-HR), K. Papathanassiou (DLR-HR) and A. Iodice (Univ. of Naples) between June and December 2011.

- This page intentionally left blank -

ABSTRACT

New opportunities are arising in Earth observation with the use of multibaseline (MB) SAR being able to combine data stacks for an improved imaging and characterization of the observed scene. Prior to any MB coherent processing, it is necessary to correct the data stack for the phase contributions due to residual non-compensated platform motions (typical in airborne SAR applications) and/or atmospheric propagation delays (e.g. in spaceborne SAR), which in general are different from track to track. The classical calibration methods tackle the MB phase calibration problem by means of the detection of point-like scatterers. However, the effectiveness of these techniques is scenario-dependent, as both the number and spatial distribution of such scatterers varies. Especially in natural scenarios, the MB phase calibration is particularly challenging given the volumetric nature of the scattering. Moreover, a limited number of baselines can impair the detection performance, which in turn results into a degraded calibration quality. In this work we propose a new calibration method based on the minimization of the entropy applied on the vertical profile of the backscattered power to improve the performance. This allows to potentially exploit the MB SAR signal independently of the imaged scattering mechanism. With particular reference to SAR Tomography applications, the proposed method has been tested under controlled conditions by processing a simulated dataset of a forest stand. Performance results are shown in this presentation. The calibration accuracy has been also evaluated with an airborne L-Band dataset acquired by the DLR E-SAR platform over the forest site of Traunstein (Germany), and comparisons with the classical calibration techniques have been carried out.

- This page intentionally left blank -

TABLE OF CONTENTS

CHAPTER 1

INTRODUCTION

1.1 Synthetic aperture radar imaging

The term "remote sensing" refers to the process of detection, acquisition, recording and analysis of physical properties of an area by measuring its reflected or emitted radiation, with devices not in physical contact with the surface being analysed [1]. Generally speaking, sensors are classified as passive and active. In the field of microwaves, a passive sensor, named radiometer, measures the electromagnetic radiation reflected or emitted by the investigated surfaces, operating as an incoherent receiver. Conversely, an active sensor is able to transmit a signal and to (coherently) receive the back-scattered echo, which will be affected by the physical features of the object under study [1]. In particular, a Real Aperture Radar (RAR) is an active device which generates short duration phase modulated pulses (chirps) in the microwave region of the electromagnetic spectrum, being able to return images either during the day and the night in a weather-independent way (the Earth's atmosphere is almost transparent in this region), thus overcoming the main limitation of passive sensors. For a RAR the achievable along-track resolution shows a range distance dependent behavior, which unavoidably constrains these systems to poor resolution[1] values, so limiting their employment [2].

Born to face this problem, the Synthetic Aperture Radar (SAR) notion was firstly introduced by Carl Wiley in 1965 [2]. He stated that it is possible to simulate an antenna array behavior moving the transmitter and collecting the received pulses from several positions along the platform flight track. The coherent integration of the compressed pulses produces an output equivalent to a very large narrow beam antenna, referred to as *synthetic*, thus enabling to achieve an azimuth resolution independent from the surface-sensor distance; on the other hand, the range resolution capability is guaranteed by the short duration of the transmitted pulse.

Nowadays, SAR is deeply employed for land use and soil moisture mapping, urban areas growth monitoring, weather changes detecting by means of glaciers dissolution observation, forest classification,

[1] The radar resolution is defined as the minimum distance at which two point-like scatterers have to be placed in order

biomass measurements and anomalous events reporting. Moreover, the range-azimuth high resolution, weather independence, day and night working capabilities make SAR systems suited for the continuous and global monitoring of the Earth surface [2]-[5].

The SAR imaging process provides a geometric projection of the 3-D radar reflectivity function $\beta(x,y,z)$ into a 2-D cylindrical coordinates (x,r) (where x denotes the azimuth direction, i.e. the one parallel to the flight track, r is the slant-range, and z is the vertical height), followed by a 2-D convolution with the system azimuth-range point-spread function (PSF) $g(x,r)$ [2], [5]:

$$y(x,r)=\left[\int \beta(x,y,z)Rd\theta \exp\left(-\frac{4\pi}{\lambda}r\right)\right]\otimes\otimes g(x,r) \tag{1.1}$$

where $y(x,r)$ is the complex SAR image, R is the distance between the sensor and the target, θ is the look angle, and λ is the wavelength.

1.2 SAR Interferometry

The product of a SAR acquisition is the complex image $y(x,r)$ which collects the complex reflectivity information filtered by the system PSF. SAR Interferometry (InSAR) is a well-established technique to achieve the elevation information and to produce topography surface models [2]-[5]. The first applications of interferometry to radar dates back to 1974 by L.C. Graham [3], followed by experiments made by R.M. Goldstein and H.A. Zebker during the '80s, till in the 1991 the European Space Agency (ESA) launched the ERS-1 sensor which provided continuous and nearly global Earth surface mapping. After several attempts, on February 2000 the Shuttle Radar Topography Mission (SRTM) set the basis for the deep development of research and commercial applications based on InSAR products by generating a global Earth surface digital elevation model (DEM) with about 90m cell spacing.

The main concept behind InSAR is to introduce some kind of diversity in the acquisition system in order to get knowledge about the missing third dimension [2]. When viewing angle diversity is exploited InSAR is normally called *across-track interferometry* (XTI-SAR). A cross-track InSAR system acquires two complex SAR images from two antennas slightly separated by a cross-track baseline $B_\perp$. The phase difference φ between the echoes collected by the two antennas, called *interferometric phase*, can be used to determine the terrain height for each pixel according to the following relationship [2], [4]:

$$z = H - r\cos\left[\xi - \cos^{-1}\left(-\frac{\varphi\lambda}{4\pi B_\perp}\right)\right] \tag{1.2}$$

where H is the platform altitude, and ξ is the baseline tilt angle (the angle between the baseline and the ground range axis). The basic InSAR processing can be summarized as follows [2],[4]:

1. Firstly, two focused SAR images has to be acquired and focused preserving the phase information and the images have to be co-registered in order to compensate the range difference existing between the two acquisitions;

---

to be discriminated by the system.

2. A calibration procedure has to be set up to compensate the platform deviations from the nominal track;
3. Since the sensor receives from each resolution cell a back-scattered wave which is the result of the coherent superposition of many microscopic contributions, SAR images are affected by the so-called *speckle*[2] noise. Furthermore, an additive thermal noise contribution on the received signal is always present. Hence, a multi-looking[3] step is needed to counteract the consequent degradation effects. Basically, it consists in taking several looks of a target in a single radar sweep (a simple way to get this can be to separate the synthetic antenna in sub-apertures) and in averaging the obtained images;
4. Denoting with N the number of looks, for each fixed pixel (x,r) the corresponding interferometric phase can be estimated as follows:

$$\hat{\varphi}(x,r) = \arg\left\{\sum_{n=1}^{N} y_{1,n}(x,r)\, y_{2,n}^{*}(x,r)\right\} \tag{1.3}$$

5. The achieved phase has to be unwrapped to remove the 2π ambiguities.
6. Finally the height information can be retrieved by means of (1.2).

In the last two decades, XTI-SAR has found many applications in topographic and urban mapping, geophysics, forestry, as well as hydrology and glaciology [4].

When the diversity parameter is the acquisition time, the technique is referred to as *along-track interferometry* (ATI-SAR). It can be used to detect additional non-topographic information such as velocity measurements on both short and large time scales [2]. In the first case, the interferogram is built with two temporally close acquisitions along the same track, so their phase difference is mainly due to scatterer motion in range direction. By measuring the Doppler shift, the velocity of the target can be easily obtained, making ATI-SAR a useful instrument for ocean currents and waves monitoring. On the other hand, very small variations can be registered by increasing the temporal distance between the acquisitions. In this case, if the same nominal track could be assumed for both of the acquisitions, the phase difference would be only related to the scene changes. Unluckily, platform motion is always affected by oscillations with respect to the nominal track, hence the interferometric phase has a topographic contribution which has to be taken into account. To overcome this limitation Differential SAR interferometry (D-InSAR) has been developed in the last two decades. The idea is to utilize three images (or two images with addition of a DEM) to subtract the topographic content from the interferogram, thus revealing differential fringes indicating surface displacements on a scale smaller than the radar wavelength, usually in the millimetre range. This enables a monitoring of ecological stress-changes processes [6]-[7] like sudden co-seismic displacements, long-term tectonic movements, volcanic bulging before eruptions, land sliding in mountainous areas and glaciers movements.

[2] The *speckle* is a multiplicative noise characterizing each SAR image, which is due to the interferences between the backscattered echoes coming from different elementary scatterers in the same resolution cell. Due to the typical effect of random walk in the complex plane, the coherent combination of these contributions leads to amplitude fluctuations of the resulting received signal, even for close-by pixel belonging to the same homogeneous area.

[3] Individual *looks* are groups of signal samples in a SAR processor that splits the full synthetic aperture into several sub-apertures, each representing an independent look of the same scene. The resulting multi-look image formed by

Moreover, by using multi-frequency or multi-polarised repeat-pass data sets, other kinds of diversity can be exploited to detect changing processes in natural surfaces or vegetation layers. In the last framework, Polarimetric SAR Interferometry (PolInSAR) is a powerful mean which combines the capability of interferometry to extract height information with polarimetric decomposition techniques, in order to achieve a limited volumetric imaging and to allow an estimation of canopy heights or underlying ground topography [8]-[11].

1.3 The layover phenomenon and multidimensional imaging

As already mentioned, the SAR imaging process results into a mapping on the (x,r) plane of the scene reflectivity function. As a consequence, when a high slope topography is present, or when the radar wave penetrates into a volume, the sensor receives in the same instant backscattered echoes from a number of surface locations characterized by different heights, which will be mapped in the same range-azimuth resolution cell [2]. The corresponding pixel will be then associated to an "integrated" intensity value. This well-known phenomenon, named *layover,* strongly gives rise to interpretation ambiguities and affects acquisitions on urban areas as well as forested or glacier ones, where a typical residual volumetric scattering contribution at low frequencies is present. InSAR processing provides height information, but it has no resolving capability along the third dimension since it is unable to separate multiple scattering mechanisms in the same cell [2], [5].

To solve this problem, several approaches have been proposed in literature. Multifrequency methods try to exploit the frequency-dependent behavior of the penetration coefficient in order to get returns from different layers. For instance, in forested areas it would be possible, to resolve the canopy and the ground contribution. Anyway, it has been widely demonstrated that there is no frequency sensitive only to the ground under a vegetation layer without being affected by any volume scattering contribution [11]. In this scenario, a different solution requires the use of fully-polarimetric imaging, which takes advantage of polarization diversity to separate the scattering sources (typically, volume backscattering is the strongest one in the HV channel). As it will be discussed in the next Section, PolInSAR, exploits information retrieved from different polarimetric channels and combines them using across track interferometric techniques [8]-[10]. In this framework, the successful results in tree height and underlying ground topography estimation also highlight the key role played by the cross-polarized (HV) channel measurement, making fully polarimetric data sets necessary for this purpose.

However, contributions distributed over different heights cannot be resolved if they belong to the same scattering mechanism. In order to enhance the height resolution capability and to generate 3-D images of complex scenarios, SAR 3-D tomography (Tomo-SAR) techniques have been developed in the last decade starting from the first airborne tomographic experiment at the German Aerospace Center (DLR) of [12]. The main idea is to perform an additional aperture synthesis along the vertical plane (i.e., a beam forming in the elevation direction) exploiting multi-baseline (MB) data sets. As it will be discussed more in detail in the

---

incoherent combination of these looks is characterized by reduced speckle at the cost of degraded spatial resolution.

following, a Fourier transform relation exists between data collected with multiple tracks and the reflectivity function $\gamma(x,r,z)$. Thus, the coherent combination of MB data allows to produce vertical profiles representing the distribution of the power backscattered by targets distributed along the third dimension. Thanks to its innovative features, Tomo-SAR constitutes a promising mean for biomass estimation, forest and urban settlement classification, tree and building height retrieval, ice thickness monitoring and other risk control problems (see [13] and references therein). Other enhancements to MB 3-D imaging methods have been recently introduced. In the Polarimetric Tomo-SAR, the polarimetric information is employed in order to improve the estimation accuracy of the vertical position of the imaged scatterers and the physical interpretation of the vertical profiles. In [14] several algorithms, already deeply exploited in the Tomo-SAR framework, have been generalized in order to determine height-dependent optimal polarization combinations.

Recently, a new multidimensional imaging mode has been proposed to adapt 3-D imaging to scenarios in which scattering can vary in time, such as urban areas (due to e.g. terrain displacements) and forest areas, in which scattering changes produce temporal decorrelation. This mode, generally referred as Differential SAR Tomography [15] or 4-D imaging, is based on the synergic combination of Tomo-SAR and D-InSAR in order to jointly get scatterer separation in height and scatterer temporal characterization. For instance, in scenarios affected by subsidence, they return a power distribution in the height-deformation velocity plane, thus enabling a differential InSAR at each height. In this way, layover ambiguities in extremely variable urban environments can be solved or temporal decorrelating volumetric scatterers (for example moving glaciers) can be monitored [13], [15]. A Polarimetric Differential Tomo-SAR imaging has been proposed and firstly tested in [16]. In this way, the polarimetric characterization and interpretation is possible of temporal-varying scattering phenomena at different heights.

1.4 PolInSAR: scatterer separation with different polarizations

PolInSAR methods can separate scattering contribution in the same resolution cell by joining polarimetric techniques to InSAR and by relating the polarimetric-interferometric coherences to scattering models. Especially in forest scenarios, PolInSAR is nowadays a well-assessed and mature technique able to estimate forest height with a precision in the order of magnitude of 1m.

In [8] the polarization-dependent behaviour of scattering was demonstrated and exploited for an improved interferometry. For a better understanding, a generalization is possible of the classical scalar interferometry by starting from the following 3-dimensional Pauli scattering vector in a single pixel in the case that a quad-pol system is available[4]:

$$\mathbf{k} = \frac{1}{\sqrt{2}}\left[y_{HH} + y_{VV}, y_{HH} - y_{VV}, 2y_{HV}\right]^T \tag{1.4}$$

where subscript T denotes the transpose operator. The resulting 6×6 interferometric multi-polarimetric covariance matrix is [8]:

[4] The dependency on pixel coordinates (x,r) has been dropped for the sake of notation simplicity.

$$\mathbf{T}_6 = E\left\{\begin{bmatrix}\mathbf{k}_1\\ \mathbf{k}_2\end{bmatrix}\begin{bmatrix}\mathbf{k}_1^H & \mathbf{k}_2^H\end{bmatrix}\right\} = \begin{bmatrix}\mathbf{T}_{11} & \boldsymbol{\Omega}_{12}\\ \boldsymbol{\Omega}_{12}^H & \mathbf{T}_{22}\end{bmatrix} \tag{1.5}$$

where the subscript H denotes the Hermitian transpose, $E\{\cdot\}$ indicates the operator performing the statistical expectation, and:

$$\begin{aligned}\mathbf{T}_{11} &= E\left\{\mathbf{k}_1\mathbf{k}_1^H\right\}\\ \mathbf{T}_{22} &= E\left\{\mathbf{k}_2\mathbf{k}_2^H\right\}\\ \boldsymbol{\Omega}_{12} &= E\left\{\mathbf{k}_1\mathbf{k}_2^H\right\}\end{aligned} \tag{1.6}$$

The objective is to generalize the concept of interferogram to embed all the possible combinations of polarization states. It is then useful to introduce a couple of normalized complex column vectors $(\boldsymbol{\omega}_1, \boldsymbol{\omega}_2)$ representing two generic scattering mechanisms. The projections of $(\mathbf{k}_1, \mathbf{k}_2)$ are:

$$[\mu_1, \mu_2] = \left[\boldsymbol{\omega}_1^H\mathbf{k}_1, \boldsymbol{\omega}_2^H\mathbf{k}_2\right]. \tag{1.7}$$

In this way, for different choices of $(\boldsymbol{\omega}_1, \boldsymbol{\omega}_2)$, it possible to generate any kind of interferogram with corresponding interferometric phase given by

$$\varphi_{12} = \arg\left(\boldsymbol{\omega}_1^H\boldsymbol{\Omega}_{12}\boldsymbol{\omega}_2\right). \tag{1.8}$$

Thus, assuming that at least two orthogonal scattering mechanisms *i* and *j* can be separated by means of a proper choice of the combination vectors[5], an additional information can be obtained by computing the phase difference between the corresponding interferograms:

$$\Delta\varphi_{ij} = \arg\left(\mu_{1i}\mu_{2i}^*\right) - \arg\left(\mu_{1j}\mu_{2j}^*\right), \tag{1.9}$$

which represents the phase difference between the effective phase centers of the related scattering mechanisms [8]. For instance, if in the forest under analysis two orthogonal scattering mechanisms could be received from the ground and the vegetation layer, the difference between the corresponding height centroids could be simply obtained from (1.9), thus allowing to estimate the elevation of the top of the canopy. Unfortunately, experimental analyses showed the presence of both volume and scattering contributions in all polarizations, so that orthogonal scattering mechanisms, even though present, are not the only ones received from the polarimetric sensors. Recent advances have shown different ways to obtain more significant scattering mechanisms in terms of separation between ground and volume scattering [11].

To estimate the parameters of different scatterers in the same cell, more complex model-based inversion algorithms have then been developed [9]-[10]. For the particular case of SAR acquisitions over forest stands, a simple but reliable model is the Random Volume Over Ground (RVOG), which relates the observed multipolarimetric-interferometric coherences with the forest parameters. Basically, the investigated area is divided in two layers in the height dimension, as shown in Fig. 1.1. A ground scatterer is located at height $z = z_0$ with scattering amplitude per volume unit m_G, whereas the vegetation layer is seen as a

[5] It is possible to demonstrate that two orthogonal scattering mechanisms can be obtained through the

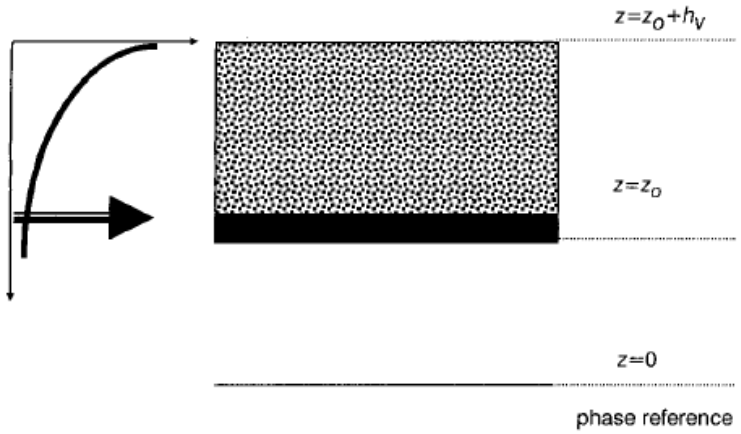

Figure 1.1 – Schematic representation of the RVOG model (reproduced from [9]).

volume of thickness h_V, filled with randomly oriented particles, and scattering amplitude m_V. According to the model, it is possible to express the complex interferometric coherence $\gamma(\boldsymbol{\omega})$ associated to a generic scattering mechanism $\boldsymbol{\omega}$ as follows [7]:

$$\gamma(\boldsymbol{\omega}) = \exp(j\phi_0)\frac{\gamma_V + m(\boldsymbol{\omega})}{1 + m(\boldsymbol{\omega})}, \tag{1.10}$$

where ϕ_0 denotes the ground phase (which is a linear function of the ground height through the baseline-dependent height-to-phase conversion factor k_z) and

$$m(\boldsymbol{\omega}) = \frac{m_G(\boldsymbol{\omega})}{m_V(\boldsymbol{\omega})}\exp\left(-\frac{2\varepsilon h_V}{\cos\theta_0}\right) \tag{1.11}$$

is the effective ground-to-volume amplitude ratio. In (1.10) and (1.11) γ_V and ε indicate the complex coherence accounting for the volumetric contribution alone and the extinction coefficient through the volume, respectively, h_V is the forest height, and θ_0 is the incidence angle. In [10] a three-stage inversion method has been tested by employing a simulated coherent electromagnetic scattering model and its effectiveness in parameter estimation, especially forest height, has been validated when at least one polarimetric channel can be found where the ratio $m(\boldsymbol{\omega})$ is small. Since then, forest height estimation matured and developed from a pre-operational to an operational PolInSAR product that has been validated in the frame of several campaigns over a wide range of forest, terrain and environmental conditions. The limitations of the individual inversion approaches and the error propagation through them are today well understood as well as the options available to compensate for them.

As a final note, MB PolInSAR inversion approaches have been investigated recently. In [17], it has been shown that MB approaches are useful to reduce constraints for single baseline PolInSAR inversion such as non-volumetric decorrelation effects and the height sensitivity of the vertical wavenumber. Moreover, MB PolInSAR inversion could contribute to compensate or filter out inversion results with strong height errors, improving significantly the accuracy of the estimation of the forest height.

---

eigendecomposition of the polarimetric-interferometric coherence matrix [8].

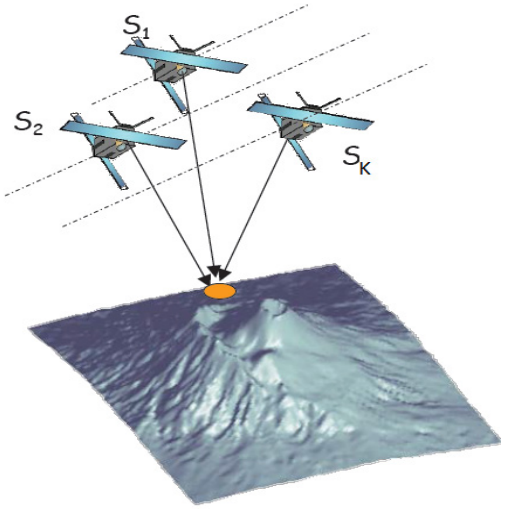

Figure 1.2 – MB acquisition with *K* sensors (reproduced from [18]).

1.5 Tomo-SAR: scatterer separation with multiple baselines

As already discussed, InSAR mainly assumes that just one single target is present within the resolution cell, and estimates the height of its scattering centroid and outputs a map which establishes a correspondence between each pixel of the scene and the height of the scatterer present inside it, i.e. a DEM. However, in real scenarios the area under test can be characterized by multiple scatterers superimposing their responses in the same resolution cell. As a result, the single-scatterer hypothesis is not sufficient to characterize the radar signal

For instance, in urban areas it would be useful to resolve scattering mechanisms coming from the basis and the top of the buildings, or to separate different layers of man-made structures. In natural areas like forest stands different contributions could come from ground, tree trunks (double-bounce), or canopy (this contribution is generally modeled as *volume scattering*). In these cases, as a result of the combination of multiple contributions, InSAR processing returns just an estimate of a height centroid, being not able to resolve them. The main idea to overcome this limitation is to generate height resolution capability by relying on a synthetic aperture along the cross-range direction. This can be obtained by exploiting information acquired by *K* passes of the radar platform, and combining them in such a way to return a profile of the power backscattered from targets placed at different heights inside the same range-azimuth resolution cell. These kind of techniques of coherent data combination are commonly referred to as SAR Tomography (Tomo-SAR), and they are intrinsically multibaseline. In the last decade, Tomo-SAR has been growing fast, and Tomo-SAR techniques have been developed by different European and not research groups in the SAR community. Papers [5], [12]-[14], [19]-[31] are an incomplete, yet representative, set of references about Tomo-SAR.

Consider the acquisition geometry of Fig. 1.2, where a set of K SAR images is acquired, corresponding to K nominal sensor flight tracks shifted along the cross-range direction. $K-1$ images (*slaves*) are supposed to be co-registered with respect to a reference master. The flat-Earth phase is assumed to be compensated. The complex amplitude received by the k-th sensor of this interferometric array can be

expressed as [22]

$$y_k(x,r) = \iint g(x',r') \int \beta(x',r',z) \exp\left(j \frac{4\pi B_{\perp k} z}{\lambda r} \right) dx' dr' dz \,, \tag{1.12}$$

where $g(x',r')$ is the post-focusing 2-D SAR impulse response, (x,r) are the azimuth-slant range coordinates, $B_{\perp k}$ is the *k*-th baseline orthogonal to the line of flight, λ is the radar wavelength and $\beta(x',r',z)$ the scene reflectivity function. After some manipulations (see [13] and [22] for details), $y_k(x,r)$ can be rewritten as:

$$y_k(x,r) = \int \beta(x,r,z) \exp\left(j \frac{4\pi B_{\perp k} z}{\lambda r} \right) dz \tag{1.13}$$

Equation (1.13) shows that a Fourier relation exists between SAR data and the target projection. Hence, $\beta(x,r,z)$ can be obtained by collecting all the samples $y_k(x,r)$, with $k = 1,\ldots,K$, and performing a Discrete Fourier Transform of the observable vector $\mathbf{y} = \left[y_1(x,r),\ldots,y_K(x,r) \right]^T$ in the height-dependent spatial frequencies domain, as follows [22]:

$$\hat{\gamma}(x,r,z) = \sum_{k=1}^{K} y_k(x,r) \exp\left(-j 2\pi B_{\perp k} \omega_z \right), \tag{1.14}$$

where

$$\omega_z = \frac{2z}{\lambda r} \tag{1.15}$$

is a spatial frequency in the height dimension. Supposing that an uniform baseline distribution is available, let *d* and *L* be the sampling distance and the overall length of the synthetic aperture along the cross-range dimension, respectively. The achievable (geometric) Rayleigh resolution in the *z*-direction is given by [12]:

$$\delta_z = \frac{\lambda r}{2L} \,. \tag{1.16}$$

According to the Nyquist criterion, an upper bound can be found to the sampling distance *d* in order to avoid height ambiguities [12]:

$$d \le \frac{\lambda r}{2\Delta H} \tag{1.17}$$

where ΔH is height interval in which the scattering of the target of interest is included.

At least in principle, the sampling distance should be uniform to properly reconstruct the vertical profiles of the scene. However, due to practical constraints, it is almost impossible to keep a constant baseline separation for all the tracks both in airborne and in the spaceborne acquisitions. Furthermore, the limited number of sensor passes often results in a strongly undersampled observable vector, leading to increasing sidelobes. As a consequence, the imaging quality worsens with respect to the ideal case, in terms of contrast and height ambiguities, as anomalous side and grating-lobes can arise [5], [12], [13], [24]. Many approaches have been proposed in the literature to solve this problem. In particular, research efforts have been spent to cast the problem of the height profile estimation in the more general signal processing framework [12], [13], [22], [23], [26], [27], [30], [31]. Spectral estimation approaches in the array processing

framework have also proposed and successfully tested [5], [13], [23]. In this latter framework, the problem is traced back to the one of finding the best spectral estimator of the intensity distribution in a statistical sense:

$$P_\gamma(z) = E\left\{\left|\gamma(z)\right|^2\right\}. \tag{1.18}$$

Here, the discussion is limited to the most common spectral estimators, which will also be useful for the purposes of this work. The simplest way to do this is to apply a *classical Fourier-based beamforming* (BF) filtering to the observable data vector $\mathbf{y}$ [5], [13], [32]. In a few words, the key idea is to design a filter which passes the spatial frequency of interest undistorted while scanning the spatial bandwidth of interest. More in details, let

$$\mathbf{a}(z) = \left[1, \exp\left(jk_{z,1}z\right), \ldots, \exp\left(jk_{z,K}z\right)\right]^T \tag{1.19}$$

be the so-called K-dimensional *steering vector* for a generic track distribution, whose elements represent the spatial phase history generated by the scatter position in height at the different baselines. The k-th element of the steering vector is given by:

$$\left[\mathbf{a}(z)\right]_k = \exp\left(jk_{z,k}z\right) = \exp\left(j\frac{4\pi B_{\perp k}}{\lambda r}z\right). \tag{1.20}$$

where it has been defined $k_{z,k} = \frac{4\pi B_{\perp k}}{\lambda r}$. $k_{z,k}$ is the height-to-phase conversion factor relative to the k-th baseline; of course, at the master track it results $k_{z,1} = 0$. The N-look estimate[6] of the covariance matrix $\mathbf{R}_y$ of vector $\mathbf{y}$ is given by:

$$\hat{\mathbf{R}}_y = \frac{1}{N}\sum_{n=1}^{N}\mathbf{y}(n)\mathbf{y}^H(n), \tag{1.21}$$

from which the beamforming spectrum can be obtained as [5]:

$$\hat{P}_{BF}(z) = \frac{\mathbf{a}^H(z)\hat{\mathbf{R}}_z^{-1}\mathbf{a}(z)}{K-1} \tag{1.22}$$

The heights of the scatterers in the considered multilook cell are estimated as the heights associated with the highest peaks of $\hat{P}_{BF}(z)$.

Although the BF estimate of (1.22) was used since the early beginning to demonstrate the potentials of the Tomo-SAR principle [19], this spectral estimator does not enjoy good imaging capabilities, due to its low height resolution (which approximately equals (1.16) independently of the baseline sampling) and a low capability to reduce the sidelobe amplitudes. In this scenario, a powerful tool to improve the estimation performance is the nonparametric data-adaptive Capon filter, hereafter referred to as *Adaptive Beam Forming* (ABF), firstly proposed for Tomo-SAR in [23] and extensively experimented in [13]. ABF is based on the filtering of the observable vector through a complex finite impulse response (FIR) filter $\mathbf{h}(z)$ of order K, in such a way to leave undistorted the signal at height z and to reject all the other contributions different from the one of interest. From an algebraic point of view, the filter is designed in order to solve the following

[6] The expression in (1.21) coincides with the maximum likelihood estimate of the data covariance matrix in the case in

optimization problem [32]:

$$\min_{\mathbf{h}(z)} \mathbf{h}^H(z)\hat{\mathbf{R}}_y\mathbf{h}(z) \text{ subject to } \mathbf{h}^H(z)\mathbf{a}(z)=1. \tag{1.23}$$

The filter impulse response optimizing (1.23) can be expressed as:

$$\mathbf{h}(z)=\frac{\hat{\mathbf{R}}_y^{-1}\mathbf{a}(z)}{\mathbf{a}^H(z)\hat{\mathbf{R}}_y^{-1}\mathbf{a}(z)}, \tag{1.24}$$

and the resulting ABF estimator of the intensity distribution is given by

$$\hat{P}_{ABF}(z)=\mathbf{h}^H(z)\hat{\mathbf{R}}_y\mathbf{h}(z). \tag{1.25}$$

The data-adaptivity of the Capon filter is apparent from (1.24) and (1.25), and it allows to improve 3-D imaging quality, to imrove the height resolution and to increase the peak sidelobe level with respect to the BF estimator [23]. Thanks to its sidelobe suppressing capabilities, in the last years ABF has been deeply employed in Tomo-SAR applications and its efficiency has been tested both with simulated data and with real data sets, becoming a standard imaging method as a matter of fact.

1.6 The MB phase calibration problem

Being a radar-based technique, the SAR MB processing is based on multiple delay measurements, converted into distances by multiplying them for the propagation velocity of the electromagnetic wave into the medium. Due to atmospheric disturbances, the propagation conditions are subjected to changes both during the same acquisition and between different passes. This results in random variations of the measured delay and, as a consequence, of the measured sensor-targets distances [33]. Moreover, under realistic conditions, in airborne acquisitions the effective flight tracks deviate from the nominal trajectories, due to the uncertainty which unavoidably affects the Global Positioning System (GPS), resulting in baseline estimation errors. The first kind of error becomes significant in space borne SAR applications, due to the role played by the ionosphere, whereas the second type is strictly related to airborne SAR acquisition geometries. Although these disturbances come from different phenomena, both can be handled as the result of uncompensated propagation delays of the radar echoes as they travel back to the SAR sensor [33]-[34]. More in details:

- *atmosphere propagation delays*: let $d_k(x,r)$ be the atmospheric one-way path delay in λ-units.

  The phase error at each baseline is simply given by:

  $$\psi_k(x,r)=4\pi d_k(x,r); \tag{1.26}$$

- *baseline estimation errors*: let $\Delta z_k(x,r)$ and $\Delta\eta_k(x,r)$ be the *k*-th baseline error components in the vertical and horizontal direction, respectively, in the height-ground range plane for fixed azimuth-range coordinate (x,r). The corresponding uncompensated baseline error in the line-of-sight direction is given by:

---

which the data vector is complex Gaussian.

$$\Delta B_{\perp k}(x,r) \approx \sin\left[\theta(r)\right]\Delta\eta_k(x,r) - \cos\left[\theta(r)\right]\Delta z_k(x,r) = \frac{\lambda}{4\pi}\psi_k(x,r). \tag{1.27}$$

As a consequence, the phase error at each baseline can be written again as:

$$\psi_k(x,r) = 4\pi\Delta B_{\perp k}(x,r) = 4\pi d_k(x,r). \tag{1.28}$$

We can then conclude that $\psi_k(x,r) = 4\pi d_k(x,r)$ is a model of the phase error which embeds all the possible phase errors which can be found in airborne and spaceborne acquisitions. The quantities $\left\{d_k(x,r)\right\}_{k=1}^{K-1}$ can be statistically modeled as a set of independent random variables [33], [35]. A reasonable choice is $\mathbf{d}(x,r) \sim N\left(0,\sigma^2(x,r)\mathbf{I}\right)$, i.e. a set of independent real-valued Gaussian variables, where $\mathbf{d}(x,r)$ is a $(K-1)$-dimensional vector whose elements are $\left\{d_k(x,r)\right\}_{k=1}^{K-1}$. Analogously, it results $\boldsymbol{\psi}(x,r) \sim N\left(0,\sigma_\psi^2(x,r)\mathbf{I}\right)$, where $\boldsymbol{\psi}(x,r)$ is a $(K-1)$-dimensional vector whose elements are $\left\{\psi_k(x,r)\right\}_{k=1}^{K-1}$ Accounting for these disturbances, the MB observable vector can be written as:

$$\mathbf{y}(x,r) = \mathbf{y}_0(x,r) \odot \mathbf{e}(x,r) \tag{1.29}$$

where $\mathbf{y}_0(x,r)$ represents the perfectly calibrated MB data vector and "$\odot$" indicates the Hadamard product, performing an element by element product. Furthermore, assuming the first image to be the master, it results:

$$\left[\mathbf{e}(x,r)\right]_n = \begin{cases} 1, \text{ for } n=1 \\ \exp\left(j4\pi d_k(x,r)\right), \text{ for } k = n-1 = 1,\ldots,K. \end{cases} \tag{1.30}$$

It is easy to show the impact of phase errors by rearranging (1.14) as follows [33]:

$$\begin{aligned} \hat{\gamma}(x,r,z) &= \sum_{k=1}^{K} y_k(x,r)\exp\left(-j2\pi B_{\perp k}\omega_z\right) = \\ &= F\left\{y_{0,k}(x,r)\exp\left[je_k(x,r)\right]\right\}, \end{aligned} \tag{1.31}$$

where $F\{\cdot\}$ denotes the imaging operator. Apparently, the disturbance effect results in an image defocusing due to the convolution of the desired projection with the Fourier transform of $\exp\left[je_k(x,r)\right]$ [33]. The effect of these phase contributions is severe in tomographic applications, leading to a strong worsening in the estimation of the vertical profiles which are characterized by a loss of height resolution and inflated sidelobes. To get a flavor, in Fig. 1.3 these effects are shown by means of simulated data, as reported in [13]. The data vector received from a point-like scatterer located at zero height and with very high signal-to-noise ratio has been simulated according to the signal model reported in [21]. Residual path delays have been simulated as independent Gaussian random variables with standard deviation 0.04λ. The BF and ABF spectral estimators have been considered, and the obtained profiles have been reported in dB with respect to the peak amplitude. It is apparent that the effects of the miscalibration are almost negligible in the BF profile, while they have detrimental effects on the ABF one, which exhibit a much lower peak sidelobe level and a reduced mainlobe width with respect to the error-free case. In fact, due to its data adaptive features, the ABF estimator is known to be very sensitive to residual miscalibrations. As a matter of fact, despite its better

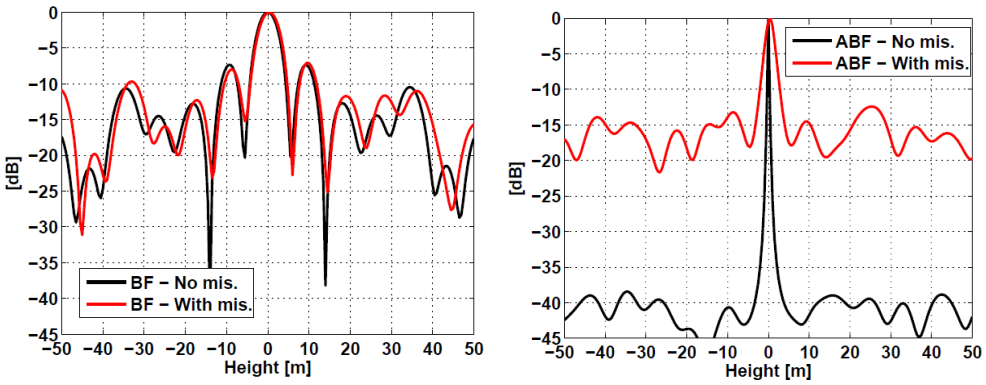

Figure 1.3 – Examples of estimated vertical profiles of the backscattered power, in absence and in presence of phase mismatch for a single scatterer at zero height (reproduced from [13]). Left panel: BF; right panel: ABF.

performance with respect to a traditional BF filter, in presence of phase errors the ABF filter could see the useful spatial harmonics as interfering contributions and reject them instead of leave unaltered. As a consequence, the filter will not be able anymore to preserve the *sharpness* of the profile, with also a loss of radiometric fidelity, i.e. the main lobe amplitude do not correspond to the real backscattered power. A common way to mitigate this phenomenon, commonly referred to as *self-cancellation,* is to apply a diagonal loading of the observable covariance matrix, in order to simulate a fictitious increase of the data noise level and limit the adaptivity of the ABF filter, at the cost of reduced super resolution and sidelobe suppression. However, the diagonal loading cannot be thought as method solving at the root the problem of phase calibration, i.e. MB data must be properly phase calibrated before being processed. In other words, the diagonal loading can only be seen as a feasible way to make ABF robust to miscalibration residuals.

A final remark is in order. Until now, the discussion about phase calibration was focused on the tomographic processing. It should be noted that MB data need a careful phase calibration before *any* processing, as residual miscalibration can impair any following parameter estimation procedure.

1.7 Objective of the report

The objective of this work is to propose and test a new method in order to calibrate in phase a MB data set. In particular, the performance of the proposed processing chain will be assessed by processing a simulated and real MB data set, over forest scenarios for tomographic applications.

This report is structured as follows.

In Chapter 2 the calibration problem will be addressed in the framework of the array signal processing, showing the main theoretical developments available in literature. In particular, theoretical limits of phase estimation will be discussed and study case of interest will be placed in this context. Then, an overview of the main available calibration methods in MB SAR processing will be given, pointing out their pro and cons. The proposed method will be presented and its advantages with respect to the existing techniques will be discussed.

In Chapter 3 a performance analysis with simulated airborne L-band data will be carried out and its results will be shown. In particular, firstly each part of the proposed processing chain will be analyzed individually and then the performance of the whole algorithm will be evaluated. Performance analysis with

both uniform and non-uniform baseline configurations will be presented.

In Chapter 4 the performance analysis will be carried out with a real E-SAR data stack acquired over the forest site of Traunstein (Germany) and the results will be presented. The results of a comparison with the other calibration techniques will be shown.

Finally, Chapter 5 will draw some conclusions and some guidelines for future developments and improvements will be suggested.

CHAPTER 2

MB PHASE CALIBRATION

2.1 Theoretical limits of phase calibration

To investigate the theoretical limits of the MB phase calibration, it is worth remembering the parallelism between MB processing and multicomponent array signal processing [5]. Many authors faced the issue of source localization using a sensor array whose effective trajectories were affected by random displacements with respect to the nominal ones. In this last framework, the phase calibration problem has been deeply studied since the '80s, and can be formally stated as the estimation of a set of unknown parameters (i.e. the calibration phases) relying on some kinds of auxiliary information, if available. In particular, in a seminal paper of 1987 Y. Rockah and P. Schultheiss derived Cramer-Rao lower bounds[1] (CRLB) on calibration and source location accuracy achievable with far-field radiating sources whose positions are not initially known [37]. They proved that the calibration becomes possible only when the number of sources exceeds a certain minimum and when the relative geometry between the sources and the array avoids certain particular configurations.

Following the discussion in [37], in Fig. 2.1 the geometry of acquisition of a sensor array with uncertainty in sensor location is shown. This array represents the classical MB acquisition geometry (with angles and distances not in scale) in the classical reference system in the ground range, azimuth, height space at fixed azimuth coordinate. A second orthogonal reference system (x, y)[2] is then defined in the ground range-height plane, to which the coordinates of the sensor positions are referred. White circles identify the nominal positions of the antennas, while the black circles identify the actual ones. Without loose of generality, for the sake of simplicity x axis is parallel to the ground range axis. α_j indicates the so-called

[1] Information theory states that any unbiased estimator has an error variance greater than or equal to the CRLB value, at least in asymptotic conditions (i.e. high number of observables and high signal to noise ratio) [38].

[2] Notice that with a slight abuse of notation same symbols have been used to indicate quantities which are different with respect to Chapter 1. In the Author opinion, this non considered a limit, as quantities have been defined unambiguously in the text. Moreover, this abuse of notation is limited only to this section.

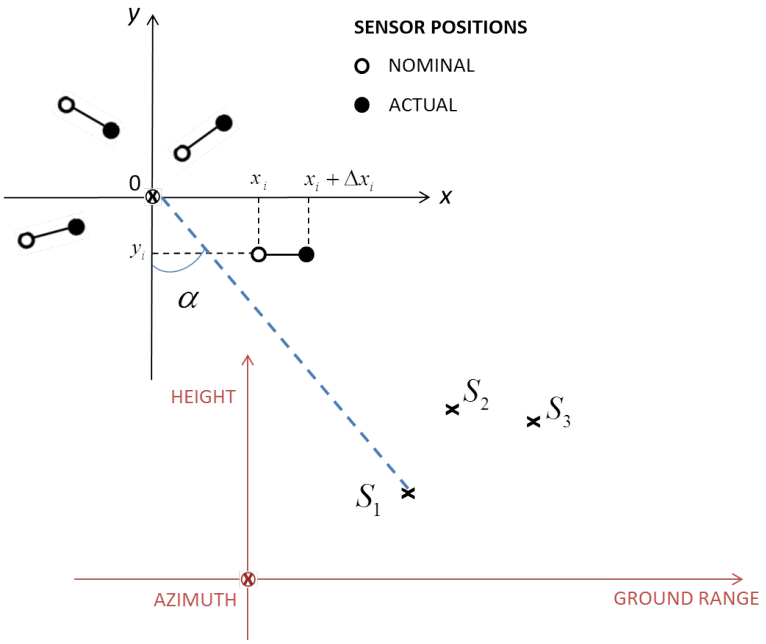

Figure 2.1 – Geometry of estimation problem examined by Rockah and Schultheiss in [37], re-casted to a MB acquisition geometry.

bearing of the j-th source, i.e. an angle measured with respect to the *y*-axis. Moreover, for the sake of simplicity, we suppose that scatterers are point-like. No hypotheses are made about their number in the same cell. Nevertheless, the analysis could be generalized also to non point-like scatterer by means of the hybrid CRLB derived in [39] with the same conclusions.

Let $(\Delta x_i, \Delta y_i)$ be the random, time-invariant, displacements of the i-th sensor with respect to its nominal track (x_i, y_i). The displacements are modeled as independent zero-mean Gaussian random variables with standard deviation σ. In the analysis of [37], three different cases have been examined, depending on the number of unknown parameters, which are reported in the following subsections 2.1.1, 2.1.2 and 2.1.3.

2.1.1 Known location of one sensor and direction from that sensor to a second sensor

In parallel with MB SAR, supposing known the location of one sensor is equivalent to choose the position of the first sensor as the master track and to estimate the relative locations of the other sensors (i.e. the slave tracks) with respect to this one.

If a second assumption stands that the direction from a master track to a second track is known, the problem geometry can be simplified by placing the *x*-axis in correspondence of the sensor whose direction relative to the first one is known, as shown in Fig. 2.2 where a three-sensor array configuration is depicted. The following discussion is focused on a 3-sensor case, but it can be generalized to a set of *K* antennas by considering 3-sensor subsets, each one composed by any two of already calibrated sensors and a third one in unknown location, in order to form a three-element structure satisfying the same assumption. In this case, it results respectively from the two assumptions

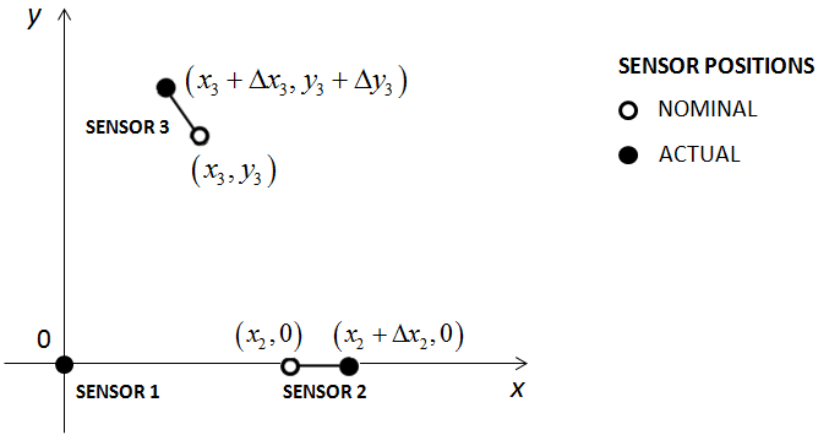

Figure 2.2 – Three-sensor array configuration with known location of one sensor and direction from that sensor to a second sensor.

$$x_1 = y_1 = \Delta x_1 = \Delta y_1 = 0\,, \tag{2.1}$$

and

$$y_2 = \Delta y_2 = 0\,, \tag{2.2}$$

so that the unknown parameters reduces to

$$(\alpha_i, \Delta x_2, \Delta x_3, \Delta y_3)\,. \tag{2.3}$$

It can be demonstrated that the CRLB on the uncertainty in sensor positions is upper-bounded as follows:

$$CRLB\left(\Delta x_2, \Delta x_3, \Delta y_3\right) \le \mathbf{M}^{-1} \tag{2.4}$$

where $\mathbf{M}$ is a matrix which is a function of *SNR*[3], nominal sensor position coordinates, source bearing (direction of arrival) and the standard deviation σ of the sensor unknown displacements with respect to the nominal positions. It can be proved that $CRLB\left(\Delta x_2, \Delta x_3, \Delta y_3\right) \to \mathbf{0}$ when $SNR \to \infty$ unless $\mathbf{M}$ is singular [37]. It has been demonstrated that $\mathbf{M}$ is singular when the shape of the array is linear and/or at least three non-collinear sources cannot be found. As a consequence, in this case, with the exception of particular array and/or source configurations, the estimation of the displacements can be achieved with an arbitrary degree of accuracy by increasing the *SNR*.

2.1.2 Known location of one sensor

This study case corresponds to the MB SAR acquisition case, in which the known sensor is assumed to belong to the master track and no other assumptions are made on the other sensor positions, i.e. a directional reference is not available anymore. Referring to Fig. 2.3, for simplicity one can place the master sensor on the reference system origin and the nominal position of the second sensor on the *x*-axis. As a consequence, an angle ϕ between the *x*-axis and the actual position of the second sensor can be defined to

[3] The signal-to-noise ratio (*SNR*) is defined as the ratio between the power of the information signal and the power of the noise, measured in correspondence of the receiver. Here, for the sake of simplicity, we can refer to a mean of the SNRs measured on the *K* sensors.

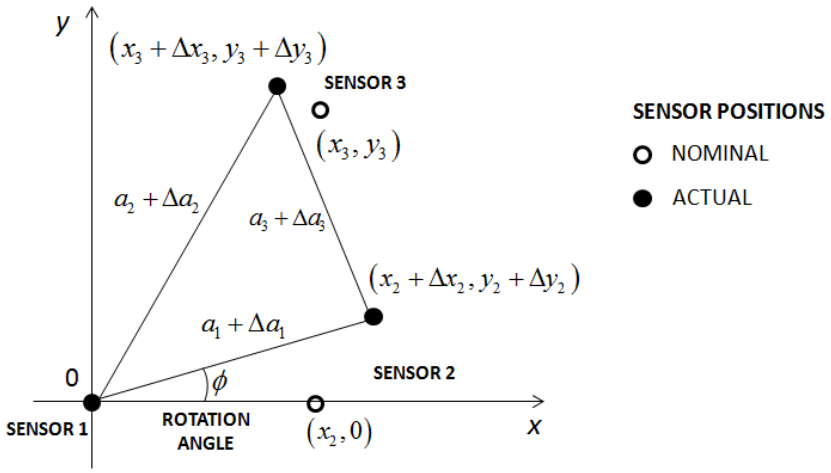

Figure 2.3 – Three-sensor array configuration with known location of one sensor.

indicate a rotation ambiguity of the actual sensor distribution. The problem can then be rewritten in terms of the estimation of the following unknown parameter set:

$$\mathbf{p} = \left[L_1, L_2, L_3, \phi\right]^T, \tag{2.5}$$

where, with reference to Fig. 2.3,

$$\begin{aligned} L_1 &= \frac{1}{2}a_1^2 = \frac{1}{2}\left(x_2^2 + y_2^2\right), \\ L_1 &= \frac{1}{2}a_2^2 = \frac{1}{2}\left[\left(x_3 - x_2\right)^2 + \left(y_3 - y_2\right)^2\right], \\ L_3 &= \frac{1}{2}a_3^2 = \frac{1}{2}\left(x_3^2 + y_3^2\right), \\ \phi &= \tan^{-1}\left(\frac{\Delta y_2}{x_2 + \Delta x_2}\right). \end{aligned} \tag{2.6}$$

If $\Delta\mathbf{p} = \left[\Delta L_1, \Delta L_2, \Delta L_3, \phi\right]^T$ are the uncertainties in the estimation of the sensor positions with respect to the master track, the desired CRLBs are given by:

$$\lim_{SNR\to\infty} CRLB\left(\Delta\mathbf{p}\right) = \sigma^2 \begin{bmatrix} \mathbf{0}_{3\times3} & \mathbf{0}_{3\times1} \\ \mathbf{0}_{1\times3} & \left(x_2^2 + x_3^2 + y_3^2\right)^{-1} \end{bmatrix}, \tag{2.7}$$

where $\mathbf{0}_{M\times N}$ indicates a (M, N)-dimensional matrix full of zeros. In the general case of K sensors, the bound on the orientation ϕ can be easily developed, at least asymptotically:

$$\lim_{SNR\to\infty} CRLB\left(\phi\right) = \frac{\sigma^2}{\sum_{i=2}^{K} r_{1i}^2} \neq 0, \tag{2.8}$$

where r_{1i} is the nominal distance of the generic *i*-th sensor from sensor 1, given by:

$$r_{1i} = \sqrt{x_i^2 + y_i^2}\ . \tag{2.9}$$

Equations (2.7) and (2.8) show that in this study case three scatterers of sufficient strength can calibrate the array shape to any desired degree of accuracy, but even a large number of sources (in unknown locations)

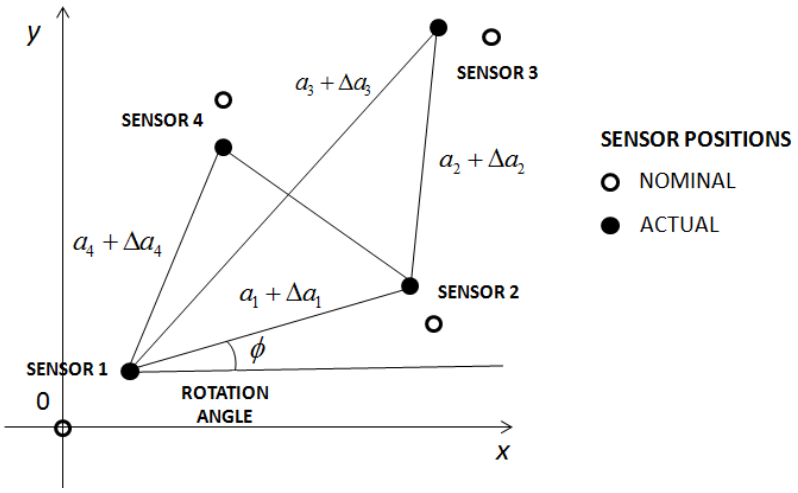

Figure 2.4 – General array geometry in the case that no sensor positions are known.

cannot resolve a rotational ambiguity in array location. There will remain a residual component of bearing error due to sensor location uncertainty even when the SNRs of the calibrating sources are arbitrarily high [16]. This is valid independently from the array shape. In a MB SAR framework, the array rotational ambiguity corresponds to an unknown additional phase ramp along the baselines, which in turn corresponds to an height shift. According to [37], this residual interferometric array rotation could be minimized e.g. by choosing the origin on a sensor at one extreme of the array as remote as possible from other sensors. This is apparent from (2.8). However, this degree of freedom could not be available in MB SAR.

2.1.3 All sensors locations are unknown

In this scenario, the origin of the coordinate system can be placed at the nominal location of the first sensor, as shown in Fig. 2.4. In the general case of K sensors the unknown parameter vector becomes:

$$\Delta\mathbf{p} = \left[\Delta x_1, \ldots, \Delta x_K, \Delta y_1, \ldots, \Delta y_K, \phi\right]^T . \tag{2.10}$$

It can be demonstrated [37] that in high *SNR* conditions the array geometry can be determined only up to a rotation angle ϕ and a translational shift $\left(\Delta x_1, \Delta y_1\right)$ corresponding to the uncertainty affecting the knowledge of the master track. Anyway, an exhaustive treatment of this case is out of scope, since this is not the case of MB applications.

2.1.4 Calibration algorithms in the array processing literature

In 1994 Viberg and Swindlehurst [40] exploited a Bayesian approach to the self-calibration[4] problem. They found that in principle, without relying on any assumption about the array shape (i.e. linear or circular), self-calibration is possible if prior information is available. In this way, rotation ambiguities can be removed (see Section 2.1.2) to a certain degree of accuracy without posing constraints on the distances between the master element and the others elements of the array. In particular, they verified the efficiency of

[4] Generally speaking, the term *self-calibration* refers to the possibility to calibrate a data set by using the set itself. In the following of this work, this expression is used to point out how the proposed method does not rely on external information to estimate the phase errors, but it acts as a *blind* technique and the only corrupted stack is employed to

their method in enabling the simultaneous estimation of all the parameters of interest when the variance of perturbations is low, allowing the linearization of the phase error. Many approaches to face the problem have been carried out and a number of calibration methods have been proposed in literature. In general, a pre-processing step is needed in order to retrieve prior information to be exploited so that the number of unknown parameters can be reduced and the estimation performance improves. For further information, the interested reader can refer to [40]-[42] and references therein. It is worth noting that in the mentioned works, the calibration targets are assumed not to decorrelate from acquisition to acquisition. In the MB SAR framework this is almost equivalent to scattering from man-made structures, while it is not true when observing volume and/or temporal decorrelating scenarios.

2.2 Available calibration methods in MB SAR

The phase calibration problem is known since the very beginning of InSAR, and an intensive research on this topic has been carried out in the last 20 years. Here, the literature review is limited only to those contributions which have been specifically designed for MB SAR. From a signal processing point of view, the MB phase calibration can be carried out by following two different classes of algorithms. A first class makes use of a grid of targets of opportunity which remain stable during the entire acquisition time span. On the other hand, a second class of algorithms is based on some kind of MB autofocus.

Concerning the first class, the simplest method consists in phase-locking the data on a reference point. As the name itself suggests, a very stable reference point in the acquisition area is employed; generally it is a corner reflector (CR) of which the exact location (x_0, r_0) is known. Let z_0 be the height of the CR, known as well. Assuming $k_{z,k}$ and the phase errors constant (or at least very slowly varying) in range and in azimuth on the whole image stack, the phase of a generic point *P* with respect to the one of the CR (located in point P_0) can be obtained as follows:

$$\Delta\varphi_k^P = \varphi_k^P - \varphi_k^{P_0} = k_{z,k}\Delta z^P . \tag{2.11}$$

The method is easy to be implemented, the computational time is null, it does not need for multi-polarimetric data sets (a single channel can be employed) and assures good performance in height estimation with respect to z_0. Unfortunately, in airborne SAR applications the vertical wavenumber depends on the looking angle. As a matter of fact, the target-platform distance is too small to neglect the variations of the incidence angle along the whole image and the space-varying geometry leads k_z to be variable too. As a consequence, (2.11) has to be rearranged as follows [33]:

$$\Delta\varphi_k^P = k_{z,k}^P\Delta z^P + \Delta k_{z,k}^P z_0^{P_0} . \tag{2.12}$$

Therefore, due to the additional term in (2.12), different estimates would be obtained by choosing different reference points, a condition which bounds the method performance and hinders its employment in airborne applications when the carrier frequency gets higher (e.g. when operating at L-band) [33]. It should also be

extract the required information.

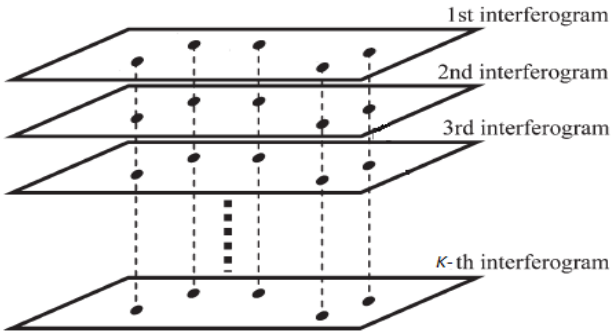

Figure 2.5 – Detection of the PSs in an interferogram set: concept scheme.

considered that the phase error varies in space, which constitutes a limitation for CR-based calibration also for spaceborne acquisitions.

All in all, it has been shown experimentally that at very long wavelengths (e.g. P-band) the CR-based calibration is effective until a maximum distance from the CR of about 500m [13]. This distance is expected to decrease with L-band. As a consequence, a grid of CRs would be an optimal solution, which is actually unfeasible. To circumvent this shortcoming, a feasible way is to detect stable (*viz.* persistent) targets in the observed scenario. This method was firstly developed in [43] and it is nowadays an operational tool for calibration and subsidence motion estimation in urban scenarios with spaceborne data. In [33], it has been experimented also in forest scenarios with P-band airborne acquisitions. A persistent scatterer (PS) is defined as an amplitude and phase stable scatterer, where the concept of stability is referred to the whole MB stack. The way in which the PS detection algorithm operates is reported in Fig. 2.5. In a first step, the dispersion factor has to be calculated for each pixel of the image, defined as:

$$D(x,r)=\frac{\mu_A(x,r)}{\sigma_A(x,r)}, \tag{2.13}$$

where $\mu_A(x,r)$ and $\sigma_A(x,r)$ are respectively the mean and the standard deviation of the MB-varying amplitudes of the pixel at coordinates (x,r). The pixels whose dispersion factors are higher than a fixed threshold are classified as Persistent Scatterer Candidates (PSCs). Then, for each PSC the ensemble coherence is evaluated as follows:

$$\gamma_{ensemble}(x,r)=\max_{z}\ \frac{1}{K}\left|\sum_{k=1}^{K}\exp\left[\varphi_k(x,r)-k_{z,k}z\right]\right| \tag{2.14}$$

where $\varphi_k(x,r)$ is the phase of the pixel at coordinates (x,r) in the k-th image [10]. The PSCs whose ensemble coherence is higher than a threshold are finally declared to be PSs. The evaluation of $\gamma_{ensemble}(x,r)$ is needed both to select the PSs from the subset of PSCs and to find the corresponding height estimates. In this way a sparse grid of phase error estimates is built as

$$\hat{\psi}_k(x_0,r_0)=\varphi_k(x_0,r_0)-k_{z,k}(x_0,r_0)\hat{z}(x_0,r_0), \tag{2.15}$$

where $\hat{z}(x_0,r_0)$ are the height estimates from (2.14), being (x_0,r_0) the coordinates of the PSs. At this point, a 2-dimensional interpolation is needed to obtain the error estimates for the whole image.

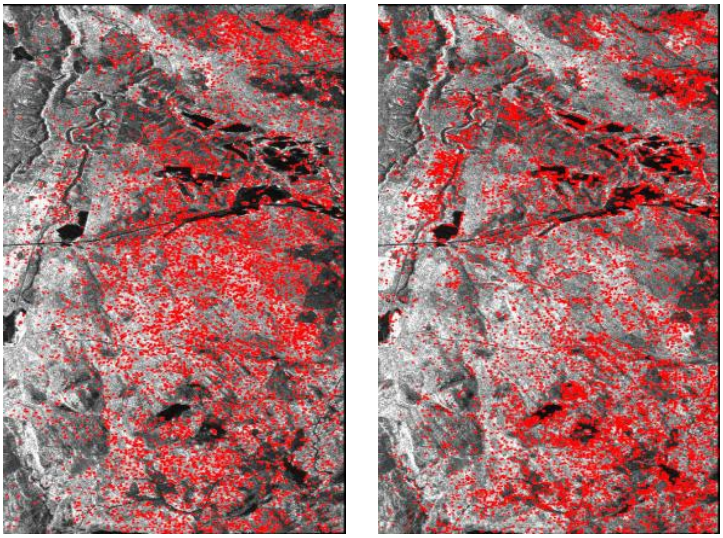

Figure 2.6 – Red points: detected stable targets over Krycklan (Sweden). Range direction is on the horizontal axis. Left panel: CS map. Right panel: PS map (reproduced from [34]).

In [34], a similar method has been introduced, based on the detection of a set of reliable targets as well. The main difference with respect to the previous technique stands in the selection criterion of the most reliable scatterers, which in this case are named Coherent Scatterer (CSs). A way to detect CS is based on the calculation of two (or even more) sublook spectra for each image in the MB stack. Then, the coherence of the sublook images is computed for each track, and the sublook coherences averaged. Only those pixels whose average sublook coherence exceeds a fixed threshold will be selected as CS candidates (CSCs). The subsequent estimation of the phase errors proceeds as in the PS case.

A comparison between the PS and the CS techniques has been carried out in [34] by processing a multibaseline PolInSAR L-Band dataset acquired by the DLR E-SAR airborne system. The stack is composed by 6 fully polarimetric images obtained in repeat-pass InSAR mode, acquired in 2008 over the boreal forest area of Krycklan (Sweden) in the frame of the ESA project BioSAR-2. Fig. 2.6 shows the locations of the calibration targets (the threshold values have been chosen in order to obtain the same number of PSs and CSs). It is apparent that the distribution of PSs is range dependent (more detections in far range due to the range dependency of the dispersion factor), whereas no dependencies can be observed in the CS displacement. Furthermore, only 20 points have been found in common, suggesting the possible application of both detection methods in cascade to increase the number of reliable calibration points.

Some comments are in order. First of all, the detection performance of targets of opportunity exhibit a non-negligible dependency on the selection of the threshold to be applied to the test statistic, and no rule-of-thumb exists. A small threshold values could lead to the detection of unreliable scatterers (false alarms), whereas a too high value would not allow to find a proper number of PSCs/CSCs for the calibration processing (missed detection). In other words, a trade-off exists between false alarm minimization and number of PS/CS detected. Actually, this feature could potentially impair the use of every methods based on targets of opportunity. Moreover, a low number of available acquisitions (in the order of 5 or less, as typically happens in temporal decorrelating scenarios) can constitute a limiting factor for the detection

performance even in the case in which the threshold is optimally selected. Furthermore, independently from the goodness of the detection, the final calibration performance is strongly scenario-dependent. In fact, PS/CS techniques are deeply employed and perform well when the number of detected PS/CS is high and when their spatial distribution is dense enough to account for the spatial variability of the calibration phases. For this reason, they appear to be suitable to calibrate data acquired over urban environment, reaching high calibration accuracy, as the buildings and the other man-made structure constitute a rich source of stable scatterers. This effectiveness has been demonstrated with different carrier frequencies and different sensors. The situation is different in natural areas. In fact, the scattering e.g. from a forest stand has a volumetric contribution that, depending on carrier frequency, can mask out coherent scattering mechanisms coming from the interaction between ground and tree trunks, thus reducing the number of detections. This problem becomes more significant with L-band acquisitions with respect to P-band acquisitions [44]. As a consequence, the spatial density of calibration targets worsens as well.

To sum up, two limitations affect the calibration methods relying on targets of opportunity: the implementation of the detection step, and the resulting spatial density of the detected targets. For this reason, research efforts have been spent in the development of a second class of algorithms, i.e. those performing a MB autofocusing (or self-calibration) independently of the kind of scattering in the cell under analysis. As a consequence, no detection is needed and the spatial coverage becomes (almost) full.

In [45] a method is proposed which is based on a statistical approach relying on the maximization of a likelihood function. The main assumption is that the phase offset to be estimated is constant along the single image[5], while it varies from acquisition to acquisition. $K-1$ interferograms are calculated from the MB stack, and M pixels exhibiting the highest coherence values are considered. In the hypothesis that a single powerful scatterer is present for each of them, the unknown height vector $\mathbf{z}_M = \left[z_1,\ldots,z_M\right]^T$ is considered in which the heights of the scatterers in the selected cells are contained. The phases of the selected scatterers can be written as:

$$\phi'_{m,k} = \phi_{m,k} + \psi_k \text{, for } m = 1,\ldots,M \text{ and } k = 1,\ldots,K-1. \tag{2.16}$$

where ψ_k is the constant phase error (to be estimated) for the k-th interferogram, and $\phi_{m,k}$ is the interferometric phase signal corresponding to the m-th pixel of the k-th interferogram [13]. From (2.16), the estimation problem is well-posed as the number of unknowns is $M+K-1$ and the available observables are $M(K-1)$. In order to estimate the phase offsets ψ_k, a Maximum Likelihood (ML) approach can be followed. If we assume the observed phase values to be statistically independent from pixel to pixel and from acquisition to acquisition, the likelihood function can be factorized as follows [45]:

$$L\left(\phi', \mathbf{z}_M \left| \boldsymbol{\psi} \right.\right) = \prod_{k=1}^{K-1}\prod_{m=1}^{M-1} f\left(\phi'_{m,k}, z_m \left| \psi_k \right.\right), \tag{2.17}$$

[5] Notice that this not a limitation, as the images can be divided into range-azimuth areas in which the phase error can be assumed constant.

where $f\left(\phi'_{m,k}, z_m \middle| \psi_k\right)$ is the single likelihood function for the *m*-th pixel of the *k*-th interferogram, and $\boldsymbol{\psi} = \left[\psi_1, \ldots, \psi_{K-1}\right]^T$ is the unknown phase offset vector [see (1.28)]. Thus, the phase errors are estimated by maximizing expression (2.17) with respect to $\boldsymbol{\psi}$:

$$\hat{\boldsymbol{\psi}} = \arg\max_{\boldsymbol{\psi}} \; L\left(\boldsymbol{\phi}', \mathbf{z}_M \middle| \boldsymbol{\psi}\right). \tag{2.1}$$

If the vector $\mathbf{z}_M$ is known, the ML estimation can be decoupled in $K-1$ scalar maximization problems which have a lower complexity than the initial optimization problem. Unfortunately, this is not always true, and a more complex iterative solution should be adopted, e.g. involving an assumption on the prior distribution of the height vector. This algorithm looks not to be completely suitable for Tomo-SAR applications. In fact, in general the a-priori knowledge of the *M* heights could not be available, thus increasing the complexity of the estimation problem with nuisance parameters. Moreover, the method still rely on the detection of a set of single scatterers, thus not really overcoming the limitations of PS/CS-based algorithms. Last but not least, the hypothesis of (almost) constant phase errors on a range-azimuth area is more likely to be verified in spaceborne data for the very high spatial correlation of the athomospheric path delay.

In [46], an algebraic approach has been proposed with particular reference to forest scenarios (the most challenging ones), and it has been called 'ALGAE'. Through an algebraic decomposition of the MB-multipolarimetric covariance matrix [29], the ground scatterer can be separated from the volume. In this way, an autofocusing on the ground scatterer can be carried out. In brief, the ALGAE algorithm enjoys the following advantages with respect to the existing methods. First of all, the solution takes account of the spatial variability of $k_{z,k}$. Secondly, no detection of particular scatterers is needed. Thus, the performance is affected by neither false/missed detections nor the spatial density of reliable scatterers, and the method results to be scenario-dependent at a much lower extent. To perform well, ALGAE needs a clear distinction between the ground scatterer and the volume contribution, although it could not happen in natural scenarios with a dense vegetation cover and/or a poor height resolution of the acquisitions. To counteract this possible shortcoming, some kind of spatial interpolation and averaging procedures can be employed, possibly relying on a set of PS, if available [47]. Moreover, a two dimensional phase unwrapping has to be performed of the ground phases, with a non-negligible computational load. Finally, a fully polarimetric MB data set is needed to separate the ground scatterer from the volume scattering contribution.

In [48], a MB technique has been conceived which maximizes an ad-hoc defined contrast of the vertical profiles estimated in the area under test. The use of vertical profiles independently of the imaged scatterers makes this method to be scenario-independent. In brief, an area of interest in the imaged scene is selected, and the ABF tomograms are calculated for each pixel, and by applying to the data a baseline-dependent phase correction $\phi_{OFF,k}$, $k = 1, \ldots, K-1$. As a result, a set of vertical profiles $P\left(\boldsymbol{\phi}_{OFF}\right)$ can obtained as a function of the correction offset and in a range-azimuth area. Supposing that the imaged scene is homogeneous in range-azimuth, some statistics of the spectral amplitudes can be derived as a function of $\boldsymbol{\phi}_{OFF}$. In this way, a *tomographic contrast* is obtained as:

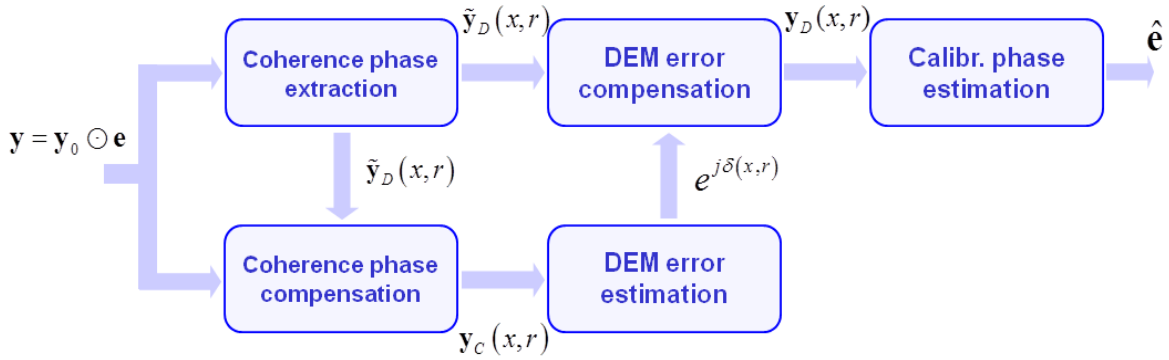

Figure 2.7 – Block scheme of the proposed calibration chain.

$$f(\boldsymbol{\phi}_{OFF}) = \frac{std\left[P(\boldsymbol{\phi}_{OFF})\right]}{mean\left[P(\boldsymbol{\phi}_{OFF})\right]}. \tag{2.19}$$

Thus, the phase correction can be chosen as the one maximizing the contrast in (2.25), i.e.:

$$\hat{\boldsymbol{\phi}}_{OFF} = \arg\max_{\boldsymbol{\phi}_{OFF}} f(\boldsymbol{\phi}_{OFF}). \tag{2.2}$$

This method has the remarkable advantage of fully exploiting the whole amplitude-phase information contained in the MB stack to estimate the phase errors. However, although the method has not been fully experimentd, the contrast measure looks to be very dependent on the dimension of the used range-azimuth window employed to calculate the spectral statistics, i.e. on the variability of the scattering characteristics in the cell under analyis.

From this literature review, it is apparent that until now no definitive solution exists for the MB phase calibration, having each solution their own pros and cons. In particular, a strong scenario dependency has been observed as a common feature. The presented work is intended to give its contribution on this topic by proposing a new calibration chain with the following advantages: (*i*) it acts as *blind* technique avoiding the detection of targets of opportunity or autofocusing on a particular scatterer, i.e. it fully exploits the information in the vertical profile; in this way it accounts for the spatial variability of the phase errors without being dependent on the features of the imaged scenario, and it enjoys a full processing coverage; (*ii*) unlike the technique described in [48], the proposed method works as a coherent processor and it directly maximizes the profile contrast according to a formulation from the information theory; (*iii*) unlike [45], no statistical models are assumed; (*iv*) the proposed method is able to operate also with single polarization data. Nevertheless, the four mentioned advantages are obtained at the cost of a non-negligible computational load.

2.3 The proposed calibration chain

The proposed processing chain exploits the low variability in the range-azimuth directions of the phase errors $\boldsymbol{\psi}(x,r)$. The calibration chain, schematically depicted in Fig. 2.7, is composed by the steps discussed in detail in the following.

Step 1

The first step consists in the calculation of the interferogram at each baseline with respect to the master image. Supposing that the multilook extent is such that the phase errors remain unaltered, the following complex signal is obtained:

$$\tilde{\mathbf{y}}_D(x,r) = \exp\left[j\mathbf{k}_z(x,r) z_0(x,r) \right] \odot \exp\left[j\boldsymbol{\delta}(x,r) \right] \odot \mathbf{e}(x,r). \tag{2.21}$$

where $\mathbf{k}_z(x,r)$ is the *K*-dimensional vector containing the vertical wavenumber for each baseline, $z_0(x,r)$ is the height of the dominant scatterer (i.e. the DEM height), and $\boldsymbol{\delta}(x,r)$ is a set of *K* phases resulting from the incoherent estimation of the DEM along the baselines (i.e., each baseline independently from each other). Of course, $\left[\mathbf{k}_z(x,r)\right]_1 = 0$ and $\left[\boldsymbol{\delta}(x,r)\right]_1 = 0$.

Step 2

The second step consists in the compensation of the interferometric complex signal (2.21) from the phase-corrupted data to obtain:

$$\mathbf{y}_C(x,r) = \mathbf{y}_C(x,r) \odot \tilde{\mathbf{y}}_D^*(x,r) = \mathbf{y}_0(x,r) \odot \exp\left[-j\boldsymbol{\delta}(x,r) \right]. \tag{2.22}$$

Notice that, apart from the height shift, the observed MB signal (1.29) differs from the signal (2.22) only for the fact that the phases $\boldsymbol{\delta}(x,r)$ corrupt the useful error-free signal at a lower extent. Therefore, their estimation results in general to be simpler than the estimation of the original phase miscalibrations. Other advantages resulting from the compensation of the interferograms will be explained in subsection 2.3.1,as they depend on the specific algorithm used for estimating $\boldsymbol{\delta}(x,r)$.

Step 3

The third step consists in the estimation of the vector $\boldsymbol{\delta}(x,r)$ from $\mathbf{y}_C(x,r)$. In this work, a *minimum entropy* criterion is used (details are given in the next subsection 2.3.1) to maximize the contrast of the vertical profile extracted from $\mathbf{y}_C(x,r)$. Assuming that no estimation error is introduced, the following complex signal is obtained with the minimum entropy estimates of $\boldsymbol{\delta}(x,r)$:

$$\mathbf{y}_\delta(x,r) = \exp\left[j\boldsymbol{\delta}(x,r) \right]. \tag{2.23}$$

Step 4

The fourth step consists in the compensation of the estimated incoherent phases in (2.23) from $\tilde{\mathbf{y}}_D(x,r)$ to obtain:

$$\mathbf{y}_D(x,r) = \exp\left[j\mathbf{k}_z(x,r) z_0(x,r) \right] \odot \mathbf{e}(x,r). \tag{2.24}$$

Step 5

In the fifth and last block, exploiting the low variability of $\boldsymbol{\psi}(x,r)$ in the azimuth and range direction, an estimation of $z_0(x,r)$ and $\mathbf{e}(x,r)$ is obtained from the signal $\mathbf{y}_D(x,r)$.

It is worth to point out the primary role of Step 3 in the proposed processing chain. Indeed, after estimating the contribution of the incoherent phase variations $\boldsymbol{\delta}(x,r)$ from the signal $\mathbf{y}_C(x,r)$, they can be compensated from it in order to isolate the complex reflectivities for each acquisition. In this way, since the

phase errors $\mathbf{e}(x,r)$ have been already compensated in $\mathbf{y}_C(x,r)$ after Step 2, the retrieved reflectivities can be used to get already an estimate of the vertical profiles for tomographic applications, even if the height reference varies from cell to cell. It is expected that, since the data are not corrupted, the profiling can be performed even by means of an ABF spectral estimator, with the consequent improvement of height resolution and sidelobe rejection with respect to a classical BF. However, the contribution of the phase errors is still not known after Step 3, making Step 4 and Step 5 mandatory for different non-tomographic applications and to retrieve the correct height positioning of the scattering.

As already emphasized, the main advantage of the proposed calibration approach is the possibility to exploit the whole information contained in the MB stack without facing the problem of the spatial distribution of the calibration targets. In this way, the technique results to be independent from the features of the imaged area and the frequency band employed. Moreover, avoiding the detection step, the number of available acquisitions does not affect, at least in principle, the performance as no statistics are required to perform the calibration. As it will be shown in the performance analysis, the resulting phase calibration is effective also with a dual-baseline configuration, which is a very limit case in MB applications.

2.3.1 Entropy minimization

Consider a fixed range-azimuth resolution cell (x, r) and let $f(z)$ be the corresponding vertical profile. When the MB data stack is not affected by miscalibrations, the profile is supposed to exhibit a number of maxima located in correspondence of the heights of the most powerful height-resolved scatterers in the cell under test. In the ideal case in which a discrete distribution of M point-like scatterers is present in the scene, located at heights $(z_1,\dots z_N)$, the spectrum is filled with a number of M Dirac delta. In natural scenarios like forest stands, multiple close-by scattering echoes are received by the sensor array and the profile becomes a continuous signal which accounts for every contributions coming from a continuous set of heights. If residual miscalibrations corrupt the data the profile will look, in general, with a lower contrast, i.e. less *sharp* with inflated sidelobes and possibly height mislocations. As observed in [33], this behavior is more critical in cells where a volume scattering is present, since the effect of phase errors on the profile sharpness is more significant. Very importantly, the ABF profile result very sensitive to phase errors, as a consequence its sharpness loss turns out to be a good indicator of the presence of phase errors. From an algebraic point of view, an useful mean to get a measure of profile sharpness, hence an indication of the extent of residual miscalibration, is represented in information theory by the concept of *entropy*. In particular, the Renyi entropy [49]-[50] is a function of the estimated vertical profile $f(z)$ in the height interval of interest as follows:

$$S_r\left[f(z)\right]=\frac{1}{1-r}\ln\sum_{n=1}^{N}f^{2r}\left(z_n\right)-\frac{r}{1-r}\ln\sum_{n=1}^{N}f^{2}\left(z_n\right). \tag{2.25}$$

where z_n are the height at which the profile is sampled. When $r=2$, the Renyi entropy can be used to measure the sharpness of the vertical profile and (2.31) becomes:

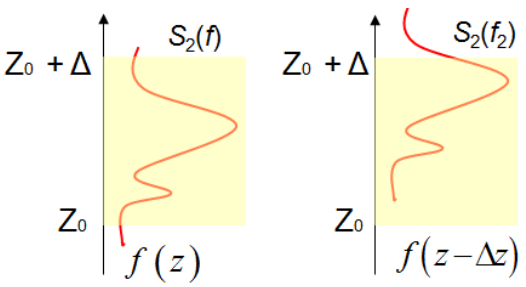

Figure 2.8 – Example of entropy measures employing a fixed height window. The same profile with a height shift can exhibit a lower entropy.

$$S_2\left[f(z)\right] = -\ln\sum_{n=1}^{N} f^4\left(z_n\right) + 2\ln\sum_{n=1}^{N} f^2\left(z_n\right). \tag{2.26}$$

In Chapter 3 a simulated analysis will be carried out to prove that in tomographic applications the Renyi entropy increases at the increase of the standard deviation of the phase errors affecting the data. It will also be shown that entropy minimization constitutes a reliable criterion to estimate the phase errors, thus retrieving the original profile sharpness.

It is worth noting that the entropy is measured inside a fixed height interval, and different positions of this interval with respect to same vertical profile lead to different entropy values. As a consequence, the entropy minimization algorithm could introduce a height shift while restoring the profile sharpness. This phenomenon is visualized in Fig. 2.8. On the left side, a profile $f\left(z\right)$ is depicted, while on the right side it is shown a height-shifted version of it, i.e. $f_2\left(z\right) = f\left(z - \Delta z\right)$. Recalling (2.26) that the entropy is a measure of the spectral content (i.e. the integral of the vertical profile), from Fig. 2.8 it is apparent that using the same height window for both spectra it results:

$$S_2\left[f_2\left(z\right)\right] < S_2\left[f_2(z)\right]. \tag{2.27}$$

In this case the same profile shifted in height exhibits a lower entropy, and it could be the result of the entropy minimization. However, this height shift can be neglected in the proposed calibration chain. In fact, after the entropy minimization and the compensation of the vector $\boldsymbol{\delta}\left(x,r\right)$ in Step 4, a possible height shift would add to the scattering centroid height. The resulting height reference is then retrieved in Step 5, when separating the height information from the original phase errors. This shed a new light on Step 2, making it of key importance: the compensation of the interferograms (*i*) reduce the calibration problem to a better conditioned one, (*ii*) allow to compensate for the height shifts introduced by the entropy minimization, and (*iii*) from an implementation point of view, makes easier the choice of a height interval of interest in which the scattering is supposed to be included. As a further comment, one could apply the entropy minimization directly to the original MB signal (1.29), but the correct height reference would be lost. The entropy minimization (or, equivalently, sharpness maximization) problem can be formalized as follows. It

corresponds to the problem of estimating a set of $K-1$ phase correction parameters[6] $\boldsymbol{\delta}=[\delta_1,\ldots,\delta_{K-1}]$ chosen in order to minimize the function (2.32) i.e.

$$\hat{\boldsymbol{\delta}}=\arg\min_{\boldsymbol{\delta}} S_2\left[f_{ABF}(z,\boldsymbol{\delta})\right] \tag{2.28}$$

with $\delta_k\in(-\pi,\pi]$. In the previous expression, $S_2\left[f_{ABF}(z,\boldsymbol{\delta})\right]$ is calculated by using $f_{ABF}(z,\boldsymbol{\delta})$, i.e. the ABF profile (given its sensitivity to phase errors) obtained from the covariance matrix $\hat{\mathbf{R}}_\delta$, defined as:

$$\hat{\mathbf{R}}_\delta=\hat{\mathbf{R}}_y\odot\left\{\exp\left[j\boldsymbol{\delta}(x,r)\right]\exp\left[j\boldsymbol{\delta}^H(x,r)\right]\right\}. \tag{2.29}$$

In any case, a closed-form solution of (2.28) does not exist, thus a numerical procedure must be adopted. When $K=3$, the optimization problem could also be implemented as an exhaustive search in a two dimensional space. Although computationally heavy, the exhaustive minimization leads to the global minimum of $S_2\left[f_{ABF}(z,\boldsymbol{\delta})\right]$. When $K>3$, the problem consists in a minimization of a non-linear, in general non-convex, $(K-1)$-dimensional functional, and an exhaustive search becomes unfeasible. The only possibility left is to resort to numerical iterative methods, with no guarantee of global optimization. As suggested in [50] and in many other multi-dimensional optimizations in applied signal processing, a possible way to tackle (2.28) is to decompose the hard problem in a sequence of easier problems. In this work, two procedures have been tested, and they are presented in the following.

A first minimization option is called Coordinate Descent (CD), and it constitutes a faster and easier alternative to the joint minimization of the entropy functional with respect to every parameters δ_k, e.g. like a gradient descent-based optimization. In a few words, a CD algorithm minimizes the entropy functional with respect to a single parameter at a time while holding the others fixed like an update process. Suppose to be at the generic step of the algorithm, that means to be at the i-th iteration and that the first $k-1$ phases have already been updated. As a consequence, the estimated phase vector at the present status is:

$$\hat{\boldsymbol{\delta}}^{(i,k-1)}=\left[\hat{\delta}_1^{(i)},\ldots,\hat{\delta}_{k-1}^{(i)},\hat{\delta}_k^{(i-1)},\hat{\delta}_{k+1}^{(i-1)},\ldots,\hat{\delta}_{K-1}^{(i-1)}\right]. \tag{2.30}$$

The next parameter to be updated is the k-th phase. Define:

$$\boldsymbol{\delta}^{(i,k)}=\left[\hat{\delta}_1^{(i)},\ldots,\hat{\delta}_{k-1}^{(i)},\delta_k^{(i)},\hat{\delta}_{k+1}^{(i-1)},\ldots,\hat{\delta}_{K-1}^{(i-1)}\right]. \tag{2.31}$$

In this way, $\delta_k^{(i)}$ is estimated by solving the following scalar minimization:

$$\hat{\delta}_k^{(i)}=\arg\min_{\alpha_k} S_2\left[f_{ABF}\left(z,\boldsymbol{\delta}^{(i,k)}\right)\right], \tag{2.32}$$

By repeating the minimization of (2.32) for $k=1,\ldots,K-1$, a sequence of scalar problem is obtained in lieu of the complex multidimensional problem of (2.28), and any of them can be solved exhaustively. Fig. 2.9 shows in a pictorial way the path from the initial values to the entropy minimum in a simple 3-image case. In Chapter 3, the results of a simulated performance analysis for this algorithm will be shown. Here, it is worth to point out that it constitutes a more feasible way to find a solution of (2.28) since its computational complexity is far below the one of exhaustive methods. Like all the iterative optimization methods, the final

[6] Dependence on (*x*,*r*) has been dropped for notation simplicity.

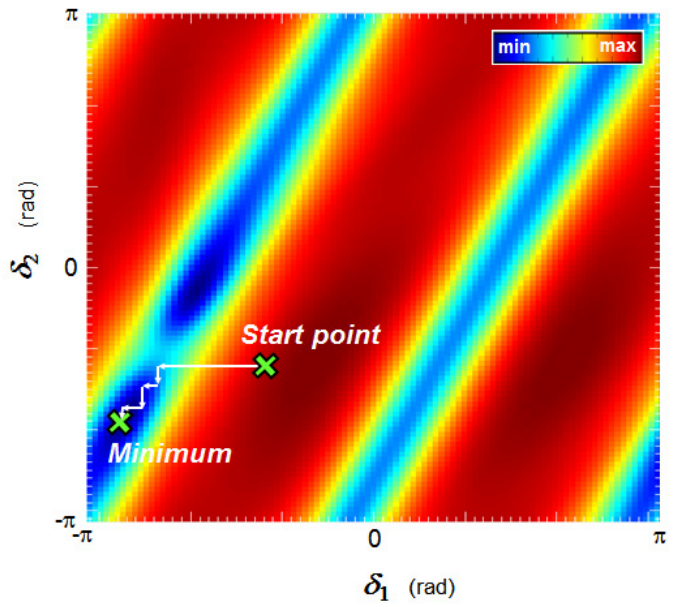

Figure 2.9 – Coordinate descent sequence superimposed to an entropy functional in the case *K*=3. The entropy functional has been calculated in a forested cell of the simulated data set (see Chapter 3).

performance will depend on the initialization values. In other words, the convergence to a global minimum of the functional $S_2\left[f_{ABF}(z,\boldsymbol{\delta})\right]$ is not guaranteed, unless a reliable initialization is found. Experiments have shown that a good starting point is the one with a set of K identical phases, whose value is chosen in order to minimize the entropy functional according to a one-dimensional exhaustive search.

A second implementation of the optimization (2.28) has been considered, and from here on it will be called Sequential Exhaustive algorithm (SE). For a better understanding, refer to Fig. 2.10 . The rationale of the SE procedure is based on the simple observation that the less critical scenario for the minimization is for $K=3$, where the most reliable solution can be found by simply employing an exhaustive search (still feasible in the 2-D case). Starting from the initialization vector $\boldsymbol{\delta}_{init}=\mathbf{0}$, let

$$\boldsymbol{\delta}^{(1)}=\left[\delta_1,\delta_2,0,\ldots,0\right] \tag{2.33}$$

be the parameter vector to be used for a first optimization of (2.33). A 2-dimensional exhaustive search is performed starting from $\boldsymbol{\alpha}_{init}$, which leads to:

$$\hat{\boldsymbol{\delta}}^{(1)}=\left[\hat{\delta}_1,\hat{\delta}_2,0,\ldots,0\right], \tag{2.34}$$

which represents the estimate of the compensation vector at the second iteration, and will be a fixed parameter for the following step. Thus, the free vector at the second iteration becomes:

$$\boldsymbol{\delta}^{(2)}=\left[\hat{\delta}_1,\hat{\delta}_2,\delta_3,\ldots,0\right]. \tag{2.35}$$

This time, a one-dimensional exhaustive search is sufficient to get

$$\hat{\boldsymbol{\delta}}^{(2)}=\left[\hat{\delta}_1,\hat{\delta}_2,\hat{\delta}_3,\ldots,0\right]. \tag{2.36}$$

Therefore, the procedure can be iterated until obtaining

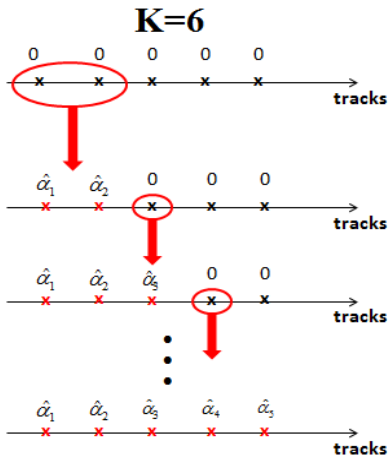

Figure 2.10 – Schematic view of the sequential exhaustive optimization procedure. Example with $K = 6$.

$$\hat{\boldsymbol{\delta}}^{(K-2)} = \left[\hat{\delta}_1, \hat{\delta}_2, \hat{\delta}_3, \ldots, \hat{\delta}_{K-1}\right], \tag{2.37}$$

which will be the final estimate of the compensation phases needed to minimize the entropy functional. In summary, the SE procedures needs K–3 one dimensional and one bi-dimensional optimization. The computational burden is lower than the one of a traditional exhaustive algorithm, but it is higher than the one of a CD.

Now, all the elements are available to compute the signal (2.23) and to compensate for the incoherent phase variations from $\tilde{\mathbf{y}}_D(x,r)$ in order to get $\mathbf{y}_D(x,r)$, from which the phase offset vector $\mathbf{e}(x,r)$ will be estimated.

2.3.2 Estimation of $\mathbf{e}(x,r)$

The estimation of the centroid height and of the original acquisition-dependent phase errors (Step 5 of the calibration chain) can be easily tackled by reasonably assuming that $\mathbf{e}(x,r)$ is slowly variable with x and r. Suppose that a reliable scatterer (e.g. a corner reflector) can be found in (x_0, r_0). As a consequence, one can compensate the phase error assuming this scatterer to be located at a known height (without losing generality, one can also suppose this scatterer to be located at null height), thus obtaining:

$$\mathbf{e}(x_0, r_0) = \mathbf{y}_D(x_0, r_0) \odot \exp\left[-j\mathbf{k}_z(x_0, r_0) z_0(x_0, r_0)\right]. \tag{2.38}$$

Given the hypothesis of slow range-azimuth variability of the phase errors, one can move one pixel further in range (or, equivalently, in azimuth), correct $\mathbf{y}_D(x_0, r_0+1)$ with $\mathbf{e}(x_0, r_0)$, and estimate $z_0(x_0, r_0+1)$. In general, $z_0(x,r)$ is estimated from the phase vector

$$\mathbf{s}(x,r) = \mathbf{y}_D(x,r) \odot \mathbf{e}^*(x, r-1) = \exp\left[j\mathbf{k}_z(x,r) z_0(x,r)\right] \odot \mathbf{e}(x,r) \odot \mathbf{e}^*(x, r-1). \tag{2.39}$$

By further manipulating the complex exponential, one obtains:

$$\begin{aligned}\mathbf{s}(x,r) &= \exp\left[j\mathbf{k}_z(x,r)z_0(x,r)\right]\odot\exp\left\{j4\pi\left[\mathbf{d}(x,r)-\mathbf{d}(x,r-1)\right]\right\} = \\ &= \exp\left[j\mathbf{k}_z(x,r)z_0(x,r)\right]\odot\exp\left[j4\pi\tilde{\mathbf{d}}(x,r)\right],\end{aligned} \tag{2.3}$$

having posed $\tilde{\mathbf{d}}(x,r)=\mathbf{d}(x,r)-\mathbf{d}(x,r-1)$. The goal of the remaining subsections is then to estimate $h_0(x,r)$ from $\mathbf{s}(x,r)$.

2.3.3 Statistical model of $\tilde{\mathbf{d}}(x,r)$

According to Section 1.6, it reasonable to assume $\mathbf{d}(x,r)\sim N\left(0,\sigma^2(x,r)\mathbf{I}\right)$; analogously, it will result $\mathbf{d}(x,r-1)\sim N\left(0,\sigma^2(x,r-1)\mathbf{I}\right)$. From the basic theory of Gaussian vectors, it turns out that:

$$\tilde{\mathbf{d}}(x,r)\sim N\left(\mathbf{0},\tilde{\mathbf{C}}(x,r)\right), \tag{2.41}$$

where $\tilde{\mathbf{C}}(x,r)$ is the covariance matrix to be determined in order to complete the stochastic characterization of $\tilde{\mathbf{d}}(x,r)$. By definition of covariance matrix:

$$\begin{aligned}\tilde{\mathbf{C}}(x,r) &= E\left\{\left[\mathbf{d}(x,r)-\mathbf{d}(x,r-1)\right]\left[\mathbf{d}(x,r)-\mathbf{d}(x,r-1)\right]^T\right\} = \\ &= \sigma^2(x,r)\mathbf{I}+\sigma^2(x,r-1)\mathbf{I}-2E\left\{\mathbf{d}(x,r)\mathbf{d}^T(x,r-1)\right\} = \\ &= \sigma^2(x,r)\mathbf{I}+\sigma^2(x,r-1)\mathbf{I}+\tilde{\mathbf{C}}'.\end{aligned} \tag{2.42}$$

Concerning the calculation of the elements of $\tilde{\mathbf{C}}'$, two cases must be distinguished:

- **diagonal terms**: in this case it results

$$\left[\tilde{\mathbf{C}}'\right]_{l,l} = -2E\left\{d_l(x,r)d_l(x,r-1)\right\}. \tag{2.43}$$

Given the starting hypothesis, it is reasonable to assume a correlation coefficient $\chi(r,r-1)$ among the two variables, turning out into:

$$\left[\tilde{\mathbf{C}}'\right]_{l,l} = -2\chi(r,r-1)\sigma(x,r)\sigma(x,r-1). \tag{2.44}$$

- **off-diagonal terms**: in this case it results

$$\left[\tilde{\mathbf{C}}'\right]_{l,m} = -2E\left\{d_l(x,r)d_m(x,r-1)\right\}. \tag{2.45}$$

Given the assumption of independence of the errors between different tracks, it results:

$$\left[\tilde{\mathbf{C}}'\right]_{l,m} = 0. \tag{2.46}$$

Finally, $\tilde{\mathbf{C}}(x,r)$ can be written as:

$$\tilde{\mathbf{C}}(x,r)=\left[\sigma^2(x,r)+\sigma^2(x,r-1)-2\chi(r,r-1)\sigma(x,r)\sigma(x,r-1)\right]\mathbf{I}. \tag{2.47}$$

It is reasonable to assume further that $\sigma^2(x,r)=\sigma^2(x,r-1)$, and dropping the dependence on (x,r) for the sake of notation simplicity:

$$\tilde{\mathbf{C}} = 2\sigma^2(1-\chi)\mathbf{I}. \tag{2.48}$$

The expression of $\tilde{\mathbf{C}}$ in (2.48) states that the higher the correlation χ between adjacent pixels, the lower the resulting error standard deviation, tending to 0 with $\chi = 1$, as it is reasonable to expect.

2.3.4 Estimation of z_0

According to the previous Subsection, z_0 must be estimated from:

$$\mathbf{s} = \exp\left(j\mathbf{k}_z h_0\right) \odot \exp\left(j4\pi\tilde{\mathbf{d}}\right). \tag{2.49}$$

where $\tilde{\mathbf{d}} \sim N\left(\mathbf{0}, \tilde{\mathbf{C}}\right)$, with $\tilde{\mathbf{C}} = 2\sigma^2\left(1-\chi\right)\mathbf{I} = \tilde{\sigma}^2\mathbf{I}$.

It is worth noting that the problem of estimating z_0 from the signal (2.49) is rather atypical. Nevertheless, it can be considered as a single-look deterministic signal backscattered from the height z_0, corrupted by a residual phase error and in the asymptotic case for signal-to-noise ratio tending to infinite. In absence of phase miscalibration, it is well-known that for such a signal the maximum likelihood estimator of z_0 is given by the height corresponding to the highest peak of the Fourier transform of the data (i.e. the BF spectral estimate). The estimation performance obtainable with this estimator will be analyzed in the next Chapter.

2.3.5 Relationship between the proposed calibration methods and the array calibration theory

As previously affirmed, the proposed phase calibration method can be placed in the theoretical framework of (interferometric) array self-calibration. With reference to the theoretical calibration limits analyzed in Section 2.1, in the MB SAR framework the nominal interferometric array shape is linear and only the position of the master track can be assumed known (case 2 examined by Rockah and Schultheiss in [37]). This ensures the calibration to be limited by a residual height shift due to an array rotational ambiguity. However, since the phase offsets can be reasonably assumed slowly variable in range and azimuth, it is possible to compensate for the offset in each pixel by using the phase error estimated from the previous one, in order to reduce the problem to a "small variance" one and to compensate for as much as possible the residual height shifts. As a final remark, even in the "small variance" problem a global height shift of the scattering can appear, depending on whether the height of the reference pixel is known or not. However, this height shift is constant on the whole image, hence it is not of concern in the applications (as usually happens in SAR interferometry).

- This page intentionally left blank -

CHAPTER 3

PERFORMANCE ANALYSIS WITH SIMULATED DATA

3.1 The simulated data set

The proposed processing chain has been tested in controlled conditions by using a simulated dataset. In particular, a MB stack has been generated with the PolSARProSim software[1] [51]. PolSARProSim makes use of a detailed (but limited) physical description of the scene, including in addition to geometry such quantitites as surface roughness and the frequency-dependent dielectic behavior of the materials. Theoretical attenuation and scattering models for each element of the artificial 3-D scene are combined with a model for coherent SAR imaging. Images simulated in this way display properties consistent with those observed in real SAR imagery, with high level of realism. Although many unavoidable approximations are used in the

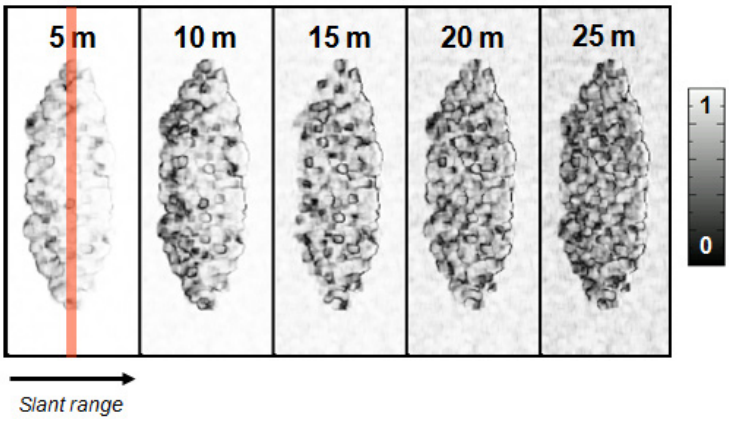

Figure. 3.1 – Interferometric coherence with respect to the master acquisition for the first 5 baselines. The red line indicates the range coordinate selected for the tomographic analysis.

[1] The PolSARProSim software is freely available in the educational software PolSARPro distributed by ESA under the GNU licence.

generation of the electromagnetic scattering, the calibration performance obtained over this data set can be considered reliable, both qualitatively and quantitatively.

The acquisition parameters have been set according to the typical values of the DLR E-SAR platform, with an incidence angle of 30deg and a central frequency of 1.3GHz (L-Band). The complete stack consists of 10 images, with an overall horizontal baseline length of 45m and a minimum distance between the tracks (sampling distance) equal to 5m. The simulated area is a forest site with deciduous and broadleaves tree species, with a mean tree height of 20m. The area has been simulated in absence of topography, and the ground height is 0m over the whole scene. In Fig. 3.1 the interferometric coherences are shown with respect to the master acquisition for the first 5 baselines. As expected, the coherence reduces at the increase of the baseline, and this happens at a higher extent where volumetric scattering is present. A tomographic analysis of these data has been performed by selecting the range coordinate at mid-range (see red line in Fig. 3.1), thus obtaining the tomograms in the height-azimuth plane.

3.2 Performance analysis

In this Section the results of a simulated performance analysis of the whole proposed calibration chain will be shown. As already deeply discussed in Chapter 2, this chain consists of two main blocks: the first one minimizes the incoherent phase variations arising after the compensation of the complex InSAR phase from the multi-baseline data set; the second one retrieves the original phase errors in the MB stack. These blocks will be analyzed individually, in order to quantify their performance. Then, the calibration results will be shown in Section 3.2.3, where the whole chain will be applied to PolSARProSim data.

3.2.1 Entropy minimization

First of all, a simulated analysis has been carried out to prove in an empirical way that the minimization of the Renyi entropy is a good criterion to reduce the phase miscalibrations which corrupt the data. In particular, the purpose of this initial set of simulation has been to prove that the Renyi entropy of the ABF vertical profile increases monotonously at the increase of the standard deviation of the phase errors. If so, the minimization of the entropy of the ABF profile (i.e. the maximization of its sharpness) leads to the desired error-free profile.

It is worth to point out that the simulated miscalibration phase vector according to the Gaussian model could contain a component linear with $\mathbf{k}_z(x,r)$, causing a mere height shift of the profile. Since the objective of this simulations is to measure the sharpness loss only, without loss of generality, this linear contribution has been estimated in a least squares sense and compensated from the corrupted data. Notice that this initial analysis is valid in each point of the calibration chain. For this reason, phase errors will be measured generically in radians. More specific interpretations will be proposed in the course of the analysis.

After their generation, PolSARProSim MB data have been corrupted using a $(K-1)$-dimensional vector $\boldsymbol{\alpha}$ with random Gaussian phase noise independent from baseline to baseline, with zero mean and with standard deviation expressed in radians $\sigma_\alpha \in \{0.08\pi, 0.16\pi, 0.32\pi, 0.4\pi, 0.6\pi\}$. A realization of this pahse

noise has been generated for each pixel at constant range under analysis. The number of realizations has been set to $N_{trial}=1000$ realizations, which is a good compromise between the reliability of the measures extracted from the simulation and the feasibility in acceptable times. For each error realization, the following $K\times K$ covariance matrix has been built:

$$\hat{\mathbf{R}}_{corrupted}(x,r)=\hat{\mathbf{R}}_{y}(x,r)\odot\exp\left\{j\boldsymbol{\alpha}(x,r)\boldsymbol{\alpha}^{H}(x,r)\right\}. \tag{3.1}$$

Where not otherwise stated, the covariance matrices have been estimated by averaging a 5×5 range-azimuth window. Starting from $\hat{\mathbf{R}}_{corrupted}(x,r)$, the ABF profile have been calculated and the corresponding entropy values have been measured for each pixel of the data stack in the selected line at constant range. As already discussed, the entropy measure depends on the employed height window and an inappropriate interval would lead to unreliable estimates. For this first analysis, the height interval $[-10\text{m},40\text{m}]$ has been considered because it contains the whole scattering contributions coming from ground, tree trunks and canopy (volume scattering). The entropy measures have been collected for each realization and for each azimuth coordinate, and their statistics have been calculated. In particular, for each pixel the minimum, the mean, and the maximum of the obtained entropy values have been measured and their histogram has been derived for a better visualization and understanding of their distribution along the image, i.e. depending of the imaged scatterers.

At first, the full uniform baseline distribution with 10 SAR images has been processed. In Fig. 3.2 the ABF tomogram in the height-azimuth plane corresponding to the error-free data set at the selected range line is shown obtained with HH polarization. In the bare soil area, the main scattering contribution is located at zero height (i.e. at the ground height), whereas in the forested area the volume scattering plays the most significant role, with a maximum height of 20m. In some cells it is also possible to distinguish multiple different contributions in height, e.g. one coming from the ground and some from the canopy. In Fig. 3.3 the ABF tomogram corrupted by a simulated phase error with $\sigma_{\alpha}=0.08\pi$ is reported averaged over N_{trial} trials. With such an error standard deviation, the discrimination is still possible between the bare and the

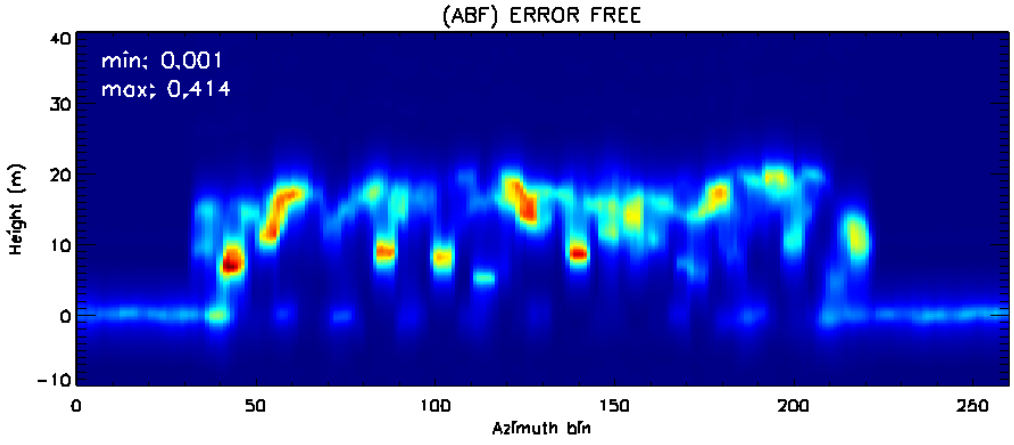

Figure 3.2 – ABF tomogram in the azimuth-height plane for the range line under test in absence of phase errors, uniform full baseline configuration (K = 10). Top left :minimum and maximum spectral amplitudes.

forested areas. It is possible to recognize inflated sidelobes both in the bare soil area and in the forested one. Moreover, it is worth noting a strong decrease of the maximum value in the corrupted tomogram with respect to the error-free one, from 0.414 to 0.101. This is due to the previously discussed self-cancellation effect of the ABF filter which tends to reject the most powerful spatial harmonics as they are seen as interferences, and to enhance the spurious sidelobe contributions. In Fig. 3.4, the histograms of the measured entropies over the error realizations still with $\sigma_\alpha = 0.08\pi$ are shown at the variation of the azimuth coordinate. The minimum and the maximum measured entropies have been superimposed with red lines, while a black line denotes the entropy of the profiles in absence of error. It is apparent that this curve is always lower than or equal to the minimum measured entropy of the phase-corrupted spectrum. Furthermore, the mean entropy is higher in the central part of the tomographic slice, which corresponds to the canopy area, in comparison with the bare soil area whose entropy values never reach 4. This happens because the degradation effect of errors in the canopy area is stronger due to the volume scattering, thus reducing the profile sharpness at a higher extent, as shown by the histograms. This is a confirmation of the theoretical trends derived in [33]. For a better visualization, in Fig. 3.5 the error-free, the measured minimum/maximum and the average entropies are plotted as a function of azimuth in the same panel. It is apparent that the entropy of the error-free profile constitutes a lower bound for the ones corresponding to the miscalibrated data, and that the minimum measured entropy is very close to it. Nevertheless, an unexpected very small difference exists between the error-free and the minimum measured entropy plots. It has been verified that this is an effect of the limited number of realizations, i.e. a "finite sample effect". In fact, the probability of having an error realization of 10-element vector of independent random variables very close to 0 is very small. In this sense, a measured minimum entropy totally superimposing to the error-free one could be found simply by increasing the number of realization.

This analysis has been repeated by gradually increasing the standard deviation σ_α while holding the baseline configuration fixed. Figs. 3.6-3.17 show the averaged corrupted spectra, the histograms and the entropy comparisons for values of σ_α belonging to $\{0.16\pi, 0.32\pi, 0.4\pi, 0.6\pi\}$. From these plots, the results of an increasing phase error are more apparent, with higher sidelobes and with a stronger self-cancellation effect resulting in an overall decrease of the 95.4% of the maximum peak amplitude which reaches 0.019 with the maximum considered σ_α. Noteworthy, the relative radiometry among the peaks of the same profile is totally mislead, again as a consequence of the self-cancellation effect. From the comparison of the histograms and the entropy statistics, the trends already underlined before become more apparent, with the mean entropy values moving away from the error free case; the higher is σ_α, the higher is the distance between the red and the black line. Nevertheless, the green line corresponding to the minimum entropy is still close to the one corresponding to the error-free case. Notice that the finite sample effect get worse at the increase of σ_α, as a higher and higher number of realization is needed to generate a small phase error. To conclude this analysis, in Fig. 3.18 the mean entropy values are plotted for different phase error standard deviations σ_α. From this figure, it is apparent that the entropy of an ABF spectrum monotonically increases with the increase of σ_α.

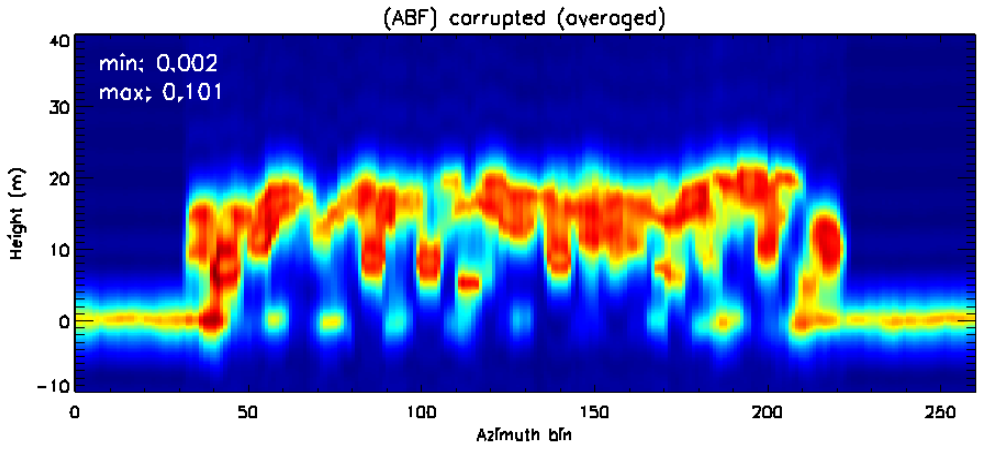

Figure 3.3 – ABF tomogram in the azimuth-height plane for the range line under test averaged over 1000 realization of the miscalibration error vector (σ_α = 0.08π), uniform full baseline configuration (K = 10). Top left: minimum and maximum spectral amplitudes.

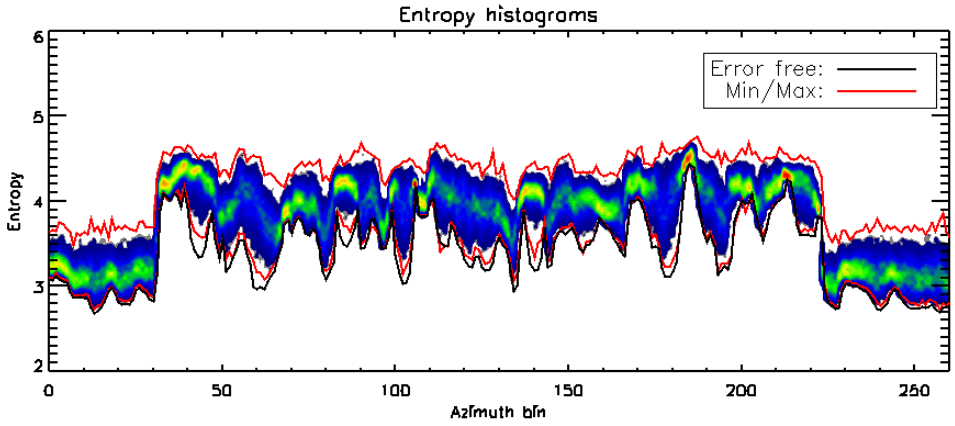

Figure 3.4 – Entropy histograms calculated over 1000 realization of the miscalibration error vector (σ_α = 0.08π), uniform full baseline configuration (K = 10). Black line: entropy corresponding to the error-free data set. Red lines: measured minimum and maximum entropies corresponding to the corrupted data set.

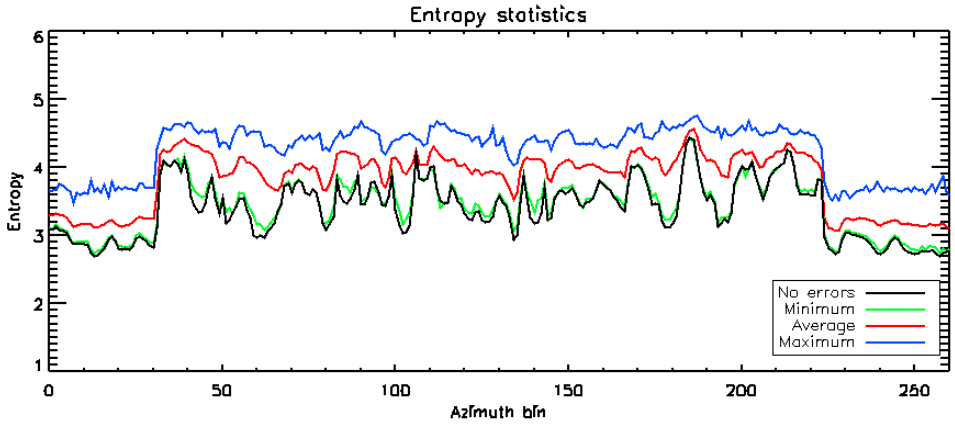

Figure 3.5 – Entropy statistics calculated over 1000 realization of the miscalibration error vector (σ_α = 0.08π), uniform full baseline configuration (K = 10). Black line: entropy corresponding to the error-free data set.

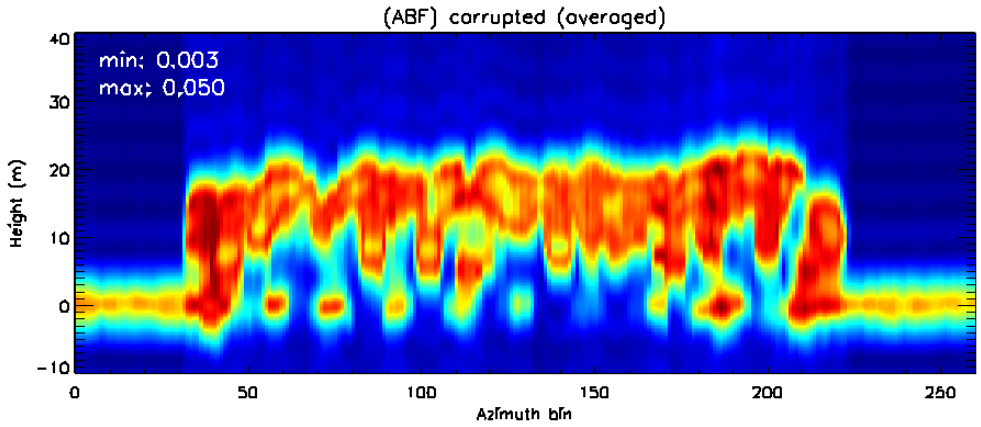

Figure 3.6 – ABF tomogram in the azimuth-height plane for the range line under test averaged over 1000 realization of the miscalibration error vector ($\sigma_\alpha = 0.16\pi$), uniform full baseline configuration ($K = 10$). Top left: minimum and maximum spectral amplitudes.

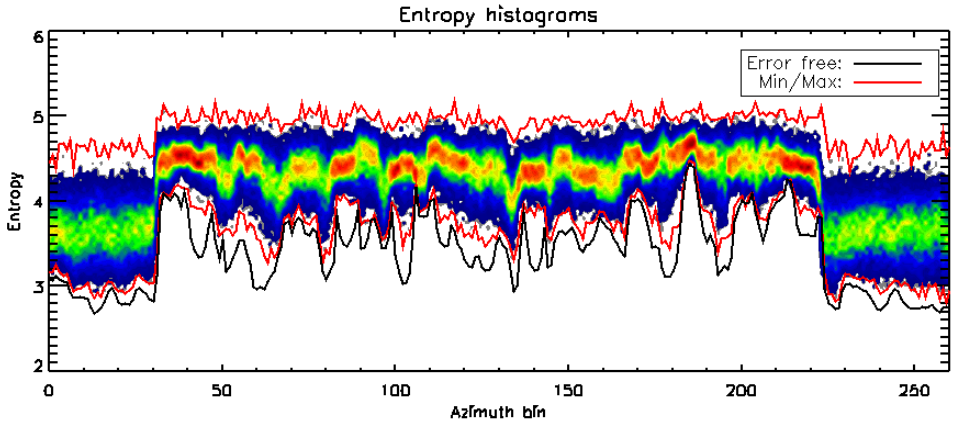

Figure 3.7 – Entropy histograms calculated over 1000 realization of the miscalibration error vector ($\sigma_\alpha = 0.16\pi$), uniform full baseline configuration ($K = 10$). Black line: entropy corresponding to the error-free data set. Red lines: measured minimum and maximum entropies corresponding to the corrupted data set.

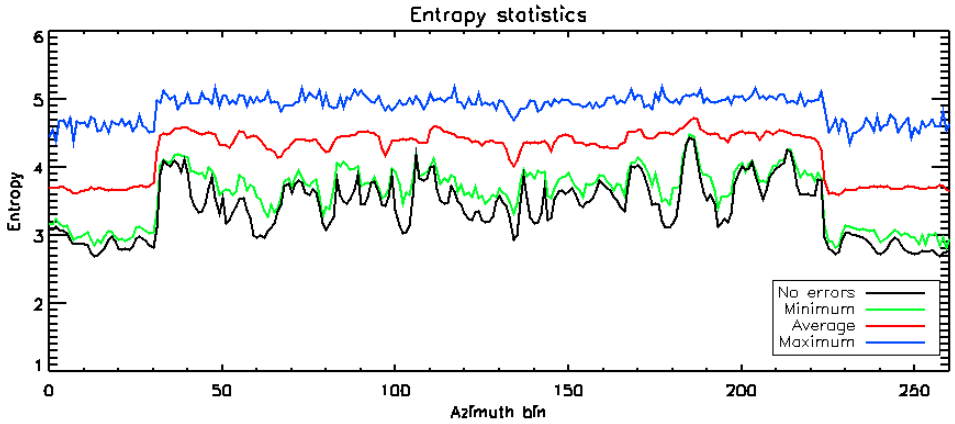

Figure 3.8 – Entropy statistics calculated over 1000 realization of the miscalibration error vector ($\sigma_\alpha = 0.16\pi$), uniform full baseline configuration ($K = 10$). Black line: entropy corresponding to the error-free data set.

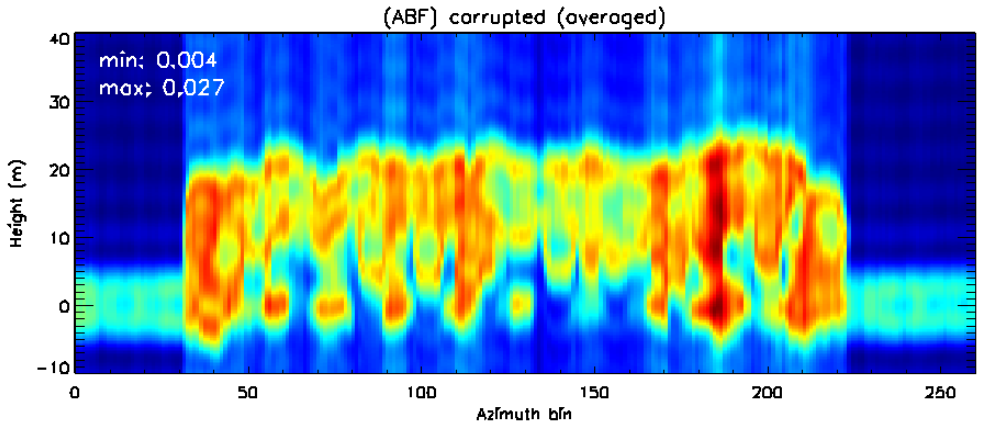

Figure 3.9 – ABF tomogram in the azimuth-height plane for the range line under test averaged over 1000 realization of the miscalibration error vector ($\sigma_\alpha = 0.32\pi$), uniform full baseline configuration ($K = 10$). Top left: minimum and maximum spectral amplitudes.

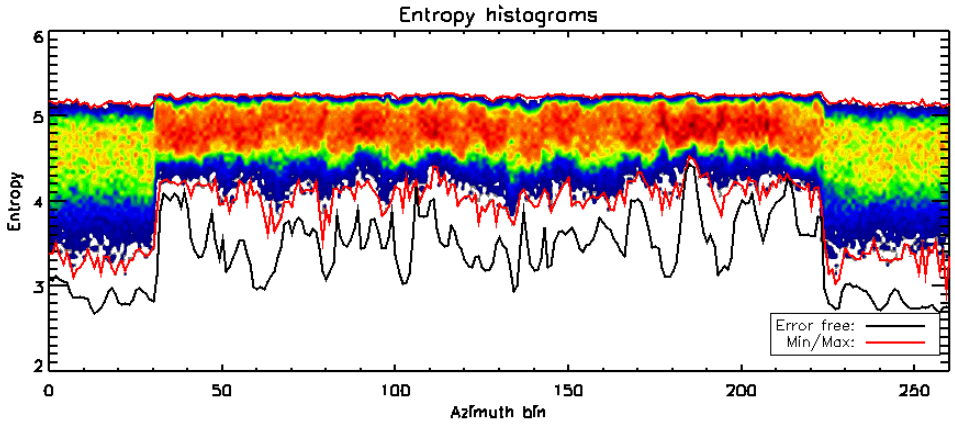

Figure 3.10 – Entropy histograms calculated over 1000 realization of the miscalibration error vector ($\sigma_\alpha = 0.32\pi$), uniform full baseline configuration ($K = 10$). Black line: entropy corresponding to the error-free data set. Red lines: measured minimum and maximum entropies corresponding to the corrupted data set.

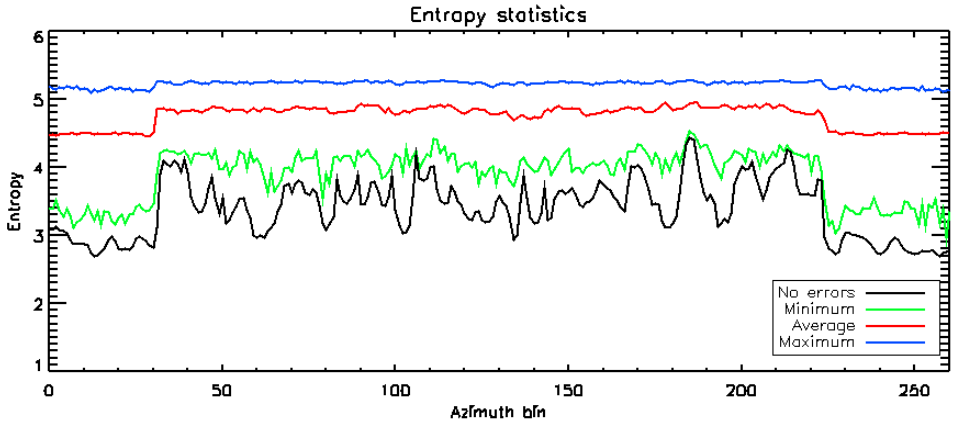

Figure 3.11 – Entropy statistics calculated over 1000 realization of the miscalibration error vector ($\sigma_\alpha = 0.32\pi$), uniform full baseline configuration ($K = 10$). Black line: entropy corresponding to the error-free data set.

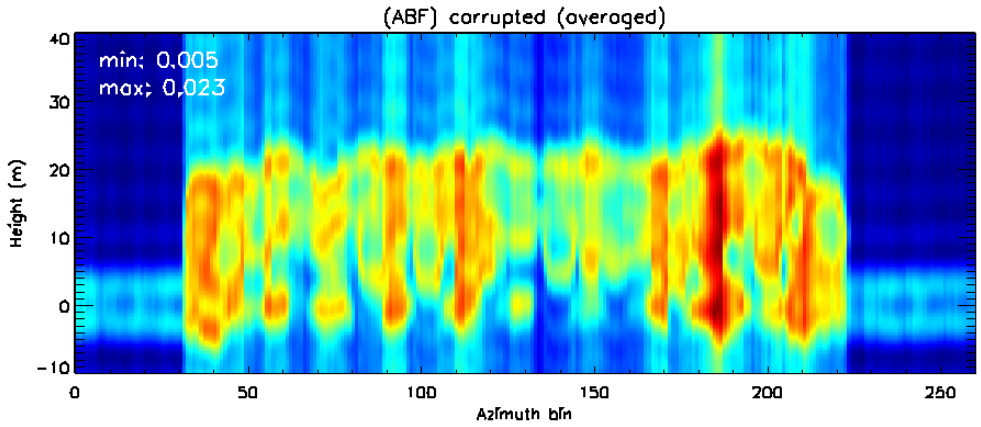

Figure 3.12 – ABF tomogram in the azimuth-height plane for the range line under test averaged over 1000 realization of the miscalibration error vector ($\sigma_\alpha = 0.4\pi$), uniform full baseline configuration ($K = 10$). Top left: minimum and maximum spectral amplitudes.

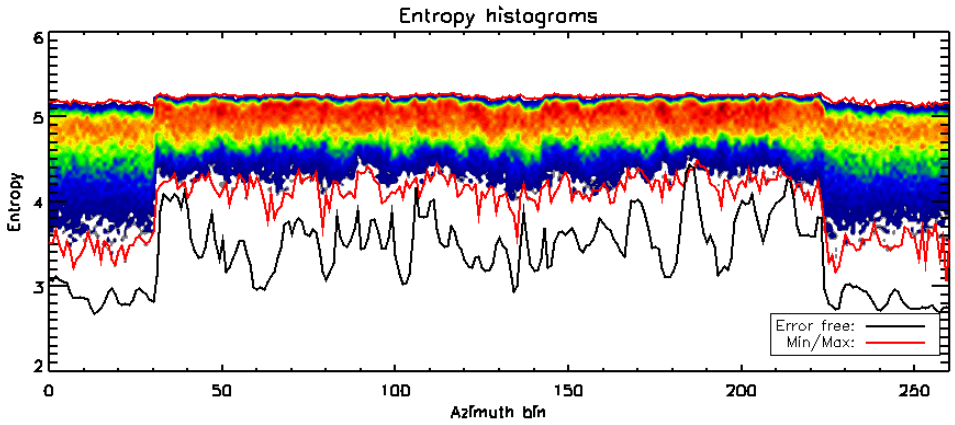

Figure 3.13 – Entropy histograms calculated over 1000 realization of the miscalibration error vector ($\sigma_\alpha = 0.4\pi$), uniform full baseline configuration ($K = 10$). Black line: entropy corresponding to the error-free data set. Red lines: measured minimum and maximum entropies corresponding to the corrupted data set.

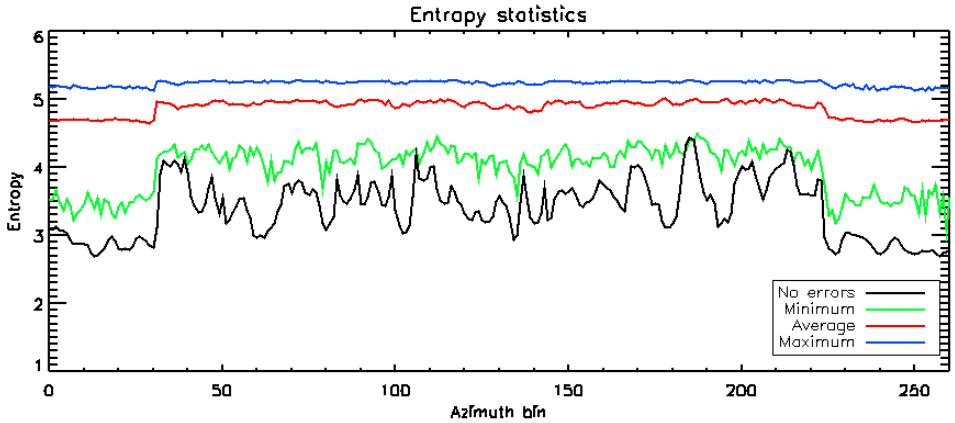

Figure 3.14 – Entropy statistics calculated over 1000 realization of the miscalibration error vector ($\sigma_\alpha = 0.4\pi$), uniform full baseline configuration ($K = 10$). Black line: entropy corresponding to the error-free data set.

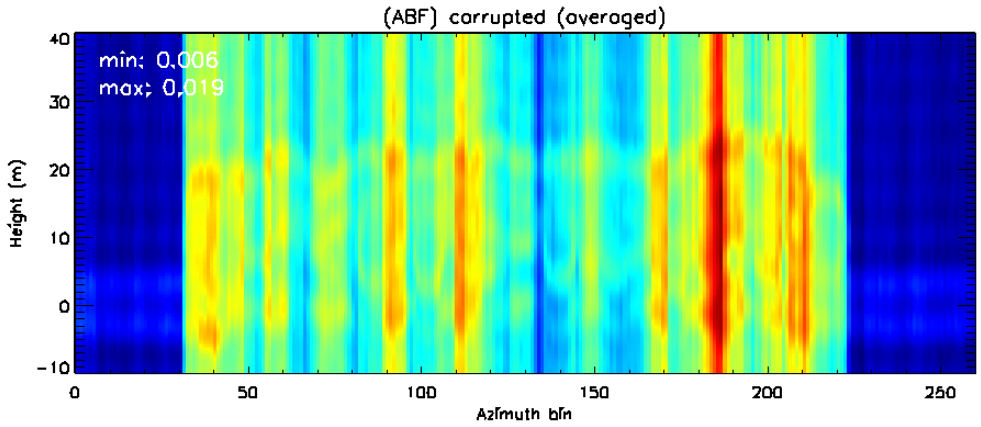

Figure 3.15 – ABF tomogram in the azimuth-height plane for the range line under test averaged over 1000 realization of the miscalibration error vector ($\sigma_\alpha = 0.6\pi$), uniform full baseline configuration ($K = 10$). Top left: minimum and maximum spectral amplitudes.

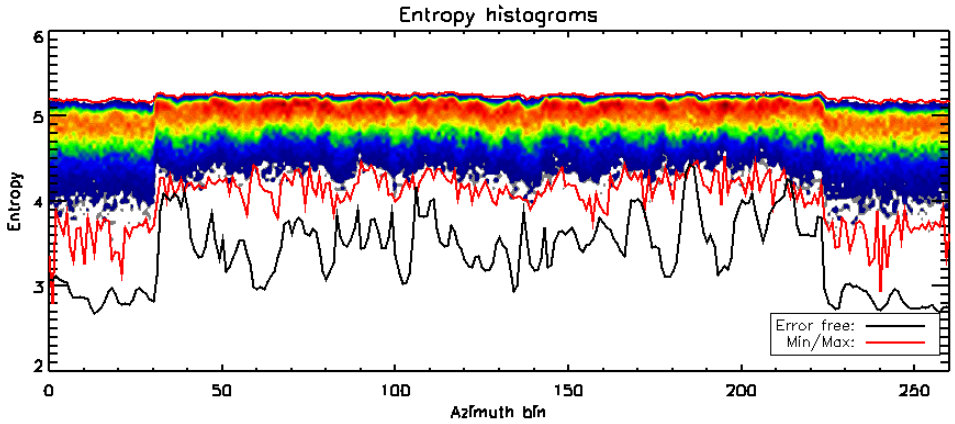

Figure 3.16 – Entropy histograms calculated over 1000 realization of the miscalibration error vector ($\sigma_\alpha = 0.6\pi$), uniform full baseline configuration ($K = 10$). Black line: entropy corresponding to the error-free data set. Red lines: measured minimum and maximum entropies corresponding to the corrupted data set.

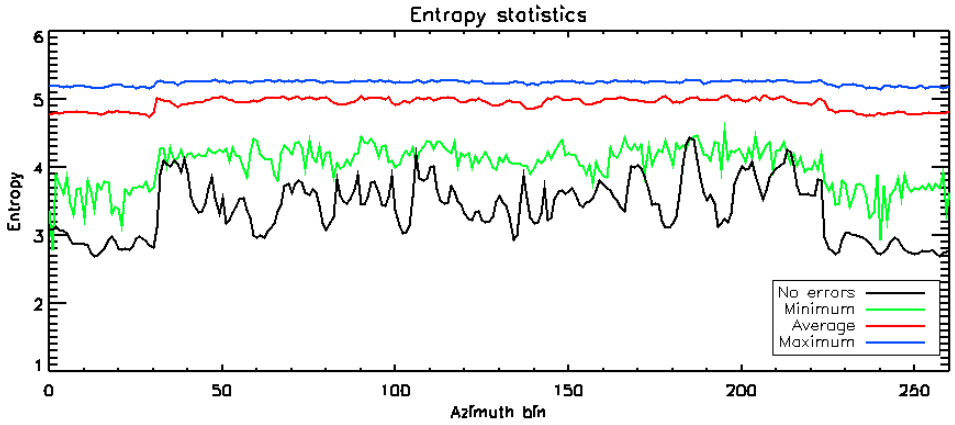

Figure 3.17 – Entropy statistics calculated over 1000 realization of the miscalibration error vector ($\sigma_\alpha = 0.6\pi$), uniform full baseline configuration ($K = 10$). Black line: entropy corresponding to the error-free data set.

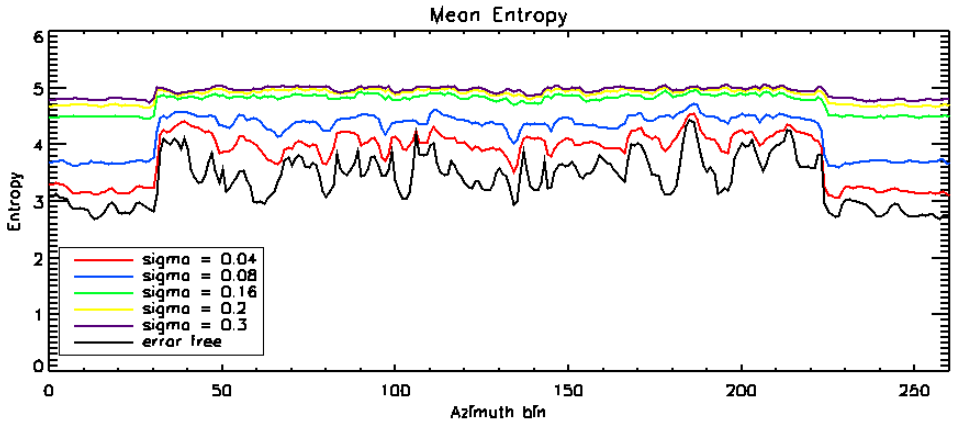

Figure 3.18 – Average entropies calculated over 1000 realizations of the miscalibration error vector, as a function of the azimuth coordinate and for different values of σ_α, uniform full baseline configuration (K = 10). Black line: entropy corresponding to the error-free data set.

The next issue to be addressed is to verify if the entropy of the vertical profiles increases at the increase of the standard deviation of the error vector in the case in which a lower number of baselines are available, still in uniform baseline configurations. For this reason, the same experiment has been repeated with $K = 4$, $B = \{0\text{m}, 5\text{m}, 10\text{m}, 15\text{m}\}$, and $K = 5$, $B = \{0\text{m}, 5\text{m}, 10\text{m}, 15\text{m}, 20\text{m}\}$. Notice that in the considered cases the height resolution of the MB acquisition is lower than the full baseline case, leading to profiles with a lower sharpness (i.e. a higher entropy) even in an error-free case. The simulated analysis (not reported here for the sake of conciseness) has shown again that the entropy increases at the increase of σ_α.

As a final experiment, it is worth to investigate the role of the non-uniformity of the baseline distribution. As a consequence, this simulated analysis has been repeated by fixing the error standard deviation to $\sigma_\alpha = 0.08\pi$ and by changing the baseline configuration, with the only requirement that it is not uniform. Here, results are reported for two baseline configurations of particular interest. In the first one, $B = \{0\text{m}, 5\text{m}, 10\text{m}, 15\text{m}, 25\text{m}\}$ and it resembles the nominal baseline configuration of the MB data set acquired during the DLR airborne TempoSAR 2008 campaign that will be processed in Chapter 4. Actually, this baseline set is common to other different airborne campaigns, thus the obtained results are representative for other different data sets. Of course, the scattering could change from scenario to scenario, however, the simulated data set contains many different profiles which could also be in common. The second considered baseline configuration is composed by three image only with $B = \{0\text{m}, 5\text{m}, 15\text{m}\}$. These numbers have been chosen to limit as much as possible the baseline sampling employing a rather high degree of non-uniformity (the smallest baseline is 1/3 of the total baseline). Figs. 3.19 and 3.20 show the error-free ABF tomograms obtained in the 5-image case and in the 3 image case, respectively. Due to a reduction of total baseline, the height resolution results to be worse than the height resolution of the tomogram in Fig. 3.2. Moreover, sidelobes are more visible due to the non-uniform baseline sampling, although if the adaptivity of the ABF filtering is able to reject them even with a very poor dual baseline sampling. Notice that also the profile themselves and the profile peak amplitudes change from case to case. This is due in part to the fact that no

normalization with respect to K is employed in the calculation of the ABF filter (see [32]), and in part to radiometric biases characterizing the ABF spectral estimate itself. However, a thorough discussion on this topic is beyond the purpose of the entire work. In Figs. 3.21-3.23 the corrupted tomogram, the entropy histograms and the entropy statistics are shown for the 5-image baseline configuration, while the same quantities are shown in Figs. 3.24-3.26 for the 3-image configuration. In both cases, it is possible to affirm that the profile entropy increases with the presence of miscalibration errors. The amount of this increase depends on the number of images, being higher with higher K. Notice that differently from before in this study case the minimum measured entropy is superposed to the error-free one. This means that 1000 realization are enough here to characterize statistically the entropy functional. In fact, it can be easily seen that with a lower number of independent Gaussian samples the probability to have a realization of the error vector in a very small interval around the vector filled with 0s increases with respect to the case with $K = 10$. Notice also that in some points the minimum measured entropy is lower than the error-free one, even if of a negligible quantity. This is particularly apparent for the case $K = 3$. This phenomenon can be explained to be due to small inaccuracies in the estimation of the linear component of the generated error vector, which results into a height shift that in turn could reduce the profile entropy, as seen in Fig. 2.8. The lower is K, the (relatively) higher the inaccuracy.

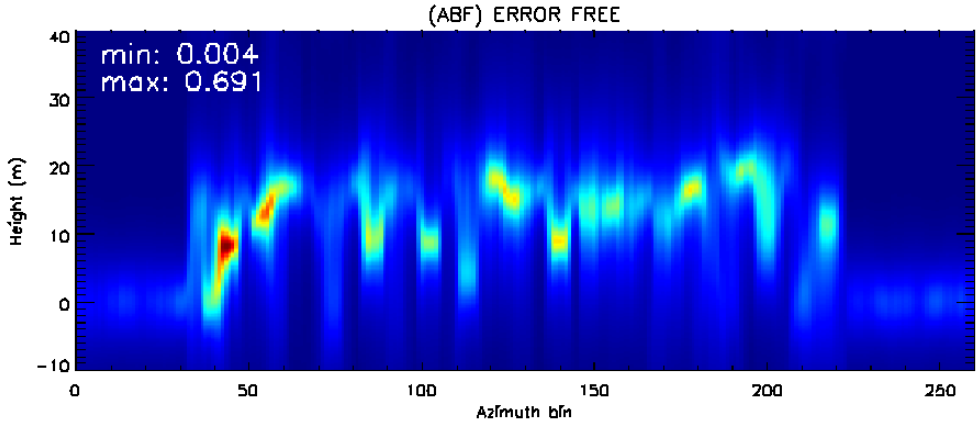

Figure 3.19 – ABF tomogram in the azimuth-height plane for the range line under test in absence of phase errors, baseline configuration B={0m, 5m, 10m, 15m, 25m}. Top left: minimum and maximum spectral amplitudes.

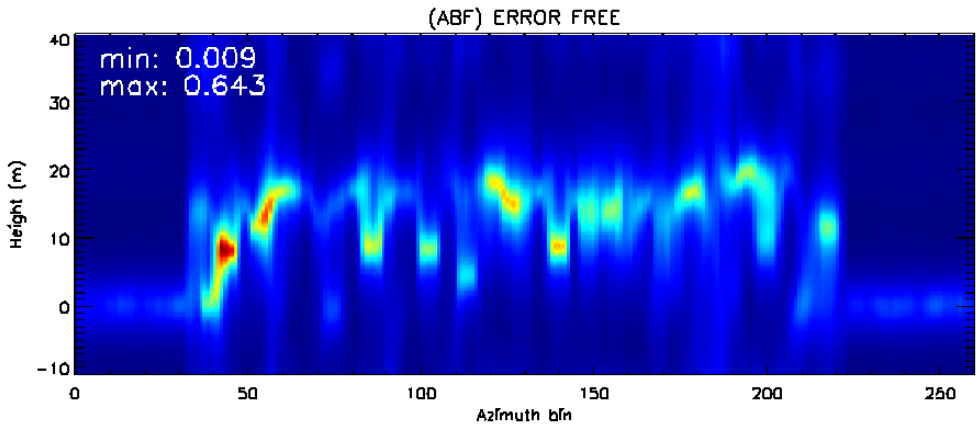

Figure 3.20 – ABF tomogram in the azimuth-height plane for the range line under test in absence of phase errors, baseline configuration B={0m, 5m, 15m}. Top left :minimum and maximum spectral amplitudes.

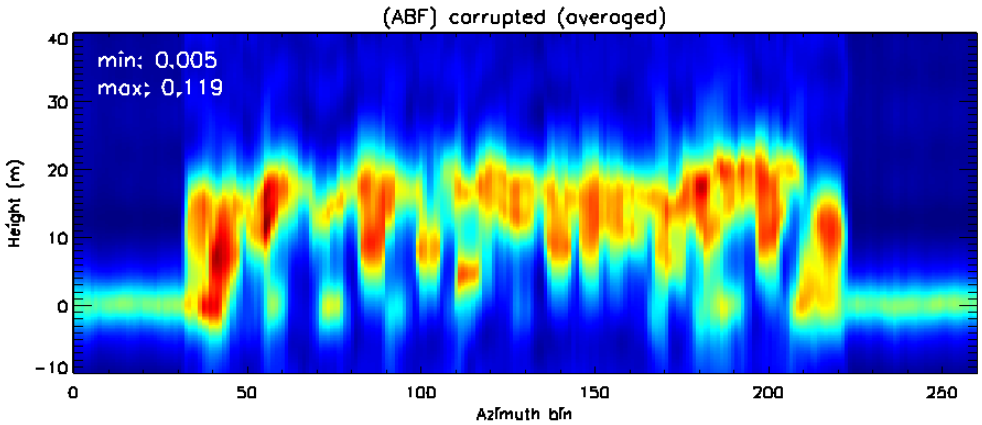

Figure 3.21 – ABF tomogram in the azimuth-height plane for the range line under test averaged over 1000 realization of the miscalibration error vector (σ_α = 0.08π), baseline configuration B={0m, 5m, 10m, 15m, 25m}. Top left: minimum and maximum spectral amplitudes.

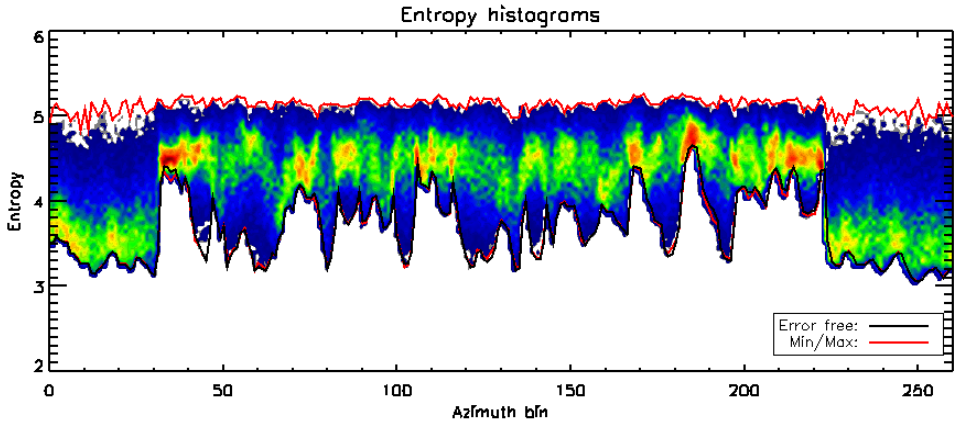

Figure 3.22 – Entropy histograms calculated over 1000 realization of the miscalibration error vector (σ_α = 0.08π), baseline configuration B={0m, 5m, 10m, 15m, 25m}. Black line: entropy corresponding to the error-free data set. Red lines: measured minimum and maximum entropies corresponding to the corrupted data set.

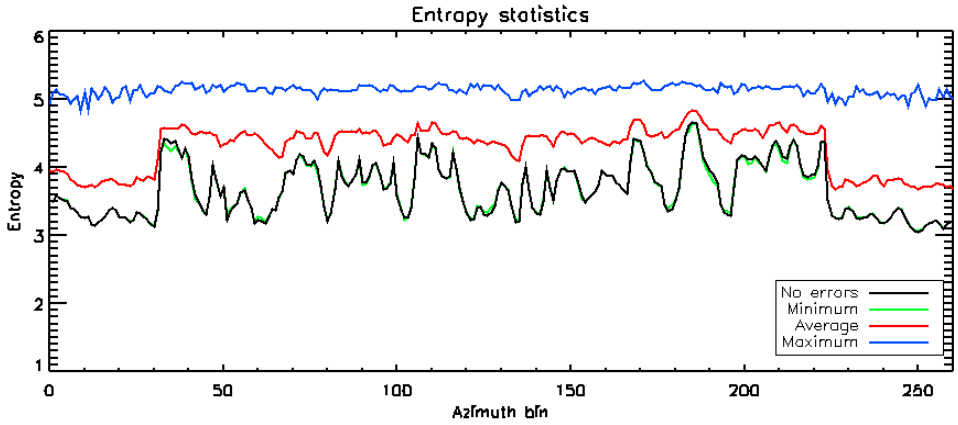

Figure 3.23 – Entropy statistics calculated over 1000 realization of the miscalibration error vector (σ_α = 0.08π), baseline configuration B={0m, 5m, 10m, 15m, 25m}. Black line: entropy corresponding to the error-free data set

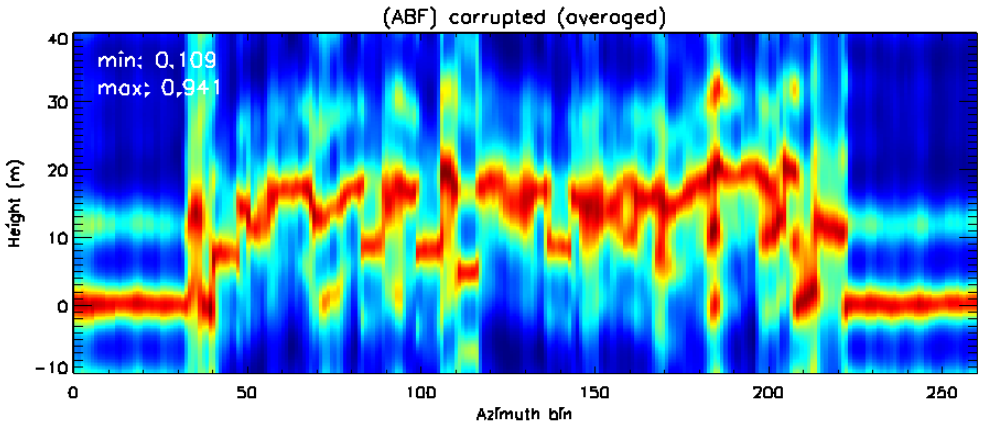

Figure 3.24 – ABF tomogram in the azimuth-height plane for the range line under test averaged over 1000 realization of the miscalibration error vector (σ_α = 0.08π), baseline configuration B={0m, 5m, 15m}. Top left: minimum and maximum spectral amplitudes.

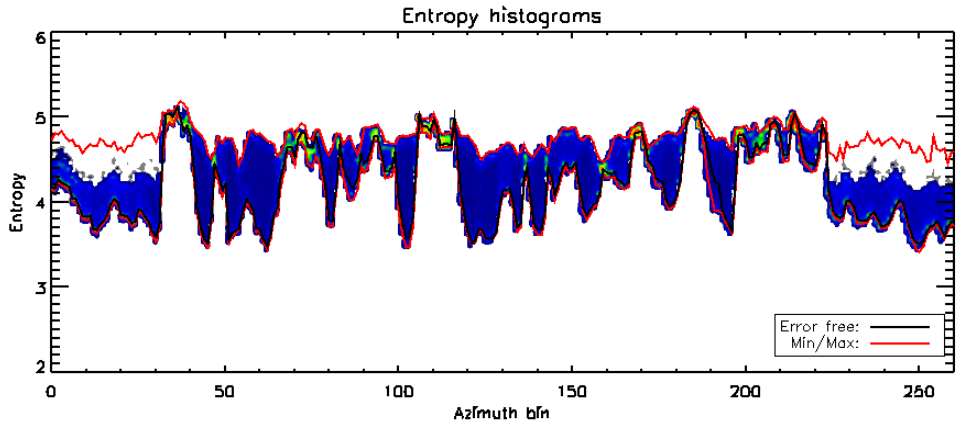

Figure 3.25 – Entropy histograms calculated over 1000 realization of the miscalibration error vector (σ_α = 0.08π), baseline configuration B={0m, 5m, 15m}. Black line: entropy corresponding to the error-free data set. Red lines: measured minimum and maximum entropies corresponding to the corrupted data set.

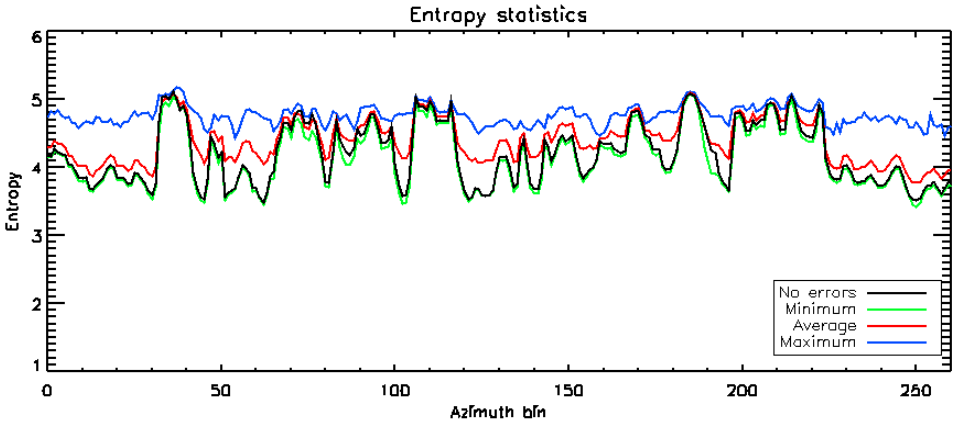

Figure 3.26 – Entropy statistics calculated over 1000 realization of the miscalibration error vector (σ_α = 0.08π), baseline configuration B={0m, 5m, 10m, 15m, 25m}. Black line: entropy corresponding to the error-free data set.

The simulated experiments carried out until now have been useful to assess that the entropy of the ABF profile increases at the increase of the standard deviation of the phase errors corrupting the data, assuming a minimum value for small (tending to 0) error vectors which corresponds to the error-free entropy. This is true independently of the baseline number and their uniformity. As a consequence, it is reasonable to conclude that the minimization of the entropy is a good criterion for phase calibration. The next objective is to verify the degree of accuracy that can be achieved in the reconstruction of the profile, especially considering the implementation of the iterative search of the solution. Since the interest is here in measuring the accuracy in the retrieval of the profile shape, after the entropy minimization the resulting height shifts have been compensated by maximizing the correlation between the reconstructed profile and the error-free profile. Notice that in what follows the interest is in evaluating the performance that can be obtained in Step 3 of the calibration chain. As a consequence, here vectors $\boldsymbol{\delta}$ have been simulated as Gaussian random variables expressing the DEM errors independent from baseline to baseline, thus their standard deviation σ_δ will be expressed in meters. Moreover, to resemble the multilook averaging with which interferograms are estimated at Step1, phase errors have been boxcar- averaged in range and azimuth with a 11×11 window.

To get a reconstruction performance which is independent from the inaccuracies intrinsic with an iterative procedure, an exhaustive minimization has been implemented and taken as a reference. Due to feasibility problems, this means that K is constrained to be equal to 3. Three different double-baseline configurations have been considered, by holding the phase error standard deviation fixed at $\sigma_\delta = 10\text{m}$. The first considered baseline distribution is uniform with a ratio between the minimum and the maximum baseline length equal to 0.5. The ratios corresponding to the second and the third non-uniform configurations are respectively equal to 0.3 and 0.25. For the three of them, the overall baseline length is 20m. In other words, the degrees of non-uniformity increases from the first to the third distribution. In Figs. 3.27-3.29 the ABF tomograms are shown for three configurations obtained from the error-free dataset, from the corrupted one, and after the minimum entropy (hereafter referred as ME) correction. It is possible to observe that even in the most unfavorable case the minimization algorithm is able to return a profile very similar (if not identical) to the error-free one, once again validating the effectiveness of entropy minimization. It also worth noting that the both the peak and relative profile amplitudes are accurately recovered, i.e. the ABF filtering is not affected by self-cancellation. This is already an indication that ME is a good candidate for the calibration of MB data set over forested areas, the analysis of which strongly relies on radiometric fidelity of the imaging technique. As a further comment, these kinds of scenarios are challenging for the conventional MB calibration techniques.

As already emphasized, the exhaustive method becomes unfeasible when $K > 3$ and an iterative algorithm is needed to solve the minimization problem. Both the coordinate descent (hereafter referred as CD-ME) and the sequential exhaustive (SE-ME) have then been implemented. The CD-ME iterations have been initialized with that vector which contains equal correction phases[2] and that minimize the profile

[2] This is equivalent to a very rough scan of the multi-dimensional space of the solution along its multi-dimensional diagonal.

entropy. The first objective is to understand until which extent the profile reconstruction performance of an iterative method degrades with respect to the exhaustive one. This comparison is possible for $K = 3$, and the same 3-image acquisitions considered before have been used. Notice that in such a case the SE-ME solution coincides with the exhaustive one, thus only the CD-ME optimization has been taken into account. To get a performance measure, the following normalized error energies have been calculated:

$$En_1 = \frac{\sum_{n=1}^{N}\left[f_{CD}(z_n) - f_{ef}(z_n)\right]^2}{\sum_{n=1}^{N} f_{ef}^2(z_n)},$$

$$En_2 = \frac{\sum_{n=1}^{N}\left[f_{EX}(z_n) - f_{ef}(z_n)\right]^2}{\sum_{n=1}^{N} f_{ef}^2(z_n)}, \qquad (3.2)$$

$$En_3 = \frac{\sum_{n=1}^{N}\left[f_{CD}(z_n) - f_{EX}(z_n)\right]^2}{\sum_{n=1}^{N} f_{EX}^2(z_n)},$$

where $f_{CD}(z)$ and $f_{EX}(z)$ denote the ABF profiles obtained after the CD-ME optimization and the exhaustive one, respectively, while $f_{ef}(z)$ denotes the error-free profile. While En_1 and En_2 express respectively the reconstruction error between CD-ME and the exhaustive solution with respect to the error-free profile, En_3 expresses the error between the iterative and the exhaustive solutions. Notice that En_1 and En_2 already take into account radiometric inaccuracies in the profile reconstruction. The obtained error energies are shown in Fig. 3.30 reported in percentage in the interval between 0% and 2%. It is apparent that both the CD-ME and the exhaustive algorithms reach a good performance with error energy lower than 0.3% if the tracks are uniform [Fig. 3.30(a)], and no relevant differences can be observed between the two solutions. In the second analyzed case, in which the ratio between the minimum and the total baseline equals 0.3 [Fig. 3.30(b)], both the methods performs still very well when the non-uniformity extent increases, with error energies lower than 0.5% in the most of the azimuth lines and lower than 3% in some isolated points. In these points it is possible to recognize a local performance worsening when the ratio between the minimum and the maximum baseline increases further [Fig. 3.30(c)]. In particular, in the third configuration some error peaks arise in a few pixels for which En_1 is between 4% and 10%. Anyway, in the most of the analyzed coordinates the error energy approaches the null value and no relevant differences between the exhaustive and the CD-ME solutions can be seen in this first comparison. To sum up, the CD-ME solution already demonstrated to be a good candidate for the entropy minimization and, with the chosen initialization, it leads to the global minimum of entropy functional, at least for $K = 3$. Moreover, already in this very poor baseline sampling, CD-ME constitutes a fast alternative to the exhaustive solution.

The second objective of this analysis is to compare the two individuated candidate algorithms CD-ME and SE-ME. The SE-ME algorithm tries to solve the trade-off existing between computational-burden

and method reliability. A performance analysis has been carried out by measuring the following error energy:

$$En_{SE} = \frac{\sum_{n=1}^{N}\left[f_{SE}(z_n) - f_{ef}(z_n) \right]^2}{\sum_{n=1}^{N} f_{ef}^2(z_n)}, \tag{3.3}$$

where $f_{SE}(z)$ is the ABF vertical profile obtained after the minimum entropy optimization by means of the sequential exhaustive algorithm. En_{SE} has then been compared with En_1. The performance has been evaluated with different baseline configurations by fixing the phase error standard deviation to $\sigma_\delta = 10\,\mathrm{m}$. For this analysis the very important TempoSAR 2008 baseline configuration has been investigated ($B = \{0\mathrm{m}, 5\mathrm{m}, 10\mathrm{m}, 15\mathrm{m}, 25\mathrm{m}\}$), together with a $K = 6$ uniform baseline distribution ($B = \{0\mathrm{m}, 5\mathrm{m}, 10\mathrm{m}, 15\mathrm{m}, 20\mathrm{m}, 25\mathrm{m}\}$) and the full $K = 10$ uniform baseline distribution. Notice that the first one can be considered as a thinned non-uniform version of the second with the same total baseline.

ABF tomograms for the TempoSAR baselines are reported in Fig. 3.31, normalized with respect to the peak amplitude at each azimuth coordinate for better visualization. The CD-ME and SE-ME calibrated tomograms are very similar to the error-free one, although some residual miscalibrations are still present at a few isolated coordinates. Just from a visual comparison, the SE-ME solution looks slightly better than the CD-ME. Fig. 3.32 reports the same plots, but for the full uniform baselines. In this case, the corrupted tomograms is worse than in the previous, even if obtained with the same σ_δ. This is due not only to a different realization of the phase error vector, but also to the increased number of baselines [33]. Nevertheless, both CD-ME and SE-ME reconstructions are very good and similar (if not identical) to the error free tomogram. Differently from before, in this case CD-ME is better than SE-ME. This is likely to be due to a sort of error propagation starting from the first two dimensional searches and propagating through the next one dimensional searches. In other words, with SE-ME sharpness is not maximized jointly, but it is maximized at each baseline conditionally to the maximization reached at the previous baselines. Conversely, through the iterated update process, CD-ME always tries to maximize the sharpness jointly for all the baselines. This trend becomes apparent at the increase of the number of images in the stack. However, it is still possible to affirm that, although its sub-optimality, the conditioned optimization still can reach a good reconstruction quality in the analyzed cases.

Fig. 3.33 compares En_{SE} has then been compared with En_1 for the three baseline configurations under test. Error energies have been found to follow the same trend independently of the baselines. First of all, both En_{SE} and En_1 are much lower than 1% for the majority of azimuth coordinates, and a few number of isolated points, they are below 3%. In general, SE-ME is slightly better than CD-ME in those points, and this happens mainly with a lower number of baselines. When the number of baselines reach the full configuration, as already pointed out, CD-ME is better than SE-ME. It is worth stressing the spiky nature of these errors, meaning that they could be removed with a post-filtering. It also worth noting that CD-ME presents higher errors especially around azimuth bins 40 and 200, and this is true independently of the

baseline configuration. These two coordinates correspond approximately to the borders between bare area and forested area, and vice versa. This might suggestion a (low) dependency of the entropy minimization on the analyzed profile, even if not at a high extent. Nevertheless, this topic is far from the purpose of this report.

Fig 3.34 compares En_{SE} with En_1 by fixing the baseline configuration to the TempoSAR 2008 one, and by varying σ_δ. In particular, $\sigma_\delta = \{2.5\text{m}, 5\text{m}, 15\text{m}\}$ have been considered. It is possible to observe that for both CD-ME and SE-ME the obtained error energies are not sensitive to the error standard deviation, and they look almost identical. This is a clear indication of the fact that the full profile information is used in the calibration, independently from the imaged target. In other words, the method do not make preferences of profiles which could be less be affected by lower miscalibration levels. Not only, but a confirmation is given tha the entropy (i.e. the sharpness) of the ABF profile represents a parameter which really can discriminate between a calibrated and a non-calibrated data vector, and its minimization is able to recover the scattering information.

To conclude this section, it is worth to sum up and stress the results of this simulated analysis:

1. the entropy/sharpness of the ABF vertical profile increases/decreases at the increase of the standard deviation of the phase errors;
2. the minimization/maximization of the entropy/sharpness is a good criterion for phase calibration, and allows to recover the error-free profile;
3. CD-ME and SE-ME optimization procedures are able to reconstruct the error-free profile with a high accuracy. However, SE-ME performance degrades at the increase of the number of baselines as it is based on a conditioned optimization. Moreover, in the cases in which SE-ME outperforms CD-ME, the performance gain is no worth compared to the increase of the computational load. In fact, as it is shown in Appendix 3.A, the computational load of SE-ME is at least one order of magnitude bigger than the computational load of CD-ME;
4. CD-ME is globally the best performing optimization procedure, and it will be used in the following. It leads to error energies lower than 1% in the majority of the analyzed cases, independently from the MB acquisition configuration (uniform/not-uniform, with poor/rich baseline sampling) and the standard deviation of the phase errors. This is due to the fact that entropy expresses the miscalibration degree of the data vector, independently of the imaged scatterer and the different effects that a miscalibration can cause on its response. Moreover, the chosen initialization (one identical phase correction for all the baselines minimizing the profile entropy) has demonstrated to be accurate enough to guarantee the convergence of the iterations to a global minimum in the most of the cases. Nevertheless, a slight profile dependency on the optimization results has been observed, even if the error energy there do not exceed the 10%. These cases correspond to isolated pixels in the range-azimuth plane, whose calibration inaccuracies can be compensated by means of basic local averages.

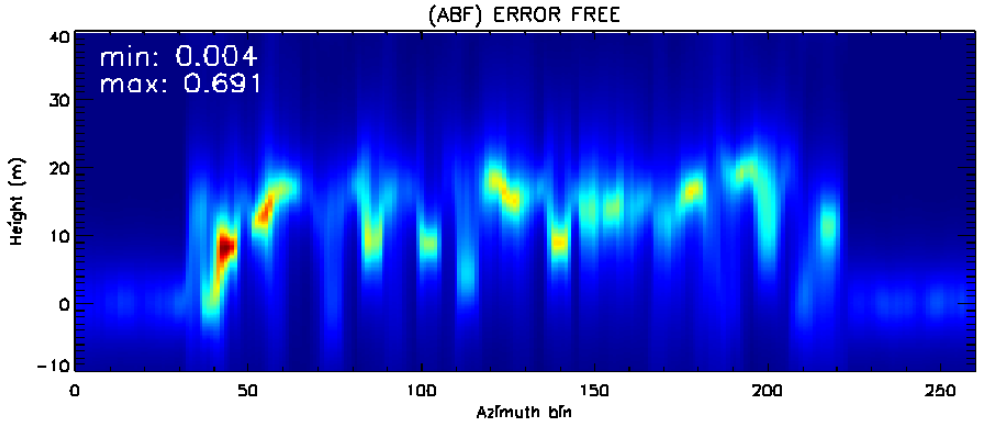

(a)

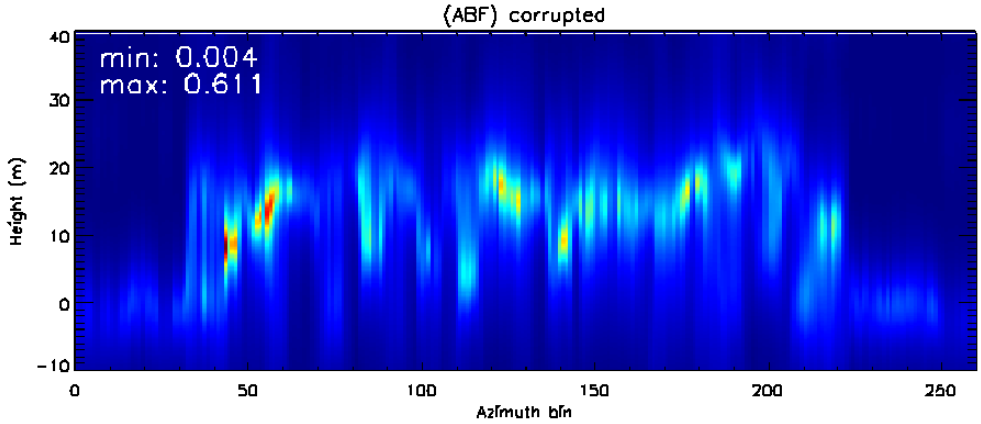

(b)

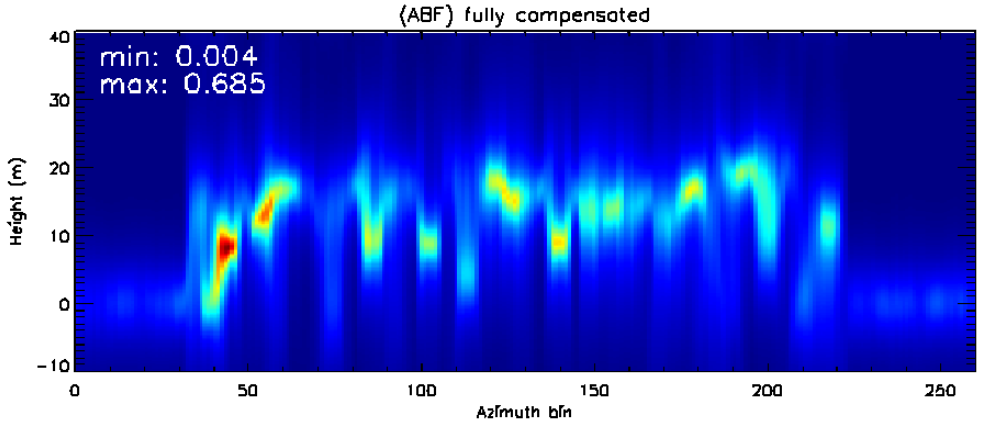

(c)

Figure 3.27 – ABF tomograms in the azimuth-height plane for the range line under test, baseline configuration B={0m, 5m, 10m}. (a) Error-free; (b) corrupted by incoherent phase variations with σ_δ = 10m (single realization); (c) reconstructed by means of an exhaustive search.

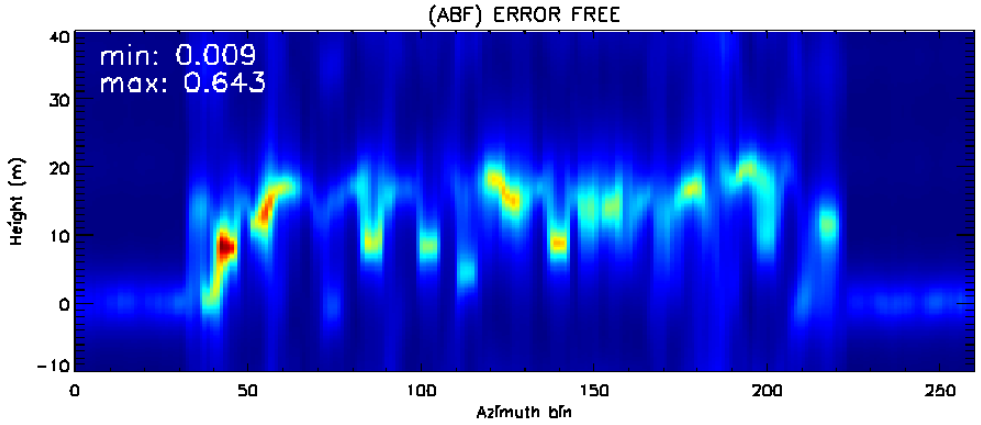

(a)

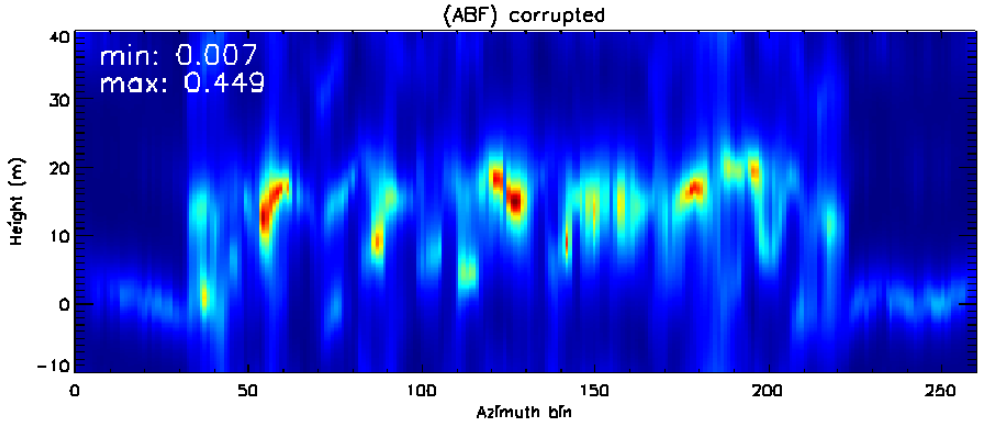

(b)

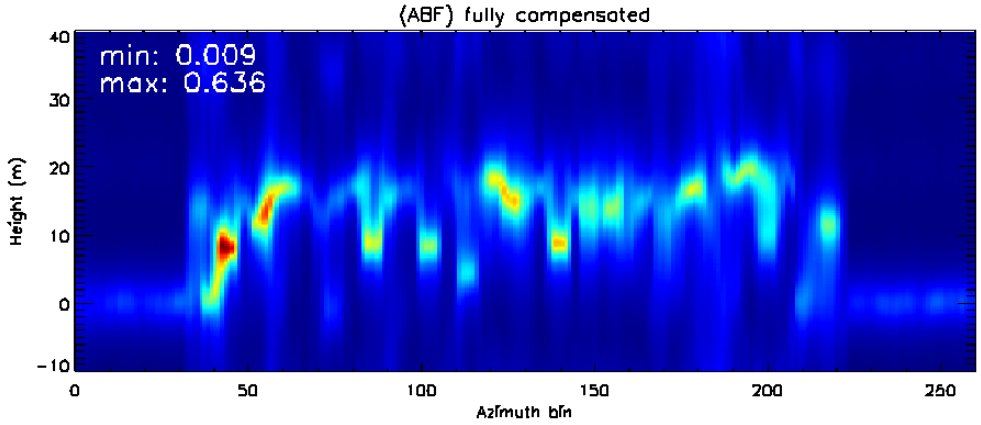

(c)

Figure 3.28 – ABF tomograms in the azimuth-height plane for the range line under test, baseline configuration B={0m, 5m, 15m}. (a) Error-free; (b) corrupted by incoherent phase variations with σ_δ = 10m (single realization); (c) reconstructed by means of an exhaustive search.

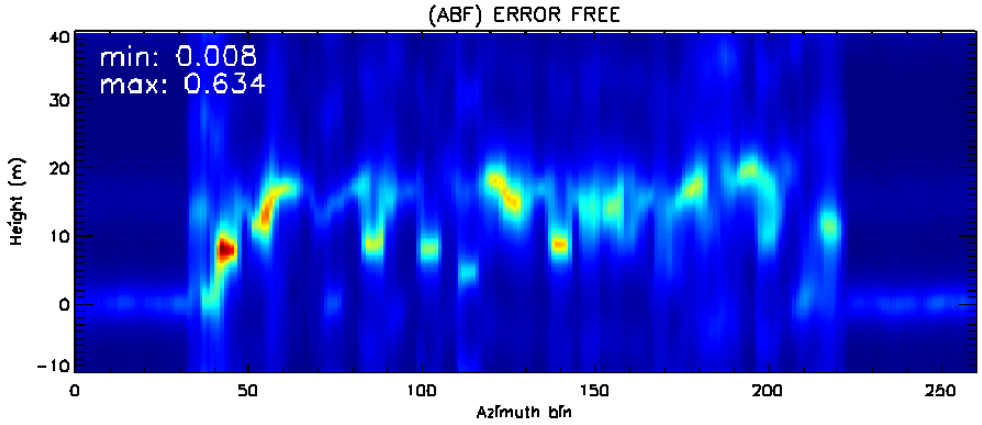

(a)

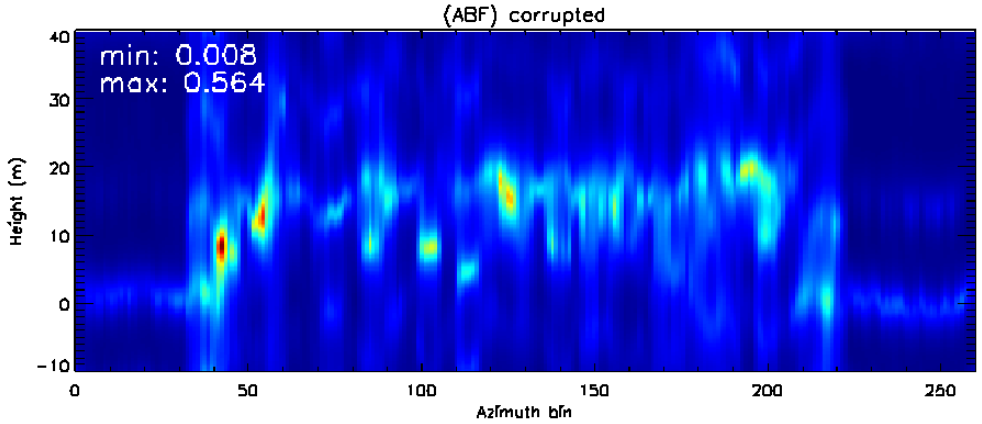

(b)

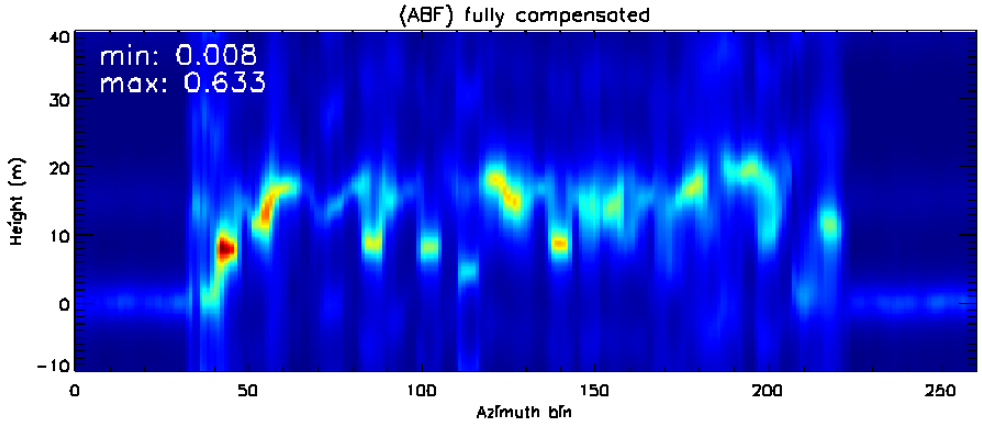

(c)

Figure 3.29 – ABF tomograms in the azimuth-height plane for the range line under test, baseline configuration B={0m, 5m, 20m}. (a) Error-free; (b) corrupted by incoherent phase variations with σ_δ = 10m (single realization); (c) reconstructed by means of an exhaustive search.

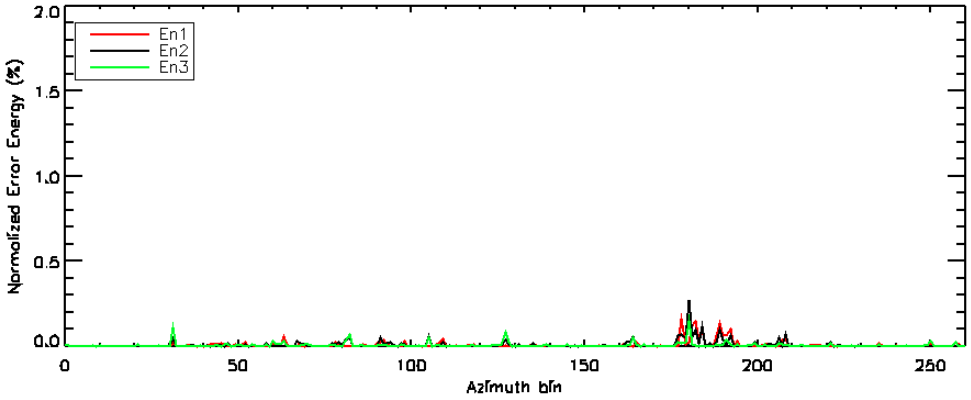

(a)

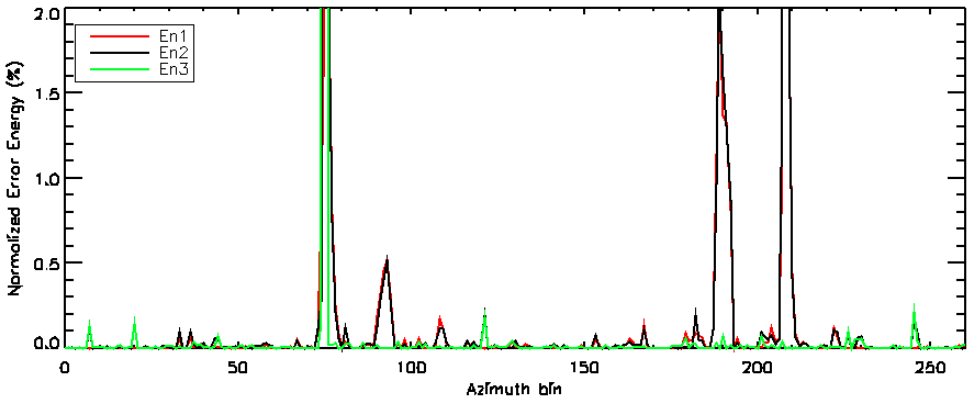

(b)

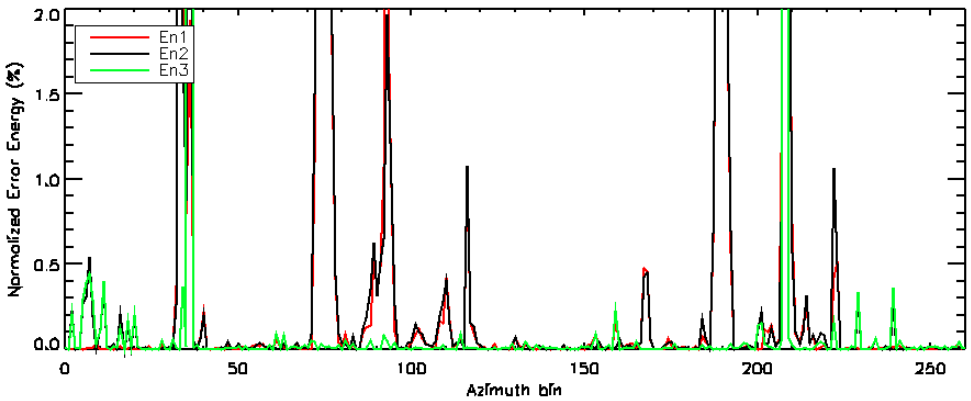

(c)

Figure 3.30 – Normalized energies of the reconstructed errors as a function of the azimuth coordinate, comparisons between the CD and the exhaustive solutions, σ_δ = 10m. (a) Baseline configuration: B={0m, 5m, 10m}; (b) baseline configuration: B={0m, 5m, 15m}; (c) baseline configuration: B={0m, 5m, 20m}.

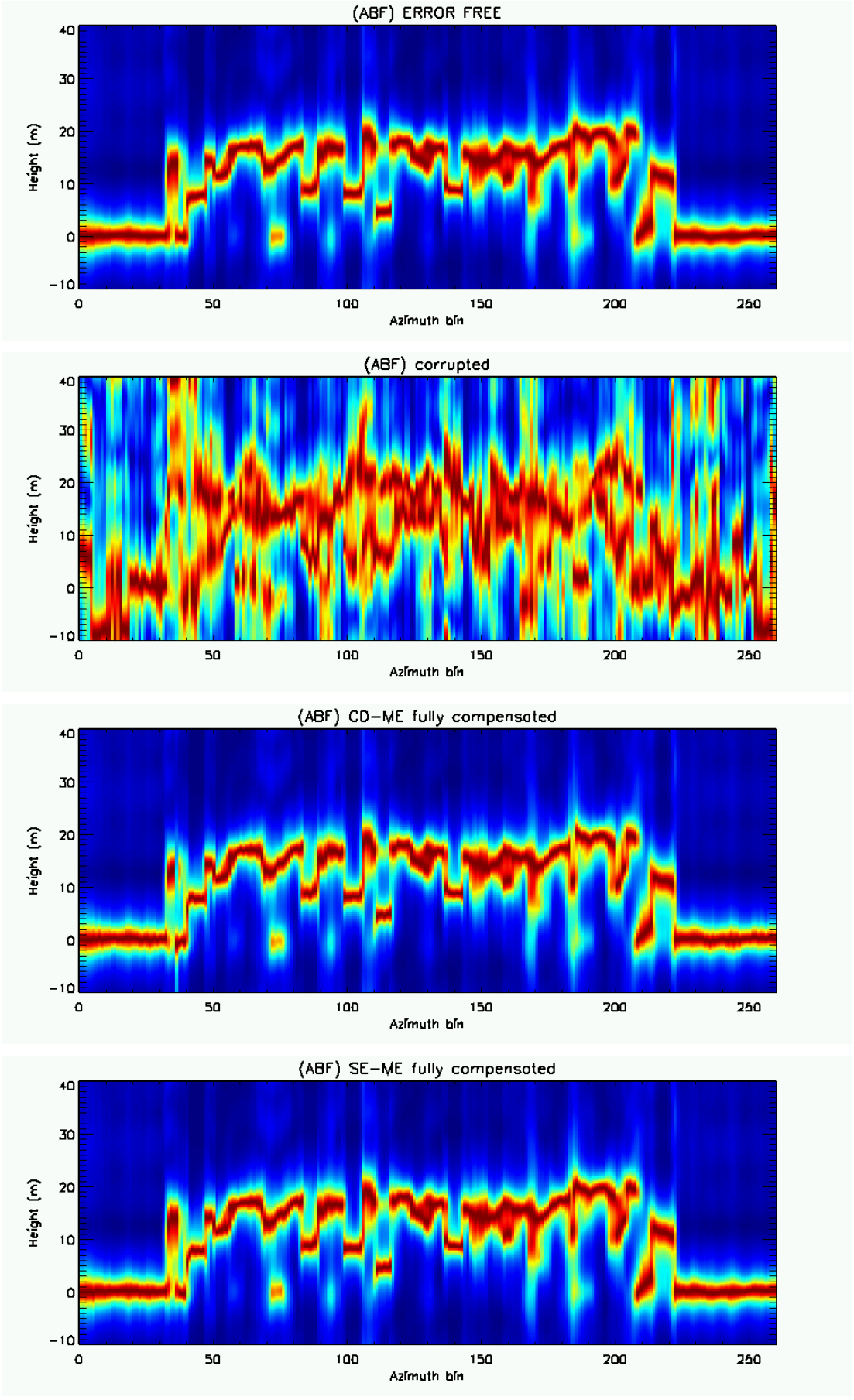

Figure 3.31 – ABF tomograms in the azimuth-height plane for the range line under test, B={0m,5m,10m,15m,25m}, with σ_δ = 10m. From top to bottom: (a) Error-free; (b) corrupted; (c) CD-ME; (d) SE-ME.

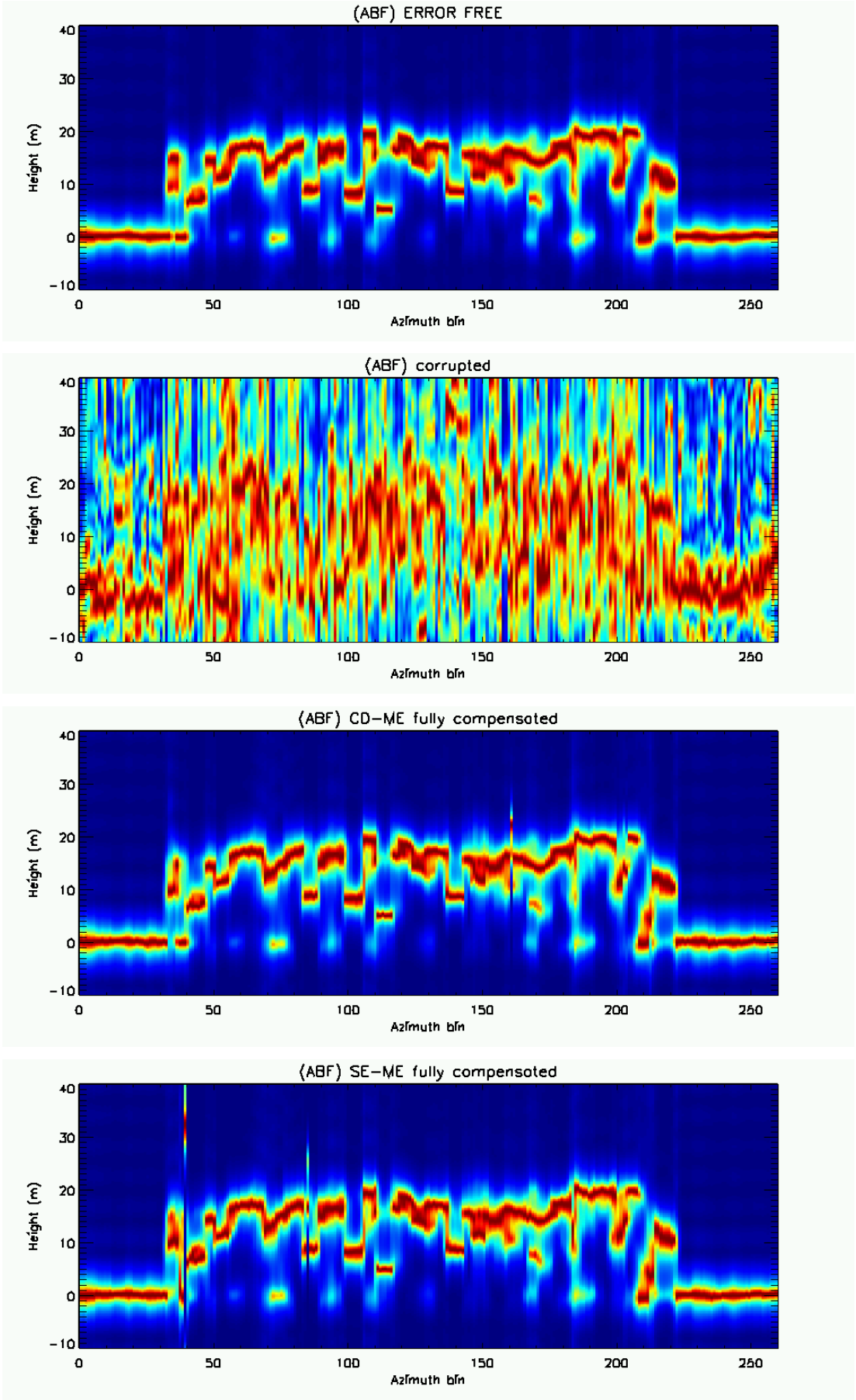

Figure 3.32 – ABF tomograms in the azimuth-height plane for the range line under test, B={0m,5m,10m,15m,20m, 25m,30m,35m,40m,45m}, with σ_δ = 10m.. From top to bottom: (a) Error-free; (b) corrupted; (c) CD-ME; (d) SE-ME.

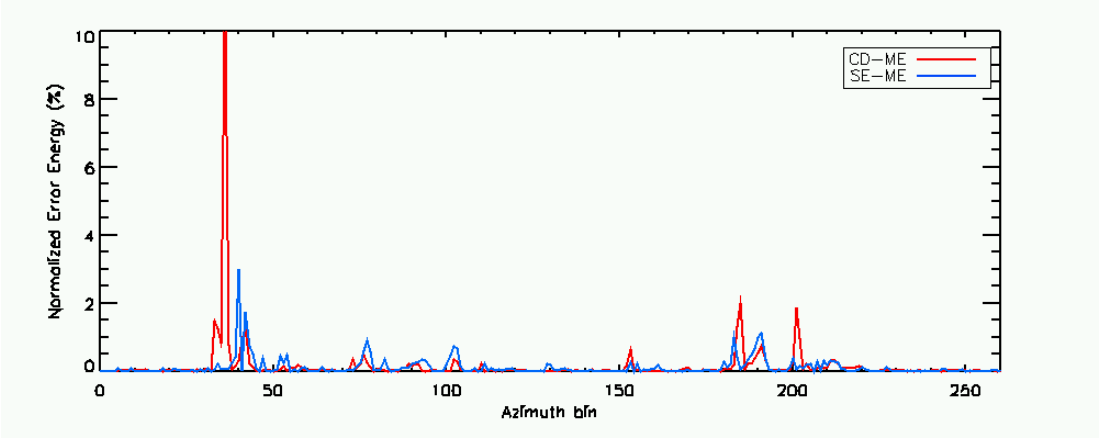

(a)

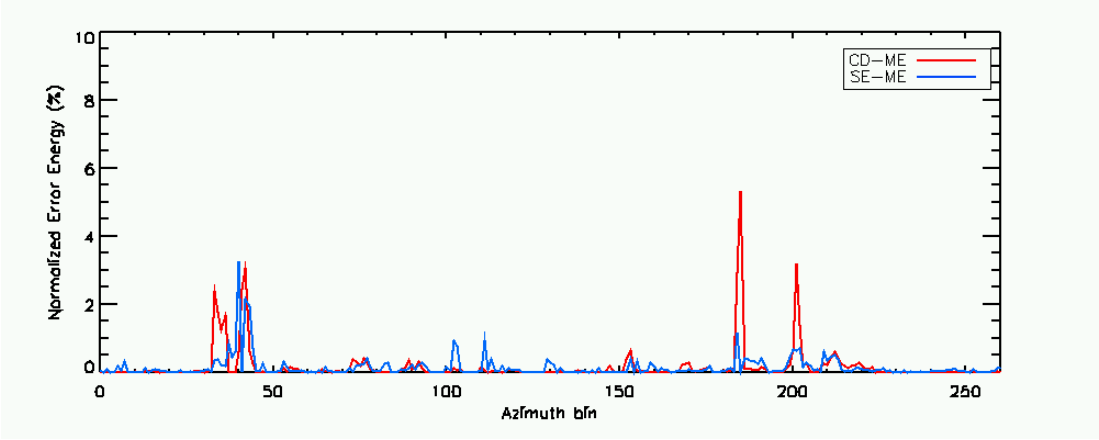

(b)

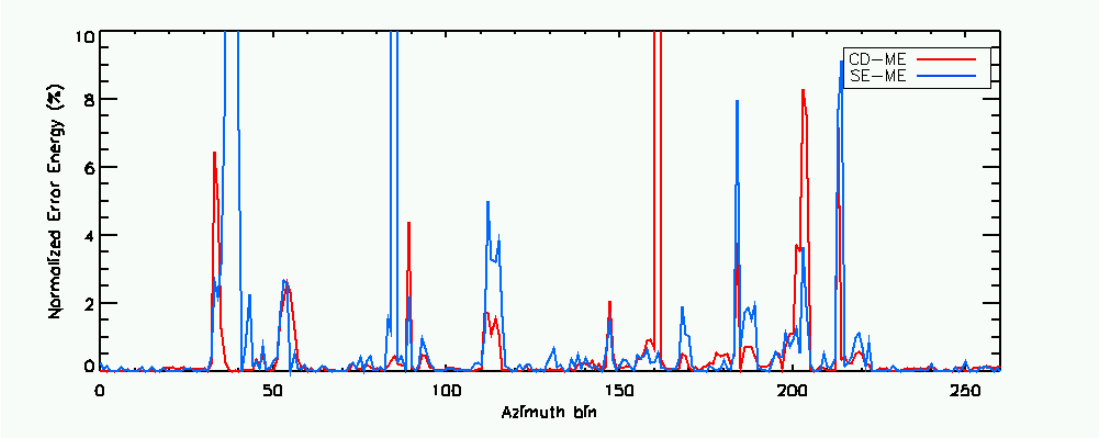

(c)

Figure 3.33 – Normalized energies of the reconstructed errors as a function of the azimuth coordinate, comparisons between the CD and the SE solutions, incoherent phase variations with σ_δ = 10m. (a) Baseline configuration: B={0m, 5m,10m,15m,25m}; (b) baseline configuration: B={0m, 5m,10m,15m,20m,25m}; (c) baseline configuration: B={0m, 5m,10m,15m,20m,25m,30m,35m,40m,45m}.

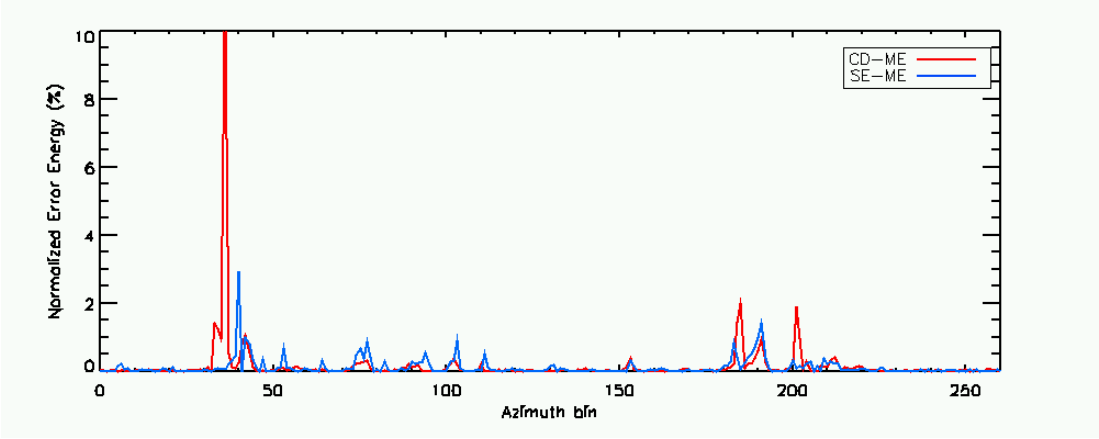

(a)

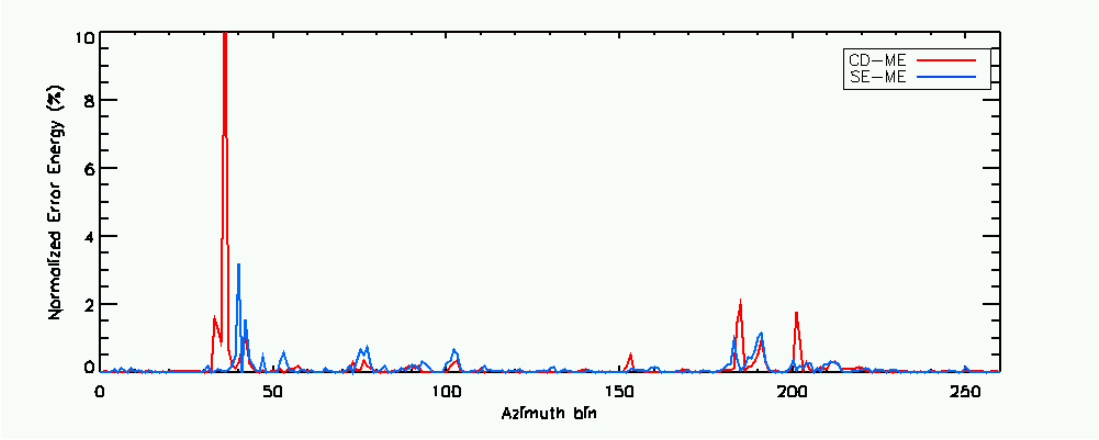

(b)

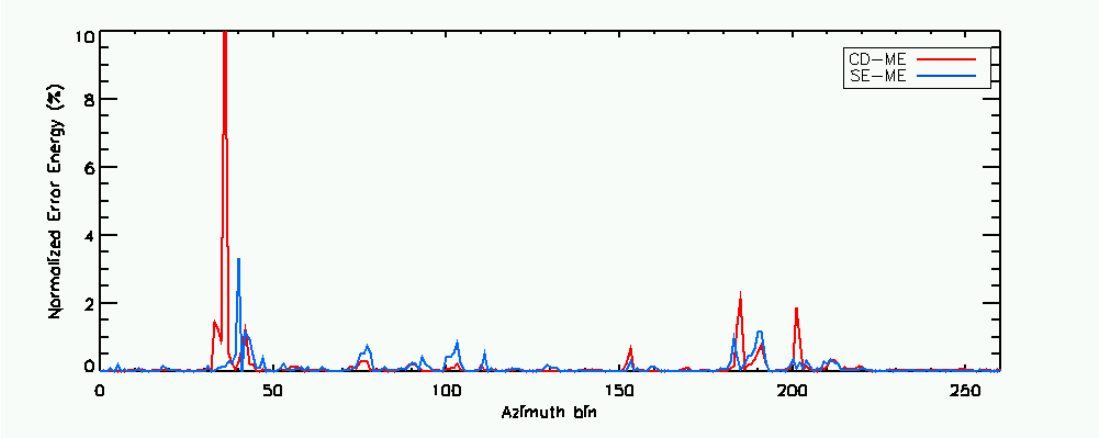

(c)

Figure 3.34 – Normalized energies of the reconstructed errors as a function of the azimuth coordinate, comparisons between the CD and the SE solutions, baseline configuration: B={0m, 5m, 10m, 15m, 25m}. (a) σ_δ = 2.5m; (b) σ_δ = 5m; (c) incoherent phase variations with σ_δ = 15m.

3.2.2 Estimation of z_0: performance analysis

The objective of this Section is to evaluate the performance obtainable in the estimation of z_0 and, consequently, of the original calibration errors in Step 5 of the calibration chain. As explained in Section 2.3.2, these operations are performed by the last processing block of the proposed chain by means of a "forward-backward" procedure starting from a reference pixel and exploiting the slow variability of the phase errors we want to estimate. Noteworthy, this operation is not strictly needed for tomographic purposes, since after the minimum entropy step it is already possible to isolate the complex reflectivities and to estimate the vertical profiles by means of an ABF filter. Anyway, as already discussed in the previous chapter, the contribution of the phase errors have been compensated in the signal $\mathbf{y}_C$ but it is still an unknown of the problem. On the other hand, for applications different from SAR Tomography it would be useful to know the extent of these phase offsets. Thus, the following analysis is worth to be performed in order to assess the goodness of the last processing block in isolating the DEM contribution from the undesired calibration errors.

Here the performance is derived by means of a simulated analysis evaluating the RMSE obtainable in the estimation of z_0 with a simple BF, as proposed in Section 2.3.4. 10000 realizations of the miscalibration phase vectors have been generated for each variation of the parameter of interest. At each realization, z_0 has been estimated through a BF spectral estimate. Then, the root mean square error (RMSE) of the estimation has been evaluated in each analyzed case. As a benchmark, the hybrid Cramér-Rao bound (HCRB) was calculated using the formulation in [52] assuming an infinite signal-to-noise ratio. For the sake of analytical simplicity and generality of the results, it is useful to express $\mathbf{k}_z$ normalized with respect to the maximum value of its elements, say $k_{z,\max}$, and z_0 normalized with respect to the height resolution unit $\delta_z = 2\pi/k_{z,\max}$. With this choice, the obtained results are independent from the baseline lengths and the incidence angle (which affect the absolute value of $\mathbf{k}_z$). They only depend on the baseline distribution and $\tilde{\sigma}^2$.

In Fig. 3.35 the estimation RMSE (continuous lines) have been plotted as a function of $\tilde{\sigma}$ and for different values of K (indicated with different colors). Baselines have been designed uniform for the sake of simplicity. The HCRB has been superimposed for each K (dashed lines). Of course, z_0 is perfectly estimated without errors for $\tilde{\sigma} = 0$ (no miscalibration) independently of the value of K. At the increase of $\tilde{\sigma}$, the RMSE increases, still reaching the HCRB. It has been verified that the estimation bias is null. This means that BF is the best estimator of z_0 in that zone, and no other better performing estimator can be found. Dependently on K, for a further increase of h_0, the RMSE starts to deviate from the HCRB, in a way resembling a threshold effect. The value of $\tilde{\sigma}$ in which this deviation happens depends on K: the higher K, the higher the "cut-off" value of $\tilde{\sigma}$. To make an example, in real applications with airborne data $k_{z,\max}$ approaches approximately 0.5 (at least in near-mid range), leading to $\delta_z = 15\text{m}$. As a consequence, a RMSE of 0.1 resolution units (r.u.) corresponds to 1.5m, a still acceptable value. From the curves of Fig.

3.35, a RMSE of 0.1 r.u. is reached for instance at $\tilde{\sigma} = 0.05$ for $K = 5$ and $\tilde{\sigma} = 0.075$ for $K = 20$. Nevertheless, it is expected that $\tilde{\sigma}$ does not exceed 0.01 in the hypothesis of high χ. In this case, z_0 can be estimated with a RMSE lower than about 20cm independently from K. Not only, but BF is the best estimator there, as it reaches the HCRB.

So far, we uniform baseline distributions have been considered. With non-uniform distributions and $K > 5$ (what happens in practice), it is not expected a dramatic worsening of the performance, even if, depending on the non-uniformity degree, sidelobes with a poor amplitude level could be amplified by the miscalibration. This trend has been verified by comparing the RMSE obtained by a $K = 5$ uniform distribution and the 5-element distribution of the TempoSAR 2008 campaign. Results are plotted in Fig. 3.36. The non-uniform baseline distribution leads to a negligible worsening of the RMSE, which is not of concern.

A very particular case is found with $K = 3$, to which the curves in Fig. 3.37 are referred. As already emphasized many times this is a very interesting limit case. Here, the signal generated by a baseline distribution with $\mathbf{k}_z = \left[0, k_{z,\mathrm{mid}}, 1\right]$ has been simulated, and the related RMSE has been obtained as a function of $k_{z,\mathrm{mid}}$ and for different $\tilde{\sigma}$. In Fig. 3.37, the continuous lines are the RMSEs obtained by processing the non-uniform data stack. It is apparent that in general the RMSE decreases at the increase of $k_{z,\mathrm{mid}}$, i.e. at the reduction of the non-uniformity degree of the baselines. Again, we observe that for $\tilde{\sigma} < 0.01$ the RMSE reaches acceptable levels in the order of magnitude of 0.01 r.u. For $\tilde{\sigma} = 0.04$, no acceptable RMSE values are reached anymore.

In order to improve the estimation performance and to reduce the dependency of the RMSE on the baseline non-uniformity, a feasible approach is to interpolate the available MB signal from a non-uniform distribution to a (virtual) uniform one. Details on this signal interpolation can be found in [27], [53]. This interpolator is very easy to be implemented. Indeed, in [53] it has been demonstrated that this interpolator can be expressed as least-square estimator with a proper loading in the case of small errors, while it assumes a different form for big errors. Nevertheless, concerning the estimation of scatterer height, the performance of the small-scale solution has been found to be equivalent to the one of the complete solution. In Fig. 3.37 the RMSE obtained after baseline interpolation has been plotted for each analyzed case in dashed lines. It is possible to observe that the acceptable performing regions of $k_{z,\mathrm{mid}}$ have enlarged. In particular, for $\tilde{\sigma} = 0.05$ (which is of interest for large χ), an acceptable RMSE can be obtained independently of the non uniformity.

In conclusion, from this simulated analysis in the cases of interest, i.e. when it is possible to reduce our problem to a “small variance” one, the DEM estimation can be effectively performed through a simple BF spectral estimation. As a consequence, the original calibration errors will also be well estimated.

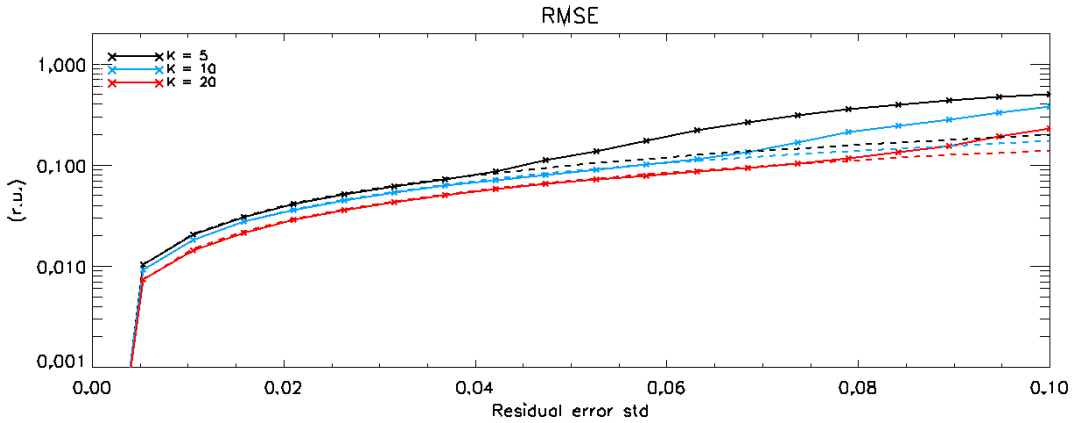

Figure 3.35 – RMSE obtained by estimating z_0 by means of BF as a function of the standard deviation of the residual error and for different values of K, uniform baseline configuration. Continuous lines: RMSE; dashed lines: HCRB.

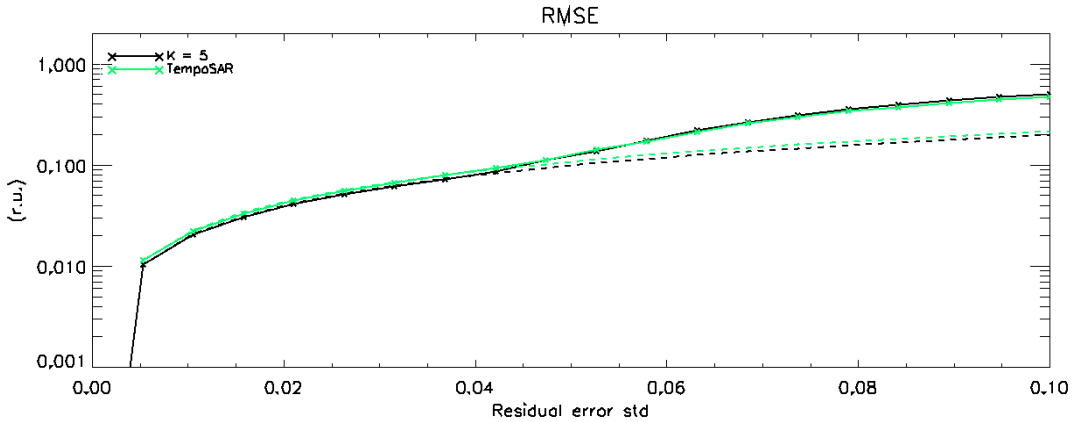

Figure 3.36 – RMSE obtained by estimating z_0 by means of BF as a function of the standard deviation of the residual error for K=5: comparison between an uniform baseline configuration (black) and the TempoSAR baseline configuration (green). Continuous lines: RMSE; dashed lines: HCRB.

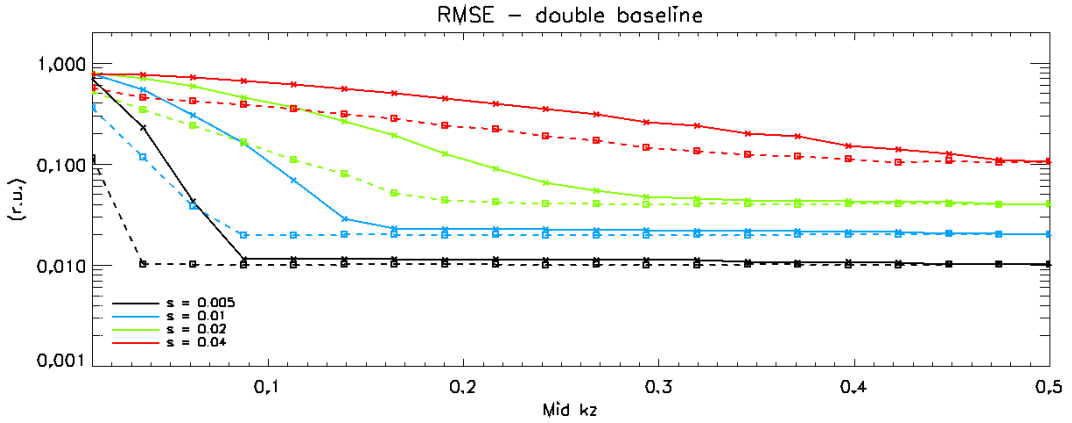

Figure 3.37 – Case K = 3, RMSE obtained by estimating z_0 by means of BF as a function of the mid k_z and for different values of the standard deviation of the residual error. Continuous lines: RMSE with the non-uniform baselines; dashed lines: RMSE after baseline interpolation.

As a final experiment, an example of estimated DEMs from the simulated PolSARProSim data stack is reported in Fig. 3.38. The full uniform baseline distribution has been considered, i.e. the one already used many times before. Data have been corrupted with random phase noise vector $\boldsymbol{\psi}$, see model in (1.28), with standard deviation $\sigma_{\psi} = 0.32\pi$. In particular, in Fig. 3.38(a) is shown obtained from the error free DEM stack $\tilde{\mathbf{y}}_D$, where it is possible to recognize clearly the bare areas, with a height centroid located at 0m, and to distinguish it from the forest area in the middle of the slice, whose height centroid is located at around 18m. From the figure it is also possible to recognize the presence of inflated sidelobes due to residuals of baseline to baseline differences in the estimated DEM height, i.e. the vector $\boldsymbol{\delta}$. Fig. 3.38(b) refers to vector $\tilde{\mathbf{y}}_D$ corrupted by the phase noise, where both the disturbances are present coming from phase miscalibrations and vector $\boldsymbol{\delta}$. Here, ambiguities arise and the extent of the sidelobes could lead to a wrong estimate of the height centroid. In Fig. 3.38(c), after the estimation of the vector $\boldsymbol{\delta}$ through the minimization of the entropy, the BF spectrum of the signal $\mathbf{y}_D(x,r)$, which is the input of the last processing block and only contain the original pahse perturbation to be estimated. Finally, Fig. 3.38(d) shows the BF spectrum obtained from the fully compensated DEM, where the phase miscalibrations have been suppressed and the sidelobes due to residual DEM estimation errors have been rejected, i.e. after Step 5. The maxima of the obtained "clean" MB DEM in Fig. 3.38(d) perfectly matche with the maxima of the DEM in Fig. 3.38(a), thus demonstrating the capability of Step 5 in estimating the miscalibration phases.

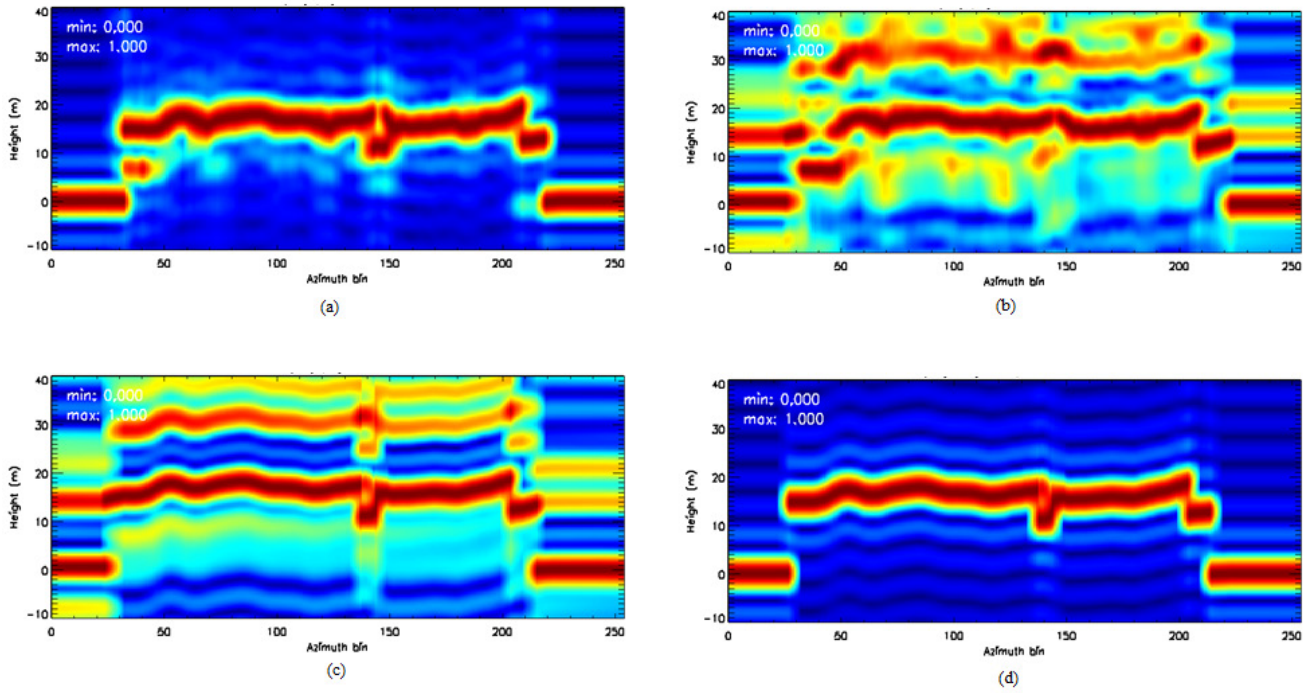

Figure 3.38 – BF tomograms of MB interferograms, uniform full baseline configuration (K = 10). (a) Error-free; (b) miscalibrated, $\sigma_{\psi} = 0.32\pi$; (c) after ME optimization; (d) fully calibrated.

3.2.3 Global performance analysis

In the previous sections each part of the proposed calibration chain has been analyzed as a stand-alone block and tests with simulated data have been carried out in order to assess its performance from both a qualitative and a quantitative point of view. Here, we link together every parts previously described and we analyze the global performance of the proposed calibration algorithm. In other words, the calibration chain is considered as a black box and the calibration performance is measured at its output. The algorithm has been implemented in a single IDL code consisting in the following main functions, corresponding to the Step discussed in Section 2.3:

Step 1

Estimation of the interferogram at each baseline with respect to the master track, starting from the corrupted MB data stack.

Step 2

Compensation of the complex interferogram at each baseline from the corrupted data. The output of this processing step is a MB signal containing either the scattering information free from miscalibrations and the residual incoherent phase variations from baseline to baseline. This spurious contribution is due to the processing itself and has to be properly compensated.

Step 3

Estimation of the incoherent phase contributions by means of CD-ME algorithm.

Step 4

Compensation of these quantities from the estimated complex MB interferograms. The output signal from this block is the one used to estimate to miscalibration phases.

Step 5

Miscalibration phase vector estimation from the DEMs, by means of a forward-backward procedure from a starting reference point.

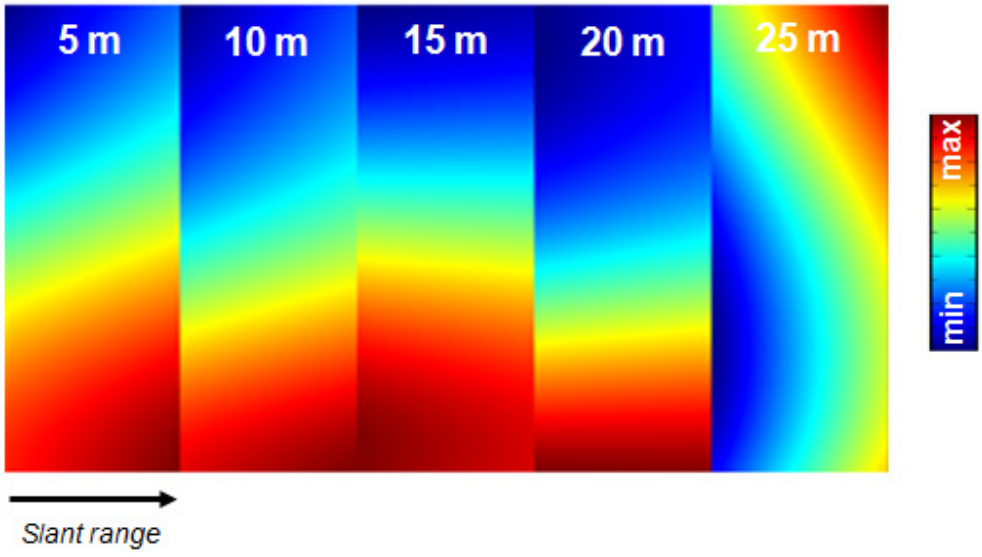

Figure 3.39 – Phase screens estimated from TempoSAR'08 data.

Finally the estimated miscalibration phases are compensated from the MB corrupted data stack to get the calibrated data stack ready for any other processing.

In this Section, the results of a simulated analysis aimed to test the whole processing chain will be shown and discussed. The analysis has been carried out considering again the baseline distribution of the TempoSAR campaign, as it is of particular interest for the next experiments with real data. In particular, to corrupt the PolSAR-ProSim stack we used phase screens previously estimated with the CS technique from the real data acquired during the TempoSAR'08 campaign. For each track, a cut of them has been extracted in order to adapt them to the dimensions of the PolSARProSim dataset. The resulting phase screens are shown in Fig. 3.39.

The results obtained in the TempoSAR case are shown in Fig. 3.40. First of all, the ABF tomograms are reported of the error-free and the corrupted data respectively. From the error-free tomogram it is possible to clearly distinguish the bare soil area from the vegetation layer. In the azimuth coordinate interval [50, 200] the volume scattering contribution comes from the top of the canopy, with its maximum located at around 18m height. In this case, the ABF filter is able to properly suppress the sidelobes and multiple maxima can be due to different scattering mechanisms, which could be imaged with a lower quality estimator. In the bare area, the imaged scatterers have spectral maxima to the zero height, where the ground is located. If the ABF filter receives in input the phase corrupted data, then the retrieved spectra look very different. A shift of the maxima can be noticed in both the bare area and in the forested one. Furthermore, the spectrum is characterized by inflated sidelobes at each azimuth coordinate which makes the image ambiguous. The width of the main lobe enlarges, worsening the height resolution. As a consequence, it is no longer possible to estimate with reasonable accuracy the parameters of interest. The estimated interferograms in Step 1 are affected by both the data miscalibration and the contribution of the incoherent phase variations from baseline to baseline. The overall results of the whole calibration chain are in Fig. 3.40, i.e. the ABF tomograms obtained from the data after the compensation of the estimated phase screens. In order to emphasize the importance of CD-ME, the final output which could be obtained without relying on this processing block, i.e. avoiding Steps 3 and 4 is reported as well. It is apparent from the obtained tomograms that the proposed calibration chain is able to estimate the calibration phases and to reconstruct properly the vertical profile. With the exception of some azimuth coordinates, the obtained profiles look very similar, if not identical, to the ABF tomograms obtained from the error free dataset. It is possible to distinguish again the zero-height ground from the vegetation layer and to properly estimate the height centroid where multiple volume scattering contributions occur.

In order to confirm the validity of the proposed method, this simulated analysis has been repeated with the dual baseline configuration $B = \{0\text{m}, 5\text{m}, 15\text{m}\}$. Fig. 3.41 shows the tomograms corresponding to the error-free data set, the corrupted data set, the data set calibrated without CD-ME, and finally the overall calibration result. For this three-image configuration we can repeat the same considerations and get the same conclusions of the previously analyzed case.

In order to evaluate quantitatively the performance, the normalized energy of the error with respect to the error free profile has been calculated. In Figs. 3.42 and 3.43 the obtained error power percentages for

the corrupted dataset (black dashed line), the one calibrated without ME processing (green continuous line) and the final calibrated data, i.e. the output of the whole chain (red continuous line) are compared. As regards the miscalibrated data the error power is higher than 100% for the most of the azimuth lines, whereas the line corresponding to the final calibrated profile stands in general below the 5%. In the TempoSAR case, the only exceptions to this trend are represented by a few azimuth coordinates where the CD algorithm did not converge to the correct point. Furthermore, the analysis of the green line highlights the strong necessity of Step 3 and Step 4, since the mean error percentage is still higher than 30% with error peaks reaching the 100%. When $K = 3$, an higher gain can be obtained by applying this processing block in this case. This is apparent from Fig. 3.43 where the reconstruction error corresponding to the final calibration output stands below the 2% for each azimuth coordinate.

3.3 Conclusions

From the simulated analysis carried out in this Chapter, it is possible to affirm that that the proposed calibration chain exhibits good performance in the estimation of the phase miscalibrations. This is clear from both the qualitative analysis of the tomograms and the quantitative evaluation of the reconstruction error. The primary role of the minimization of the entropy, i.e. of Steps 3 and 4 of the calibration chain, has also been demonstrated numerically. The CD-ME algorithm has been shown to be effective in entropy minimization.

The error plots of Figs. 3.42 and 3.43 have also shown that especially for $K > 3$ the proposed algorithm is not immune to isolated errors in the estimation of the calibration phases. However, as previously emphasized, their removal e.g. by a median filtering is considered to be a feasible way to increase further the calibration performance.

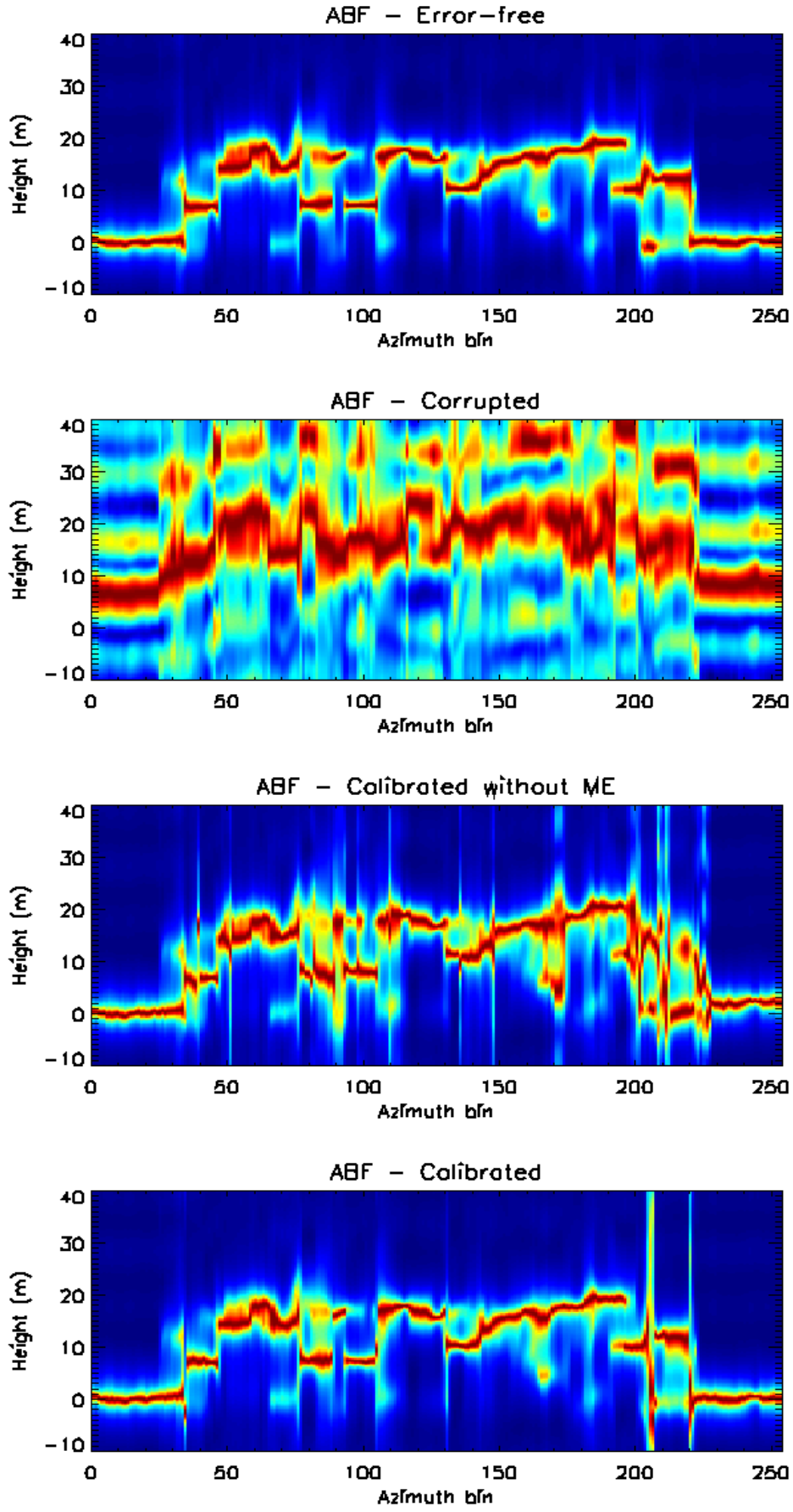

Figure 3.40 – ABF tomograms in the azimuth-height plane for the range line under test, baseline configuration B={0m, 5m, 10m, 15m, 25m}. From top to bottom: (a) Error-free; (b) corrupted; (c) calibrated, no ME; (d) fully calibrated, CD-ME.

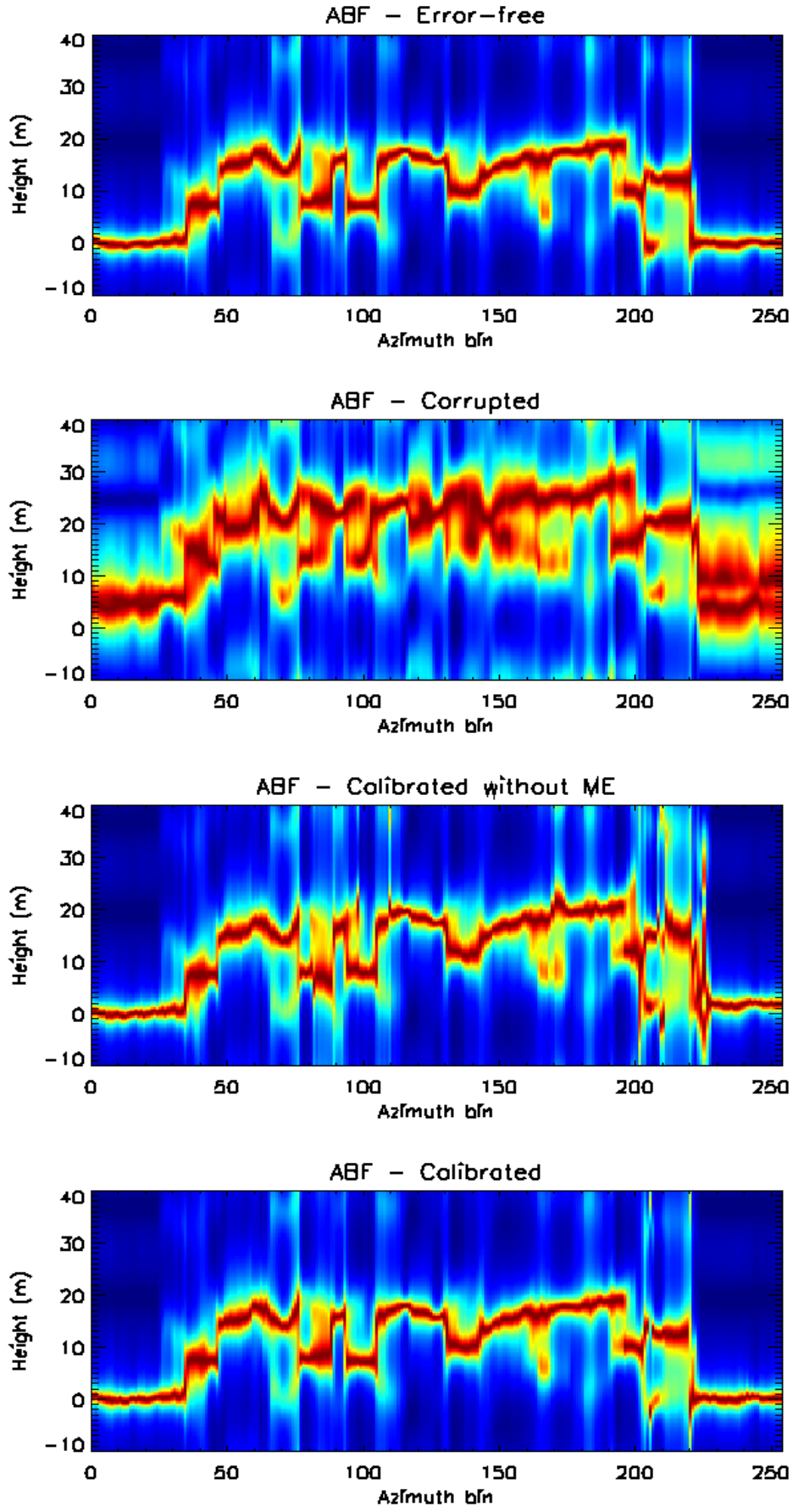

Figure 3.41 – ABF tomograms in the azimuth-height plane for the range line under test, baseline configuration B={0m, 5m, 15m}. From top to bottom: (a) Error-free; (b) corrupted; (c) calibrated, no ME; (d) fully calibrated, CD-ME.

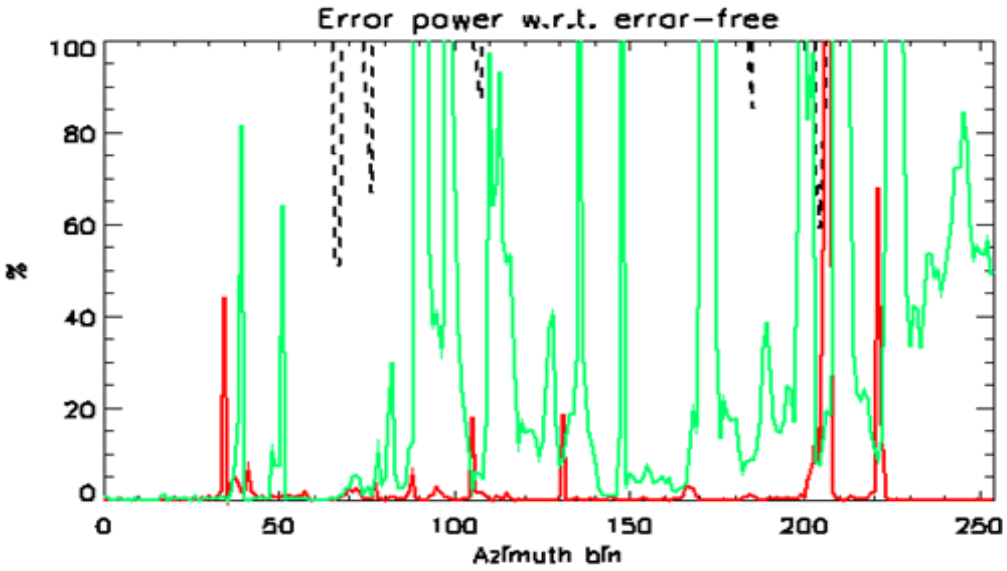

Figure 3.42 – Error power of the ABF tomograms as a function of azimuth with respect to the error-free ones, baseline configuration B={0m, 5m, 10m, 15m, 25m}. Black dashed line: miscalibrated data. Green continuous line: calibrated data without ME. Red continuous line: calibrated data after entropy minimization (CD-ME).

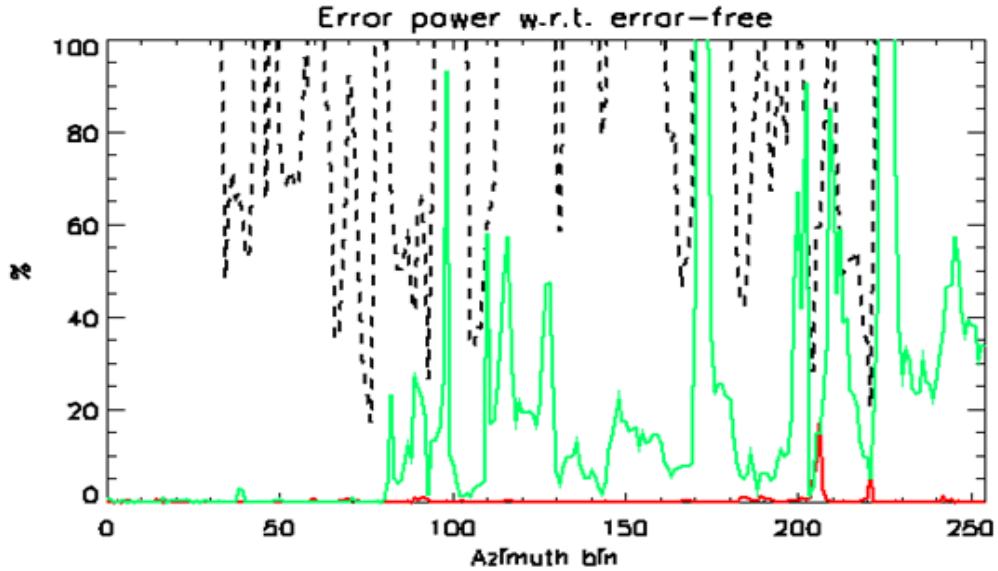

Figure 3.43 – Error power of the ABF tomograms as a function of azimuth with respect to the error-free ones, baseline configuration B={0m, 5m, 15m}. Black dashed line: miscalibrated data. Green continuous line: calibrated data without ME. Red continuous line: calibrated data after entropy minimization (CD-ME).

APPENDIX 3.A

ENTROPY MINIMIZATION: COMPUTATIONAL LOAD

From the available literature, the number of real-valued multiplications needed to calculate the ABF profile in a single range-azimuth cell is:

$$C_{ABF} = K^3 - K + M\left(2K^2 + 4K + 1\right), \tag{A.3.1}$$

being K the number of images in the data stack and M the number of height samples at which the profile is calculated. The entropy of the profile can then be calculated by using $4M + 2$ real valued multiplications.

It is easy to demonstrate that the computational loads in terms of real valued multiplications needed in entropy minimization by means of the exhaustive, the SE-ME and the CD-ME algorithms are respectively given by:

$$C_{EXH} = \left[\left(4M + 2 + C_{ABF}\right)L\right]^{K-1}, \tag{A.3.2}$$

$$C_{SE-ME} = \left[\left(4M + 2 + C_{ABF}\right)L\right]\left[\left(4M + 2 + C_{ABF}\right)L + K - 1\right], \tag{A.3.3}$$

$$C_{CD-ME} = \left(K - 1\right)\left(4M + 2 + C_{ABF}\right)LN_{iter}, \tag{A.3.4}$$

where L is the number of phase samples and N_{iter} is the number of minimizations needed by CD-ME to reach the minimum of the entropy functional.

Quantities (A.3.2)-(A.3.4) have been plotted in Fig. A.3.1 as a function of K, for $M = L = 201$ and $N_{iter} = 5$, the latter being a typical value observed in the analyses reported in Chapter 3. It is apparent that while C_{EXH} increases rapidly with K, C_{SE-ME} and C_{CD-ME} are smaller at least of 4 orders of magnitude. Moreover, C_{CD-ME} is at least one order of magnitude smaller than C_{SE-ME}, and this difference increases at the increase of K.

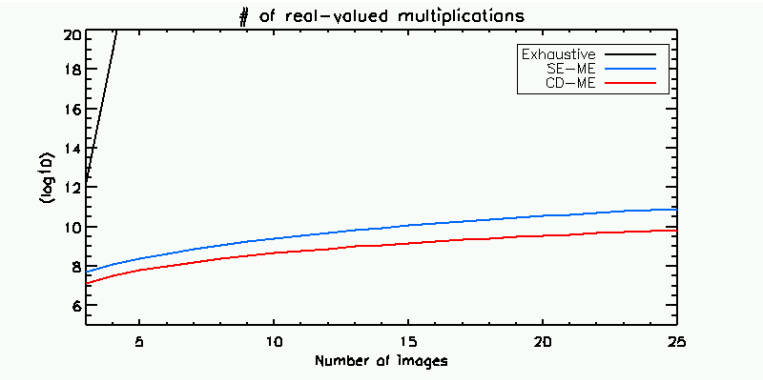

Figure A.3.1 – Computational load calculated in terms of number of real-valued multiplications for different entropy optimization methods, plotted as a function of the number of images in the stack.

CHAPTER 4

EXPERIMENTS WITH REAL AIRBORNE DATA

4.1 The TempoSAR 2008 dataset

After having employed a simulated data to assess the effectiveness of the proposed phase calibration method the processing chain has been applied to real airborne data. In particular, an E-SAR dataset acquired by DLR during the TempoSAR 2008 campaign over the forest stand of Traunstein (Germany) has been processed In Fig. 4.1 the Pauli RGB image and the LIDAR DTM are shown.

The MB stack consists of 5 fully polarimetric L-band images obtained with 5 passes of the airborne platform carrying the radar (the time span is about 1 hour). The baseline configuration is non-uniform, with a minimum nominal sampling distance $d = 5\text{m}$ and an overall nominal synthetic aperture length $L = 25\text{m}$ in the horizontal direction. This test site is very interesting for applications of forest observation since a wide vegetation cover can be recognized with a variety of tree species (e.g. spruces, beeches and white firs). The vegetation height ranges in between 10m and 40m and, noteworthy, the biomass level is varies between 40t/ha and 450t/ha. For this reason, the vegetation layer is often very dense, so the main contribution to the backscattered power comes from the canopy. Hence, the calibration of this kind of data could be a limit case in which an algebraic decomposition (e.g. like in the ALGAE method in [46]) could not be successfully applied everywhere. Nevertheless, since the proposed calibration method exploits the whole vertical profile independently on its shape, it can be applied even in this boundary conditions. As regards the existing methods based on the detection of reliable calibration targets, no theoretical reasons impair, at least in principle, their effectiveness when the full multibaseline stack is available. As already discussed, problems arise in the detection of CSs and PSs when the number of available acquisitions decreases since the evaluation of both the dispersion factor $D(x,r)$ and the ensemble coherence $\gamma_{ensemble}(x,r)$ becomes

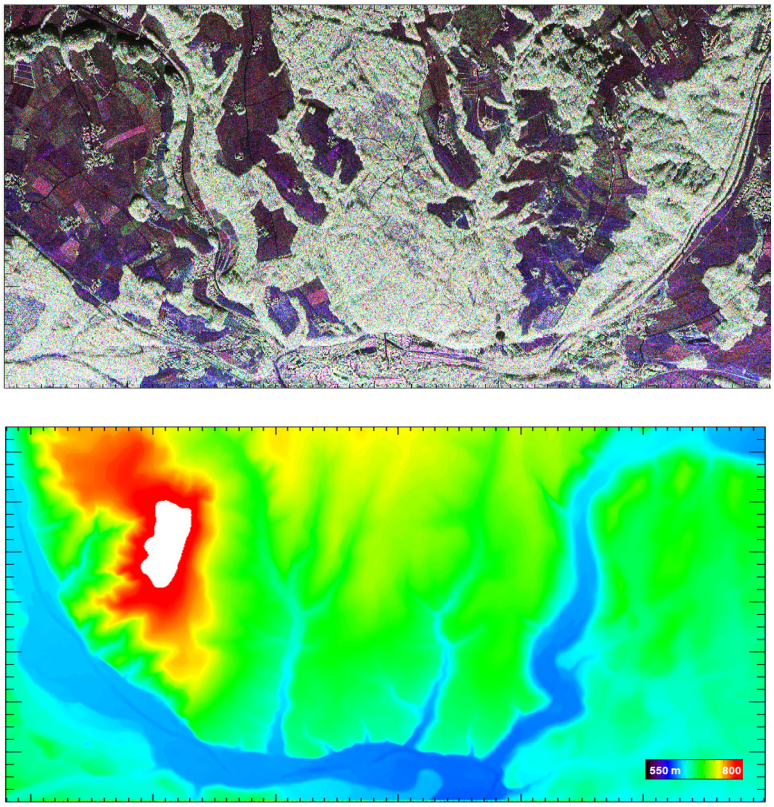

Figure 4.1 – Test site of Traunstein (Germany). Range increases from the bottom to the top, azimuth increases from the left to the right. Top panel: Pauli RGB radar image; bottom panel: LIDAR DTM.

unreliable. On the other hand, the proposed calibration method has been conceived in order to avoid these criticalities. To check this potentiality, it has been tested also with a dual-baseline configuration. This constitutes a very limit case in which the phase calibration problem becomes very challenging. Anyway, the dual-baseline case is also a very interesting solution to reduce the degrading effects of the temporal decorrelation in repeat-pass acquisitions over natural scenarios. In the following sections processing results will be shown to assess the effectiveness of the proposed method and comparisons with the existing techniques will be carried out.

4.2 Processing results: full baseline configuration

This section is devoted to analyze the performance of the whole processing chain achieved when the full baseline stack is employed to calibrate the data. In particular, at first results are presented of experiments carried out over corner reflectors, where the knowledge of their theoretical response is exploited as a way to validate the proposed method. Then, an area of interest is selected and ABF tomograms will be reported to show the calibration performance. Finally, in order to make comparisons between the obtained results and the ones we can get with the existing techniques, some representative pixels are selected and the respective vertical profiles after calibration will be examined.

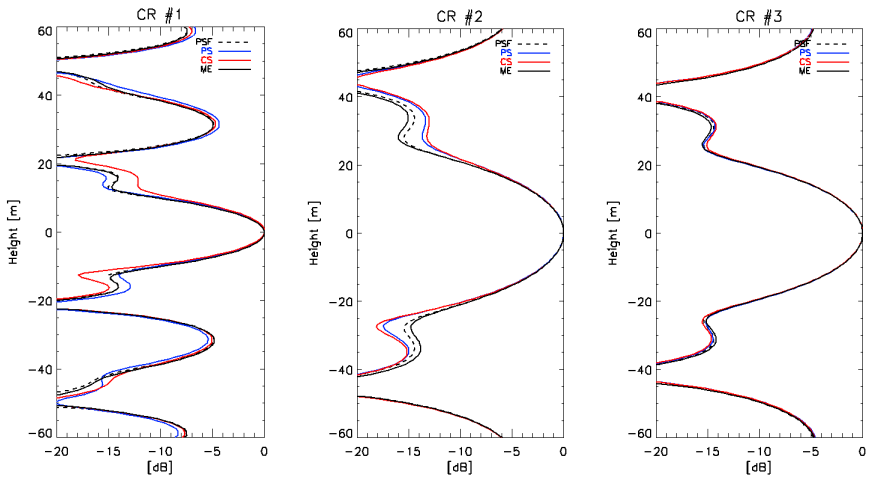

Figure 4.2 – BF profiles in correspondence of corner reflectors. Black dashed line: PSF. Blue line: PS-based method. Red line: CS-based method. Black continuous line: CD-ME.

4.2.1 Experiments with corner reflectors

Prior to any performance analysis, a reliable calibration method has to be tested in correspondence of points in which a reference is available. When the performance analysis has been carried out with simulated data, this reference was the error free profile for each cell of the image stack. Moving to real data, a good reference is the response of the system to a point-like scatterer, i.e. the tomographic PSF. For this reason, in Fig. 4.2 the BF profiles are plotted obtained after calibration in correspondence of three corner reflectors (CRs). In these points, the expected BF profile is the PSF of the system. BF profiles have been reported after the calibration with PSs, CSs, and with CD-ME. The mainlobe width of the PSF enlarges when moving from the first CR to the second and the third ones. In fact, CR2 and CR3 are located in far range, while CR1 is in near range. Thus, the horizontal baseline reduces and the height resolution worsens.

The CD-ME profile fits very well with the PSF for each of the examined points. As regards the other methods, the corresponding profiles are still in good agreement with the PSF. From the plots referred to the first two corner reflectors we can recognize a mismatch in correspondence of the sidelobes of the function between the PSF and the lines referring to the PS and CS, while for the third corner reflector all the lines are superimposed to the PSF.

4.2.2 ABF tomograms

An area of interest has been selected and the proposed calibration algorithm has been applied to two fixed azimuth lines in the HH channel. In particular, two azimuth bins x_1=2750 and x_2=3500 have been chosen and tomograms along the range direction have been considered for a total distance in range of 1425m and 1710m, respectively. In order to make comparisons with the existing techniques, the CS-based calibration has been applied to the corrupted stack. Similar results have been obtained with the PS-based calibration. The resulting tomograms at azimuth x_1 are shown in Fig. 4.3. As already stressed, since the ABF filter is data adaptive, it is very sensitive to miscalibrations, and their effect on the retrieved spectrum is apparent. It is possible to recognize recognize ambiguities and sidelobes in each range coordinate. Moreover,

the effect of the residual phase contributions results in a strong loss of height resolution. Due to these phenomena, it is impossible to distinguish between the bare and the forested areas and to exactly locate the scatterers in height, because of sidelobes which can be as powerful as the main peak. Figs. 4.3(b) and 4.3(c) show respectively the ABF spectra obtained after the CS-based and CD-ME calibrations, respectively. When the full-baseline stack is available, the CS method performs well. In particular, it is possible to distinguish again between the ground and the vegetation layers and to get an accurate estimate of the parameters of interest. The height resolution capability is recovered, since the most of the sidelobes are rejected and the mainlobe width reduces for each range coordinate. A dense vegetation is present in near range, with the top of the canopy located at around 20m with respect to the ground scatterer, which is placed at -5m according to the LIDAR measure. In the middle of the tomogram, a bare area can be seen with a moderate slope, while in far-range a forested area whose extension in height is 25m can be distinguished.

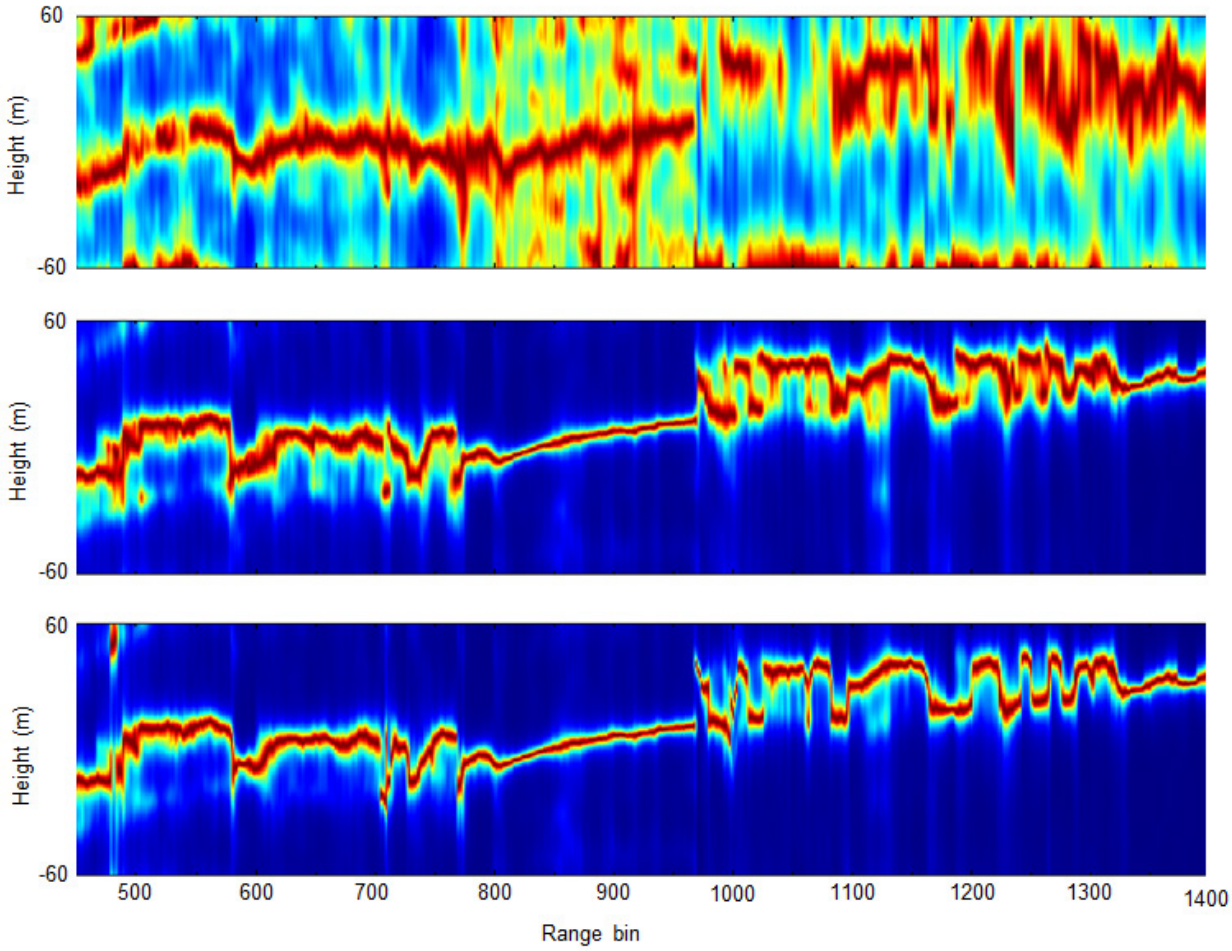

Figure 4.3 – ABF tomograms, full baseline case, azimuth coordinate x_1=2750. Top panel: corrupted data; middle panel: calibrated data with CS method; bottom panel: calibrated data with CD-ME method.

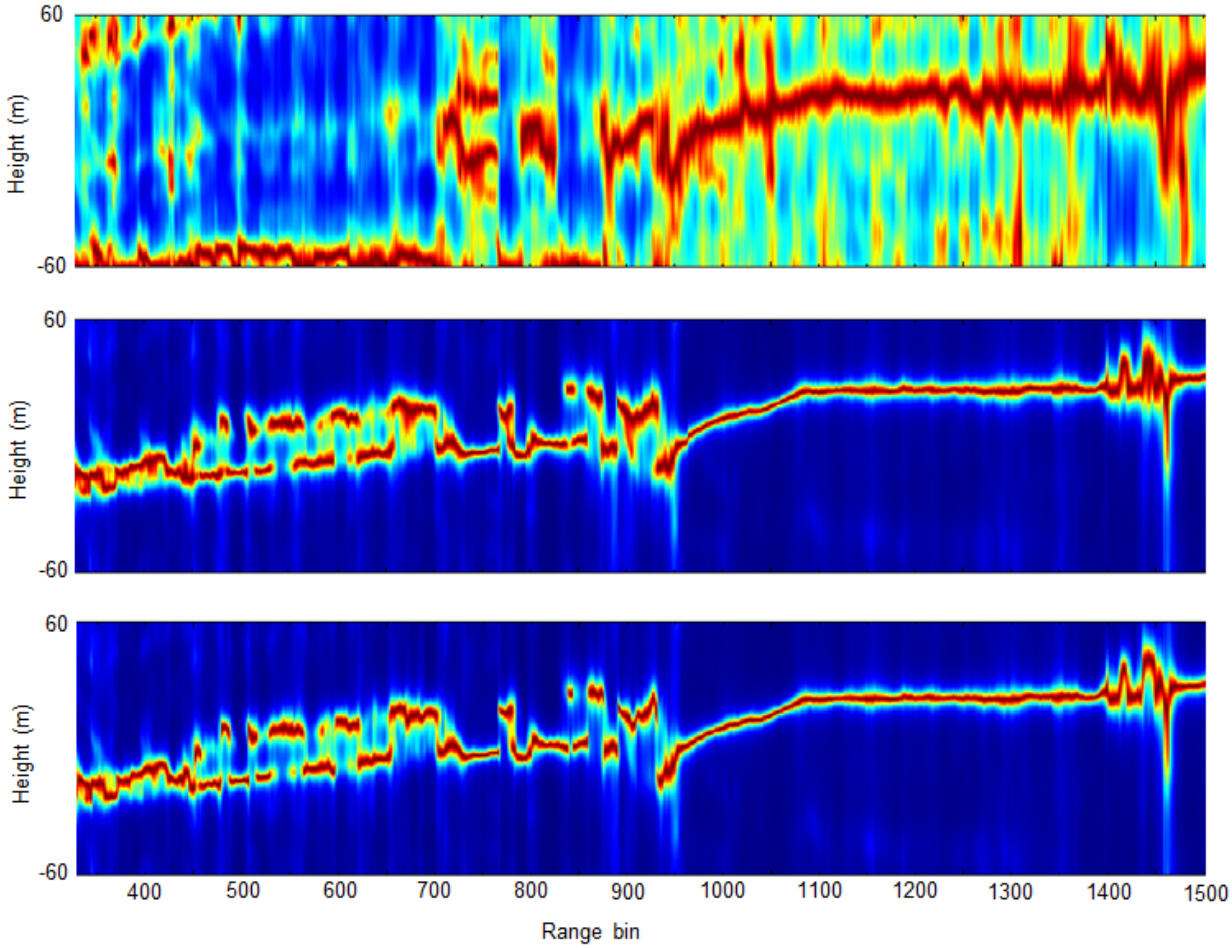

Figure 4.4 – ABF tomograms, full baseline case, azimuth coordinate x_2=3500. Top panel: corrupted data; middle panel: calibrated data with CS method; bottom panel: calibrated data with CD-ME method.

As a further experiment, each polarization has been processed independently, and the estimated calibration phases have been compared. In particular, for each baseline the correlation coefficients have been calculated. The obtained values of the correlation coefficients are higher than 0.85, i.e. a strong correlation exists between the phases estimated from the different polarimetric channels. This means that the estimated phase errors are actually the ones coming from uncompensated platform motions, which are not affected by phase information related to scattering in different polarizations. This constitutes a good indication of the effectiveness of the method in isolating the phase terms of interest from the scattering information.

The same considerations can be repeated for the azimuth coordinate x_2 (see Fig. 4.4). In particular, after calibration the contributions from the ground and the canopy can be separated very clearly. This is achieved thanks to the gain in terms of height resolution after the compensation of the phase errors. These improvements can be actually recognized after the application of both the examined calibration methods, whose performance are not impaired when the full MB stack can be exploited. Anyway, some differences can be noticed between the two calibrated tomograms, which are the result of a better compensation of the miscalibration phases after applying the CD-ME. In order to underline these differences and to compare better the calibration performance, in the following section some representative points will be selected and the corresponding vertical profiles will be shown.

4.2.3 Vertical profiles

In this section the results of a comparison between the proposed method and the one based on the CSs will be shown by analyzing of ABF and BF vertical profiles. In particular, the reported profiles are obtained in correspondence of pixels which are representative of a huge set of resolution cells showing the same features. The range locations of these representative points are shown in Fig. 4.5.

The aim of this analysis is to employ the spectral estimators like probes to highlight the potential presence of residual miscalibrations corrupting the data. In fact, the classical BF is not very sensitive to residual phase contributions, hence it is more stable. Nevertheless, where required, it can be used as a reference to evaluate the capability of the calibration methods in recovering the radiometric fidelity of the ABF profiles. In Fig. 4.6 the ABF profiles are plotted after calibration corresponding to pixels A and B. These cells correspond to bare areas, in which a scattering contribution from the ground is the only one present. In particular, in this and in the following figures the red line plots the profiles obtained CS calibration method, while the black line is referred to CD-ME. As regards the pixel A, the CD-ME profile is able to locate better the ground scatterer with respect to the CS one, since the height corresponding to its maximum peak is closer to the LIDAR measurement (around 14m). The CS profile shows a height shift of 5m. In pixel B, an improvement is apparent in terms of height resolution. In particular, the CD-ME method shows a gain of 1.1m in -3dB mainlobe width, which improves from 6.4m (CS) to 5.3m (CD-ME). As a consequence, the better CD-ME calibration enhances super-resolution properties of ABF, as expected.

The following analysis refers to cells in which two scattering contributions could be recognized, coming from both the ground and the vegetation layer. In Fig. 4.7 the profiles are reported corresponding to the cells C, D, and E respectively. In the first cell (pixel C) a volume layer is present, which is located at 5m height, over a ground scatterer placed at -25m, while in the second one (pixel D) the ground contribution is located in height at -20m. From both the CS and CD-ME profiles it is possible to distinguish two main peaks representing the two scattering mechanisms, meaning that the phase calibration has been performed successfully. Anyway, some differences can be noticed clearly between the profiles. After the calibration with the CD-ME approach the two peaks are better resolved in both pixels C and D, while the CS-based profiles are less sharp. This behavior can be due to residual miscalibrations still affecting the MB stack after processing. The same considerations can be repeated for the profiles corresponding to the pixel E, where the height centroid of the volume scatterer is located at around 40m, while the ground contribution is present at 15m (according to LIDAR measure). In particular, by analyzing the CS profile it is worth to point out the presence of a strong sidelobe located at -20m which is almost as powerful as the ground contribution. In this case some ambiguities could arise in the ground height estimation, as it is difficult to distinguish the surface scatterer from the sidelobe. This sidelobe could be due to a residual phase error, such that the ABF filter emphasizes the corresponding spatial frequency with height -20m, rejecting the one corresponding to the ground contribution. This sidelobe is well suppressed in the profile obtained after the calibration with the ME. In this case, a gain of 5dB in terms of sidelobe rejection can be measured with respect to the CS profile, which means that the residual phase contribution has been compensated as well.

As regards the radiometric fidelity, the analysis of the pixels F and G is noteworthy. Unfortunately, in absence of a ground truth, it is not possible to state exactly which is the inaccurate profile (i.e. the one still affected by miscalibrations), unless a further analysis is carried out. However, a possible reference can be the BF profile, as it is less prone to miscalibration residuals. In Fig. 4.8 both the BF and ABF profiles are reported after calibration with the ME and the CS method. Figure refers to the cell F, where a main volume contribution is present at 15m height and a less powerful echo from the ground scatterer is located at 5m. The BF profiles are almost superimposed (at least in a height interval close to the mainlobe) and the power relation between the two maxima is almost the same for both the ME and CS profiles. Since the BF is radiometrically linear, this power relation can be assumed as reference. Considering the ABF filtering, the CD-ME profile exhibits a power relation between the peaks in the order of the one in the corresponding BF profile, with a stronger contribution from the volume and a weaker one from the surface. The profile appears sharp. On the other hand, the shape of the CS profile is very different, and the two peaks are almost identically powerful. In this case the radiometric fidelity is not preserved, and the explanation of the change in the profile behavior has to be found in a residual contribution of phase errors which are well compensated after the ME-based calibration. In order to better investigate this features and to have a clear validation of the last conclusions, a further simulated analysis has been performed. In particular, an error free profile with two scatterers has been simulated in such a way that the BF spectrum of the simulated profile matches with the one retrieved from real data [see Fig. 4.9(a)]. Then, the ABF profile has been calculated and compared with the one obtained after CD-ME calibration. A good agreement between the two profiles has been found [see Fig. 4.9(b)]. Since the simulated one has been obtained in absence of errors, this means that the proposed method has been able to estimate the calibration phases better than the CS-based.

Several cells with these features have been found in the examined azimuth lines. As a last example, Fig. 4.10 reports a case in which is very apparent the effect of residual miscalibrations in the CS-based ABF profile. In fact, in this cell a stronger contribution from the volume is present at 15m height, while a weaker contribution from the ground comes from 5m. This is apparent from the BF plots, where both the CS and the CD-ME match. Again, with the ABF filter the behavior of the red line totally changes and the power relation between the peaks is inverted, with a more powerful peak from the surface, while the CD-ME profile shows the same power relation of the BF. This constitutes a clear indication of the better capabilities of the proposed method in recovering the radiometric fidelity of the profiles, a very important feature for the analysis of forest scenarios.

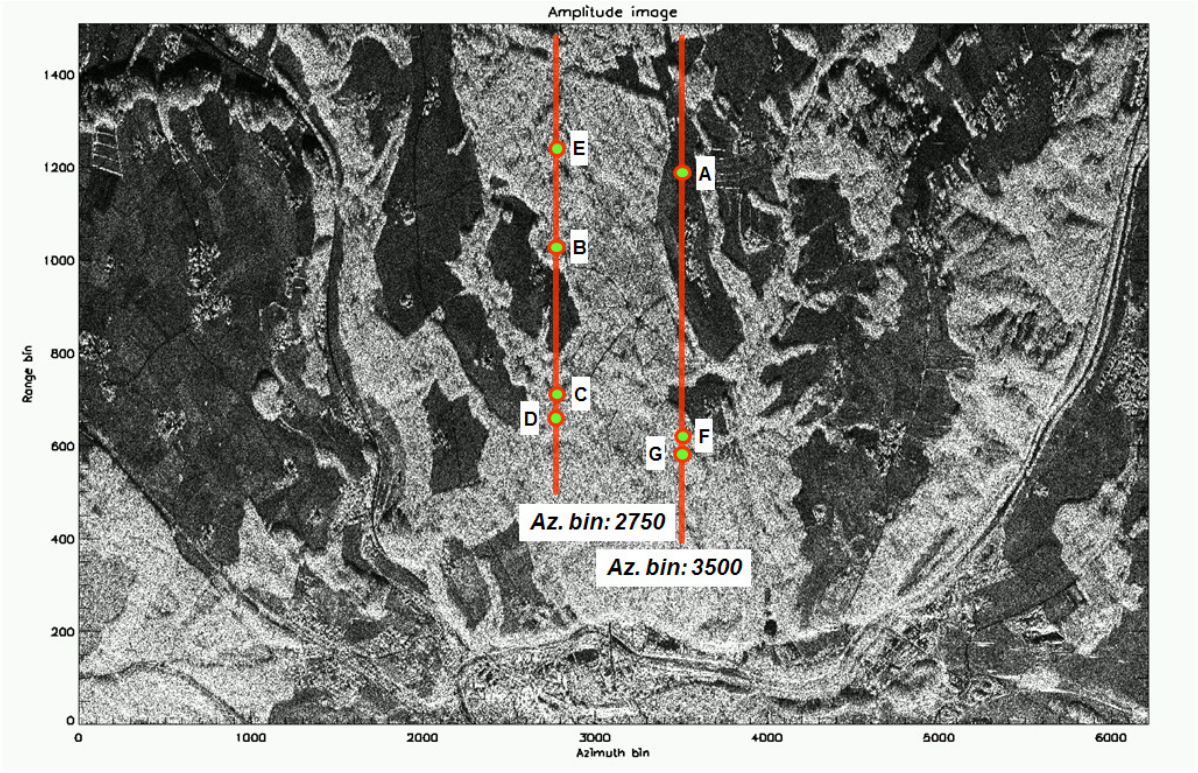

Figure 4.5 – HH range-azimuth image. Red lines: analyzed lines at constant azimuth. Green dots: locations of the analyzed cells.

MARKER	AZ. BIN	RG. BIN	TYPE
A	3500	1000	Bare
B	2750	850	Bare
C	2750	620	Forested
D	2750	648	Forested
E	2750	1125	Forested
F	3500	577	Forested
G	3500	578	Forested

Table 4.1 – Range-azimuth position and characteristics of the analyzed cells.

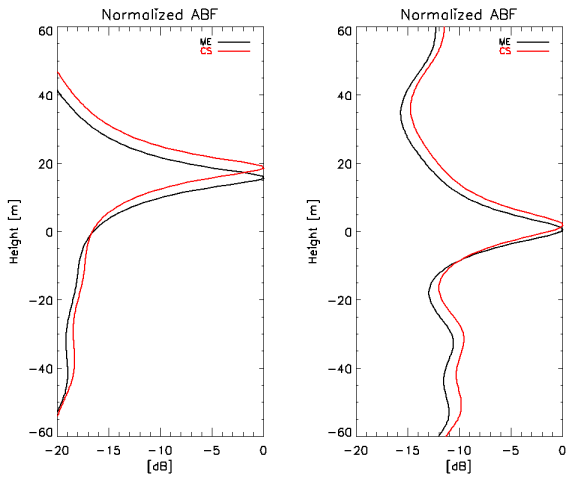

Figure 4.6 – ABF vertical profiles after calibration. Red line: CS method. Black line: CD-ME method. Figure refers to bare areas. Left panel: pixel A; right panel: pixel B.

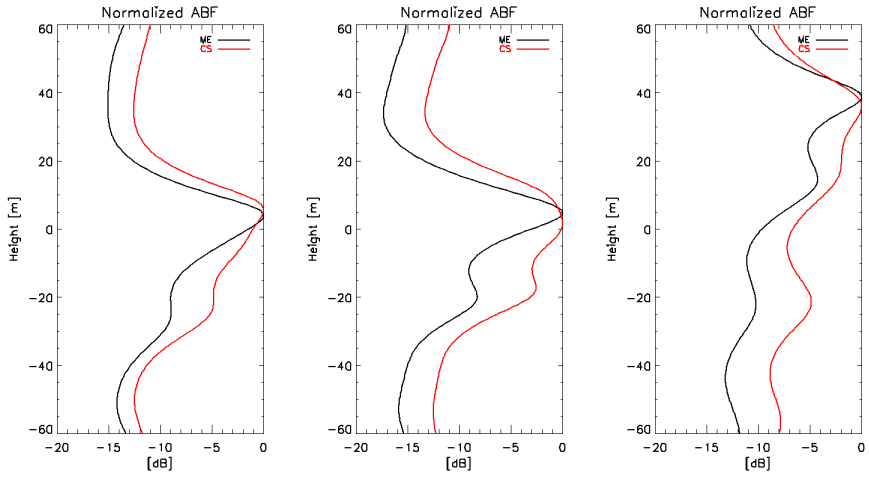

Figure 4.7 – ABF vertical profiles after calibration. Red line: CS method. Black line: CD-ME method. Figure refers to forested areas. Left panel: pixel C; middle panel: pixel D; right panel: pixel E.

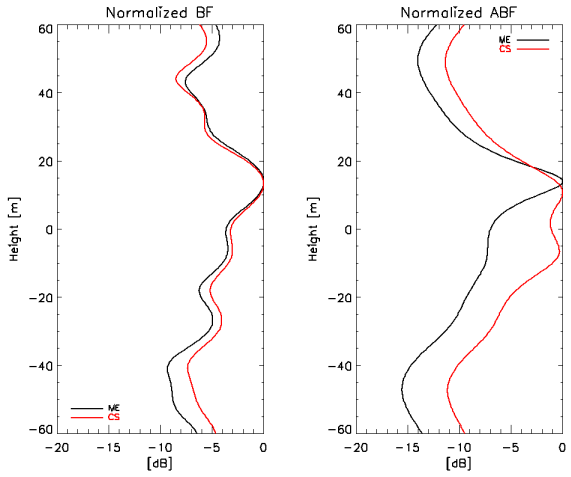

Figure 4.8 – Vertical profiles of the pixel F after calibration. Red line: CS method. Black line: CD-ME method. Figure refers to forested areas. Left panel: BF profiles; right panel: ABF profiles.

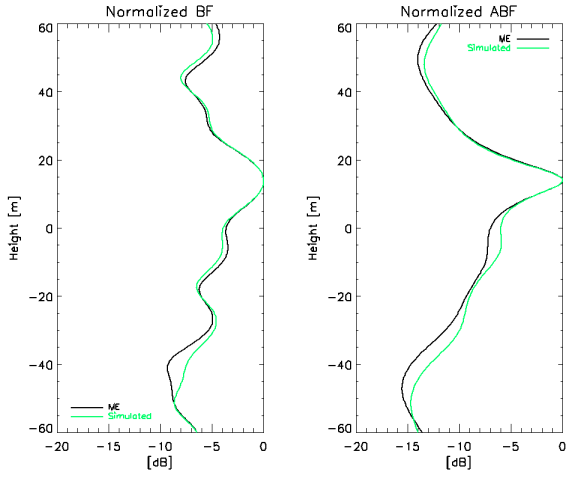

Figure 4.9 – Vertical profiles of the pixel F after calibration. Green line: simulated. Black line: CD-ME method. Figure refers to forested areas. Left panel: BF profiles; right panel: ABF profiles.

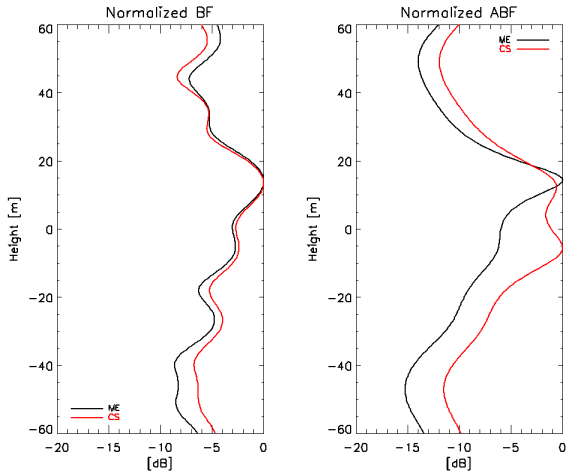

Figure 4.10 – Vertical profiles of the pixel G after calibration. Red line: CS method. Black line: CD-ME method. Figure refers to forested areas. Left panel: BF profiles; right panel: ABF profiles.

4.3 Results with a dual-baseline configuration

The last part of the performance analysis presents the calibration results obtainable when a few acquisition are available for processing. In particular, the dual-baseline configuration is a limit case because of the low number of acquisitions which can impair the detection of reliable scatterers in the PS/CS methods. On the other hand it is worth to remind that this kind of baseline configuration is particularly appealing in repeat-pass SAR sensing of natural areas where the scattering is subjected to temporal decorrelation effects. As for the full baseline case, two azimuth coordinates of interest have been selected and the proposed calibration chain has been applied together with the other calibration methods (PS-based and CS-based) in order to make some comparisons.

In particular, the azimuth bins x_3=3000 and x_4=5200 have been chosen (see Fig. 4.11, where the amplitude SAR image of the test site is reported) and again tomograms have been extracted for a total range distance of 1595m and 1760m respectively. As regards the coordinate x_3, Fig. 4.12 shows respectively the ABF tomograms obtained from the corrupted data, from the data calibrated with the CS-based method and the one obtained after applying the proposed scheme. The corrupted tomogram shows pseudo-ambiguities and sidelobes; moreover, some height shifts can be recognized and it becomes very difficult to place properly the main scattering mechanisms. In this case, the CS method is not able to estimate the calibration phases, as the quality of the retrieved spectrum is very low and variable in space, depending on the performance of the CS detection. While this method fails with a few acquisitions, the proposed CD-ME still works well, as shown in Fig. 4.12(c). From the ABF tomograms the ground, the vegetation layer and the scattering from the top of the canopy can be distinguished. The ambiguities disappears and also the sidelobe rejection improves. Some residual lobes in near-range are still present, which are actually due to the PSF in height. The ABF after CD-ME is also able to recover the loss of height resolution, demonstrating not to be strongly affected by the low number of available baselines. The same considerations can be repeated for the analysis of the azimuth coordinate x_4 (see Fig. 4.13) where the proposed method with the PS-based technique, whose corresponding tomographic spectrum is shown in Fig. 4.13(b). This azimuth line is

characterized by a big slope corresponding to a hill with a low vegetation cover. As expected, the PS techniques totally fails in this challenging case. On the contrary, a good quality of the ABF tomograms after CD-ME from which we can still recognize the vertical structure of the investigated area. Again, some residual lobes are still present which are due to the system PSF. However, the gain in terms of ambiguity suppression, super-resolution and height shift compensation is apparent.

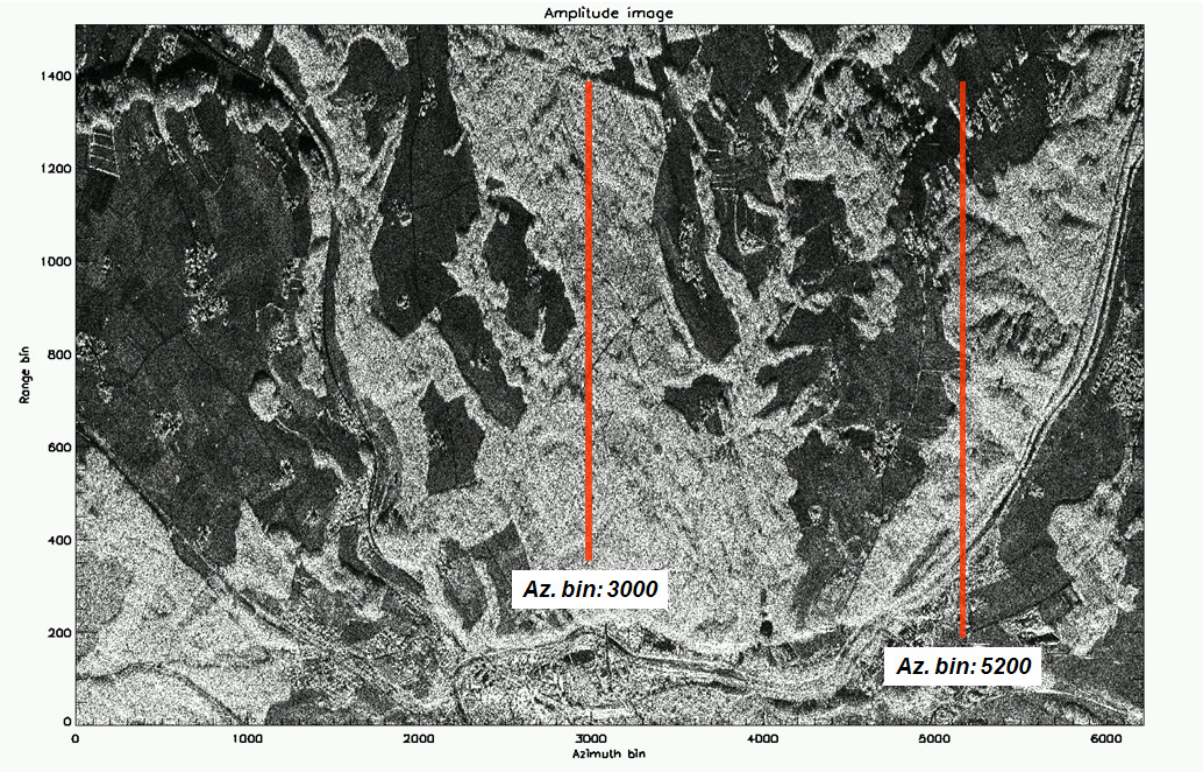

Figure 4.11 – HH range-azimuth image. Red lines: lines at constant azimuth used for the dual baseline analysis.

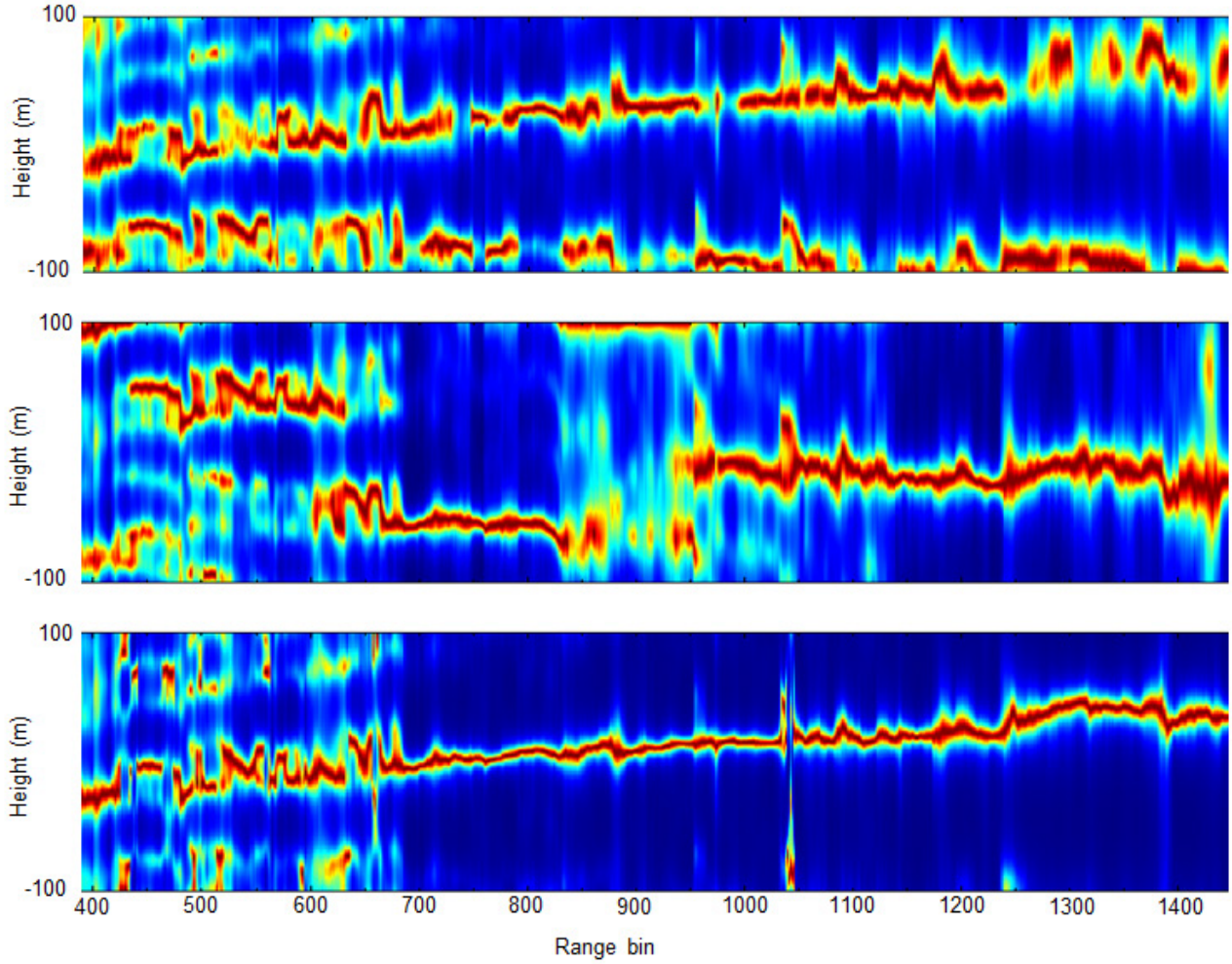

Figure 4.12 – ABF tomograms, dual baseline case, azimuth coordinate x_3=2750. Top panel: corrupted data; middle panel: calibrated data with CS method; bottom panel: calibrated data with CD-ME method.

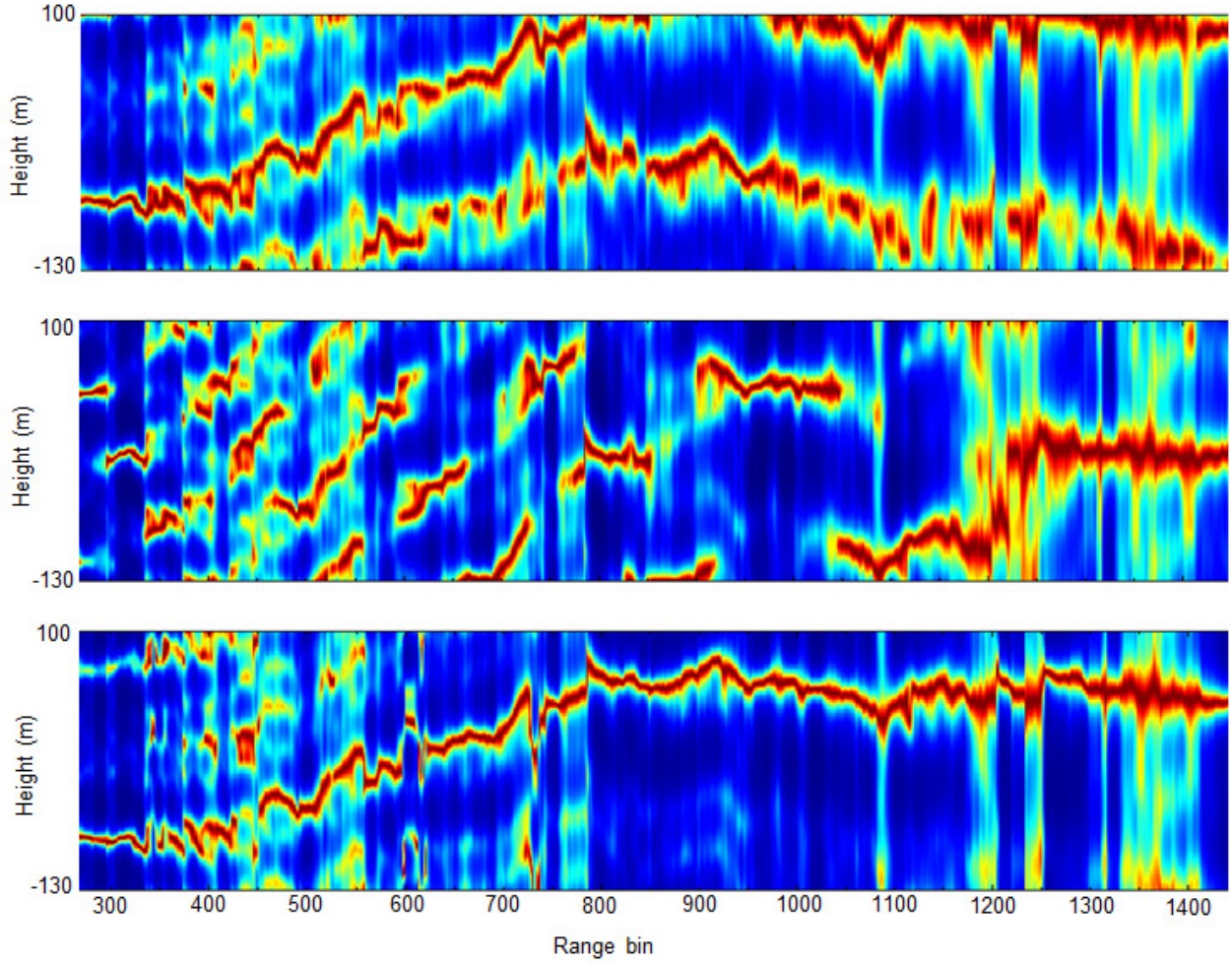

Figure 4.13 – ABF tomograms, dual baseline case, azimuth coordinate x_4=5200.Top panel: corrupted data; middle panel: calibrated data with PS method; bottom panel: calibrated data with CD-ME method.

- This page intentionally left blank -

CHAPTER 5

CONCLUSIONS AND OUTLOOK

The processing of MB-SAR data exploits the coherent combination of complex SAR data to retrieve the information of interest about the observed scene. In this framework, this work is focused on SAR tomography which allows resolving along the height dimension different scatterers belonging to the same range-azimuth cell. In this way it is possible to extract information about the vertical structure of the observed area. Unfortunately, especially in airborne SAR acquisitions, residual non-compensated platform motions result in baseline estimation errors. On the other hand, atmospheric propagation delays have to be accounted for in space borne acquisitions. In both cases, the MB data stack is affected by unknown phase contributions different from track to track. As a consequence, prior to any MB coherent processing, it is necessary to correct the data stack for these phase miscalibrations. From a signal processing perspective, the phase calibration can be carried out by following two different classes of algorithms. A first class makes use of a grid of targets of opportunity (generally point-like) which remain stable during the entire acquisition time span. Depending on the stability criterion, these scatterers are defined “persistent” (PS) or “coherent” (CS). MB calibration methods based on the detection of PS and CS have been developed and tested so far. However, the effectiveness of this class of techniques is scenario-dependent. In fact, in natural scenarios the presence of stable point-like scatterers is more reduced than in urban scenarios. Moreover, as the number of baselines is typically kept low to avoid temporal decorrelation problems, the detection performance worsen and the calibration quality degrades dramatically. As a consequence, the MB phase calibration in presence of a few tracks turns out to be a challenging task. To overcome all these problems, a second class of algorithms has been introduced based on some kind of MB autofocus. However, the common feature of the existing methods is that their performance is very scenario dependent.

This work proposes and investigates a new calibration method based on the minimization of the entropy of the adaptive beamforming (ABF) tomogram in the SAR cell under test. Indeed, in the context of the information theory the minimization of the entropy of the ABF tomogram is equivalent to the maximization of its sharpness, as it get reduced when phase miscalibrations corrupt the data, especially with

ABF. It is worth noting that the proposed method exploits the whole MB information, and there is no need to focus on a particular target or on a scatterer in the profile. In this way the spatial coverage of calibration targets is full and a single polarimetric channel is sufficient to correct properly the whole MB data stack.

The proposed calibration chain operates on a MB single-pol data stack in 5 steps. For each baseline, the interferometric phase is estimated and compensated from the complex MB data. So doing, the remaining MB complex data stack is a function of the complex backscattering at each baseline (i.e. the vertical profile) translated around the zero height, with additional phase contributions due to the DEM variations from baseline to baseline. These phase residuals can be estimated by minimizing the entropy of the ABF tomogram for each SAR cell. Then, if the original miscalibration phases (i.e. those affecting the original MB dataset) are of interest, they can be estimated from the interferometric phases calculated at the beginning by applying local averages. Actually, this last block relies on the reasonable assumption of low variability in the range-azimuth space of the phase errors.

It is worth noting that the entropy minimization is a non-convex optimization problem which does not admit a closed form solution. To this purpose, two different iterative methods have been investigated which are different ways to try to overcome the trade-off existing between reliability and complexity. Of course, the exhaustive method is the most reliable one because the convergence to the global minimum of the entropy functional is guaranteed. Unfortunately, it is unfeasible when the number of images increases (i.e. when $K > 3$). The first proposed iterative method proceed through exhaustive optimizations sequentially. In this way, the method is faster than the exhaustive one and it is still feasible when the number of images to process exceeds 3. A faster iterative solution has been implemented, called coordinate descent. The solution is found iteratively by optimizing the phases one by one while keeping the others fixed. In this way the minimization problem turns out to be scalar at each iteration, and the computational complexity reduces. For both algorithms, the convergence to the global minimum is not granted. These two kind of optimizations have been implemented and tested with a simulated stack. In particular, PolSARProSim data have been corrupted with a random phase noise and the algorithms have been applied in order estimate the error-free vertical profiles. As a performance measure, the normalized error energy has been computed between the reference ABF profile and the one after optimization. From the comparisons carried out in Chapter 3, the coordinate descent algorithm results also to be the best one in recovering the right vertical profile, with errors approaching the null value in each simulation. This result is obtained by choosing as a starting point the one with a set of identical phases, whose value is determined according to a one-dimensional exhaustive optimization. For these reasons, the coordinate descent solution has been chosen to constitute the core processing of the proposed scheme.

The whole calibration chain has then been implemented and tested with both simulated and real data. In the first case the reference stack has been corrupted with residual motion phases estimated from the DLR E-SAR TempoSAR 2008 dataset. A performance analysis has been carried out measuring the reconstruction errors of the profiles. The chain has been tested with both the full baseline stack, other thinned baseline configurations and with a poor dual baseline configuration. Results show the effectiveness of the proposed method in estimating the calibration phases and, hence, in reconstructing properly the vertical profiles. In

particular, in the dual baseline case the error approaches the null value for the most of the analyzed azimuth coordinates. The method has also been shown to be able to recover the exact amplitudes of the backscattered powers in the SAR cells under test, thus preserving the radiometric fidelity of the tomographic imaging.

As regards the test with real data, a dataset acquired by means of the DLR's E-SAR platform over the forest site of Traunstein has been processed. The experiments carried out over corner reflectors, whose tomographic response is known, have shown a better match of the obtained minimum entropy profiles with the system PSF. Then, an area of interest has been selected and tomograms have been analyzed to show the calibration performance. Finally, some representative cells have been selected and the respective vertical profiles after calibration have been examined. Other tomographic experiments have demonstrated the superiority of the proposed method with respect to the existing techniques. In particular, from the vertical profiles gains in terms of height resolution and sidelobe suppression have been shown in the ABF profiles. In the bare areas the ground scatterers are better located with respect to the reference LIDAR measures), and the mainlobe width reduces (1m gain). In the cells where two scattering contributions are present, coming from the surface and the volume layer, they are better resolved and the peak to sidelobe level increases (up to 5dB gain in the examined pixels). This means that the phase errors have been properly compensated, as the remarkable properties of the ABF imaging are restored.

Future work on this topic could be aimed at both further theoretical developments and experiments. The following lines have been individuated:

1. In the airborne case, a model is available for the phase errors due to non-compensated platform motions, see equation (1.27). As a consequence, for each azimuth coordinate, the problem reduces to the estimation of the vertical and horizontal platform displacements from the nominal track, repeated for all the tracks. One could consider to minimize the entropy of the 2-D tomogram in the range-height plane. In this way, the calibration of the entire dataset would be faster than calibrating each single cell, at the cost of an increased dimensionality of the optimization problem (2 parameters per track instead of one);
2. A slight dependence of the calibration performance on the specific profile has been observed in Chapter 3. Further simulated experiments should be devoted to verify this tendence;
3. Further experiments could be carried out to verify an improvement in the estimation of the polarimetric scattering mechanisms estimated by means of polarimetric Tomo-SAR as a consequence of an improved phase calibration;
4. Further experiments should be devoted to assess the retrieved radiometric fidelity;
5. Other airborne/spaceborne real data sets should be employed to assess the calibration performance with different scenarios (e.g. other forests, urban, ice covered…);
6. The performance obtainable in the calibration of temporally varying scenarios (e.g. due to deformations and/or temporal decorrelation) should be investigated. In this case, the entropy of the differential tomographic profile could be a useful functional to be considered.

- This page intentionally left blank -

REFERENCES

[1] J. B. Campbell, *Introduction to Remote Sensing*, Taylor & Francis, London, 2002.

[2] R. Bamler, P. Hartl, "Synthetic Aperture Radar Interferometry", Inverse Problems, vol.14, pp. R1-R54, August 1998.

[3] L. C. Graham, "Synthetic Interferometer Radar for Tomographic Mapping", *Proceedings of the IEEE*, vol. 62, pp. 763-764, June 1974.

[4] P. Rosen, S. Hensley, I. R. Joughin, F. K. Li, S. N. Madsen, E. Rodirguez, and R. M. Goldstein, "Synthetic Aperture Radar Interferometry", *Proceedings of the IEEE*, vol. 88, pp. 331-382, March 2000.

[5] F. Gini, F. Lombardini, "Multibaseline Cross-Track SAR Interferometry: A Signal Processing Perspective"*, IEEE Aerospace and Electronic Systems Magazine,* vol. 20, no. 8, pp. 71-93, August 2005.

[6] A. Ferretti, C. Prati, and F. Rocca, "Nonlinear Subsidence Rate Estimation Using the Permanent Scatterers in Differential SAR Interferometry", *IEEE Transactions on Geoscience and Remote Sensing*, vol. 38, no. 5, pp. 2202-2212, May 2000.

[7] P. Berardino, G. Fornaro, R. Lanari, and E. Sansosti, "A New Algorithm for Surface Deformation Monitoring Based on Small Baseline Differential SAR Interferograms", *IEEE Transactions on Geoscience and Remote Sensing*, vol. 40, no.11, pp. 2375-2383, November 2002.

[8] S. R. Cloude, K. P. Papathanassiou, "Polarimetric SAR Interferometry", *IEEE Transactions On Geoscience And Remote Sensing*, vol. 36, no. 5, pp. 1551-1563, September 1998.

[9] K. P. Papathanassiou, S. R. Cloude, "Single-Baseline Polarimetric SAR Interferometry", *IEEE Transactions On Geoscience And Remote Sensing,* vol. 39, no. 11, pp. 2352-2363, November 2001.

[10] S. R. Cloude, K. P. Papathanassiou, "Three-stage inversion process for polarimetric SAR interferometry", *IEEE Proc.-Radar Sonar Navig*., vol. 150, no. 3, pp. 125-134, June 2003.

[11] C. López-Martínez, A. Alonso, X. Fàbregas, K. P. Papathanassiou, "Ground topography estimation over forests considering Polarimetric SAR Interferometry", pp. 3612-3615, *IGARSS*, Honolulu, Hawaii, USA, July 2010.

[12] A. Reigber, A. Moreira, “First Demonstration of Airborne SAR Tomography Using Multibaseline L-Band Data”, *IEEE Transactions On Geoscience And Remote Sensing*, vol. 38, no. 5, pp. 2142-2152, September 2000.

[13] M. Pardini, *Advances and Experiments of Tomographic SAR Imaging for the Analysis of Complex Scenarios*, Ph.D. Thesis, University of Pisa, Italy, June 2010.

[14] S. Sauer, L. Ferro-Famil, A. Reigber, E. Pottier, “Three-Dimensional Imaging and Scattering Mechanism Estimation Over Urban Scenes Using Dual-Baseline Polarimetric InSAR Observations at L-band”, *IEEE Transactions On Geoscience And Remote Sensing*, vol. 49, no. 11, pp. 4616-4629, November 2011.

[15] F. Lombardini, “Differential Tomography: A New Framework For SAR Interferometry”, *IEEE Transactions on Geoscience and Remote Sensing*, vol. 43, no. 1, pp. 37-44, January 2005.

[16] F. Lombardini, M. Pardini, F. Cai, “Polarimetric Differential-TomoSAR Imaging”, *Proc. Of European SAR Conference*, EUSAR, Aachen (Germany), June 2010.

[17] S.K. Lee, F. Kugler, K. Papathanassiou, I Hajnsek, “Multibaseline Polarimetric SAR Interferometry Forest Height inversion Approaches”, *Proc. of ESA POLINSAR Workshop*, Frascati (Italy), January 2011.

[18] S. Tebaldini, A. Monti Guarnieri, *Methods and Performance for Multipass SAR Interferometry*, in *Geoscience and Remote Sensing. New Achievements*, Intech Online Publisher.

[19] P. Pasquali, C. Prati, F. Rocca, M. Seymour, J. Fortuny, E. Olmer, and A. J. Sieber, “A 3D SAR Experiment with EMSL Data”, *Proc. of 1995 IEEE International Geoscience and Remote Sensing Symposium (IGARSS)*, Florence (Italy), July 19955.

[20] J. Homer, I. D. Longstaff, Z. She, and D. Gray, “High Resolution 3-D Imaging Via Multi-Pass SAR”, *IEEE Proceedings, Part F-Radar, Sonar and Navigation*, vol. 149, pp. 45-50, February 2002.

[21] F. Gini, F. Lombardini, and M. Montanari, “Layover Solution in Multibaseline SAR Interferometry”, *IEEE Transactions on Aerospace and Electronic Systems*, vol. 38, pp. 1344-1356, October 2002.

[22] G. Fornaro, F. Serafino, and F. Soldovieri, “Three Dimensional Focusing With Multi-pass SAR”, *IEEE Transactions on Geoscience and Remote Sensing*, vol. 41, pp. 507-517, March 2003.

[23] F. Lombardini and A. Reigber, “Adaptive Spectral Estimation for Multibaseline SAR Tomography with L-Band Data”, *Proc. of 2003 IEEE International Geoscience and Remote Sensing Symposium (IGARSS)*, Tolouse (France), July 2003.

[24] G. Fornaro, F. Lombardini and F. Serafino, “Three-Dimensional Multipass SAR Focusing: Experiments with Long Term Data”, *IEEE Transactions on Geoscience and Remote Sensing*, vol. 43, no. 5, pp. 702-714, May 2005.

[25] I. Hajnsek, R. Scheiber, L. Ulander, A. Gustavsson, G. Sandberg, S. Tebaldini, A. M. Guarnieri, F. Rocca, F. Lombardini, and M. Pardini, *Technical Assistance for the Development of Airborne SAR and Geophysical Measurements During the BioSAR 2007 Experiment*, tech. rep., ESA contract no. 20755/07/NL/CB.

[26] F. Lombardini and M. Pardini, "3-D SAR Tomography: The Multibaseline Sector Interpolation Approach", *IEEE Geoscience and Remote Sensing Letters,* vol. 5, pp. 630-634, October 2008.

[27] F. Lombardini, M. Pardini, and L. Verrazzani, "A Robust Multibaseline Sector Interpolator for 3D SAR Imaging", *in Proc. of 2008 European Synthetic Aperture Radar Conference (EUSAR)*, Friedrichshafen (Germany), June 2008.

[28] S. Tebaldini, "Forest SAR Tomography: A Covariance Matching Approach", in *Proc. of 2008 IEEE RADAR Conference (RADARCon)*.

[29] S. Tebaldini, "Algebraic Synthesis of Forest Scenarios from Multibaseline PolInSAR Data", *IEEE Transactions on Geoscience and Remote Sensing*, vol. 47, pp. 4132-4142, December 2009.

[30] X. X. Zhu, R. Bamler, "Very High Resolution Spaceborne SAR Tomography in Urban Environment", *IEEE Transactions on Geoscience and Remote Sensing*, vol. 48, no. 12, pp. 4296-4308, December 2009.

[31] E. Aguilera, M. Nannini, and A. Reigber, "Multi-Signal Compressed Sensing for Polarimetric SAR Tomography", *Proc. of IEEE International Geoscience and Remote Sensing Symposium (IGARSS)*, Vancouver, Canada, July 2011.

[32] P. Stoica, R. L. Moses, *Introduction to Spectral Analysis*, Prentice-Hall, 1997.

[33] S. Tebaldini, A. Monti Guarnieri, "On the Role of Phase Stability in SAR Multibaseline Applications", *IEEE Transactions On Geoscience And Remote Sensing*, vol. 48, no. 7, pp. 2953-2966, July 2010.

[34] K. Iribe, K. Papathanassiou, I. Hajnsek, M. Sato, Y. Yokota, "Coherent Scatterer in forest environment: detection, properties and its applications", *Proc. of IEEE International Geoscience and Remote Sensing Symposium (IGARSS)*, Honolulu, Hawaii (USA), July 2010.

[35] A. Jacoksson, F. Gini, F. Lombardini, "Robust estimation of Radar Reflectivities in Multibaseline InSAR", *IEEE Transactions on Aerospace and Electronic Systems*, vol. 41, no. 2, pp. 751-758, April 2005.

[36] H. L. Van Trees, *Optimum Array Processing. Part IV of Detection, Estimation, and Modulation Theory*. Wiley, 2002.

[37] Y. Rockah, P. M. Schultheiss, "Array Shape Calibration Using Sources in Unknown Locations – Part I: Far-Field Sources", *IEEE Transactions On Acoustics, Speech, And Signal Processing*, vol. ASSP-35, no.3, pp. 286-299, March 1987.

[38] S. M. Kay, *Fundamentals of Statistical Signal Processing – Estimation Theory*, Prentice-Hall, 1993.

[39] M. Pardini, F. Lombardini, F. Gini, " The Hybrid Cramér-Rao Bound on Broadside DOA Estimation of Extended Sources in Presence of Array Errors", *IEEE Transactions on Signal Processing*, vol. 56, no. 4, pp. 1726-1730, April 2008.

[40] M. Viberg, A. L. Swindlehurst, "A Bayesian Approach to Auto-Calibration for Parametric Array Signal Processing", *IEEE Transactions On Signal Processing*, vol. 42, no.12, pp. 3495-3507, December 1994.

[41] M. P. Wylie, S. Roy, H. Messer, "Joint DOA Estimation and Phase Calibration of Linear Equispaced (LES) Arrays", *IEEE Transactions On Signal Processing*, vol. 42, no.12, pp. 3449-3459, December 1994.

[42] B. P. Flanagan, K. L. Bell, "Array Self-Calibration With Large Sensor Position Errors", *Signal Processing*, vol. 81, pp. 2201-2214, 2001.

[43] A. Ferretti, C. Prati, F. Rocca, "Permanent Scatterers in SAR Interferometry", *IEEE Transactions on Geoscience and Remote Sensing*, vol. 39, no. 1, pp. 8-20, January 2001.

[44] K. Iribe, *Investigations on Coherent Scatterers in Natural Environments for SAR Multi-Image Applications*, Ph.D. Thesis, Graduate School of Environmental Studies, Tohoku University, August 2010.

[45] G. Ferraioli, G. Ferraiuolo, V. Pascazio, "Phase-Offset Estimation in Multichannel SAR Interferometry", *IEEE Geoscience And Remote Sensing Letters*, vol. 5, no. 3, pp. 458-562, July 2008.

[46] G. Gatti, S. Tebaldini, M. Mariotti d' Alessandro, F. Rocca, "ALGAE: A Fast Algebraic Estimation of Interferogram Phase Offsets in Space-Varying Geometries", *IEEE Transactions On Geoscience And Remote Sensing*, vol. 49, no. 6, pp. 2343-2353, June 2011.

[47] S. Tebaldini, F. Rocca, "Multibaseline Polarimetric SAR Tomography of a Boreal Forest at P- and L-Bands", *IEEE Transactions on Geoscience And Remote Sensing*, vol. 50, no. 1, pp. 232-246, January 2012.

[48] Y. Huang, L. Ferro-Famil, F. Lombardini,"Improved Tomographic SAR Focusing Using Automatic Baseline Error Compensation", in *Proc. Of ESA PolInSAR Workshop*, Frascati, Italy, January 2011.

[49] R. L. Morrison, M. N. Do, D. C. Munson, "SAR Image Autofocus By Sharpness Optimization: A Theoretical Study", *IEEE Transactions on Image Processing*, vol. 16, no. 9, pp. 2309-2321, September 2007.

[50] T. J. Kragh, "Monotonic Iterative Algorithm for Minimum-Entropy Autofocus", *Proc. of 14th Annual ASAP Workshop*, June 2006.

[51] M. L. Williams, *PolSARproSim – A Coherent, Polarimetric SAR Simulation of Forests for PolSARPro – Design Document and Algorithm Specification*, December 2006, available at http://envisat.esa.int/polsarpro/Manuals/PolSARproSim_Design.pdf

[52] M. Pardini, F. Lombardini, F. Gini, "The Hybrid Cramer-Rao Bound on Broadside DOA Estimation of Extended Sources in Presence of Array Errors", *IEEE Transactions on Signal Processing*, vol. 56, no. 4, pp. 1726-1730, April 2008.

[53] M. Pardini, *Array Interpolation Methods for Non-Uniform Multibaseline SAR Interferometers*, M.Eng. Thesis, University of Pisa, Italy, June 2006